

MOLECULAR DYNAMICS (MD) SIMULATION STUDY OF LOW ANGLE GRAIN  
BOUNDARY (LAGB) MOBILITY IN PURE Al AND Al-Mg ALLOYS

MOLECULAR DYNAMICS (MD) SIMULATION STUDY OF LOW ANGLE GRAIN  
BOUNDARY (LAGB) MOBILITY IN PURE Al AND Al-Mg ALLOYS

By

MD. JAHIDUR RAHMAN, M.A.Sc, B.Sc. (Engineering)

A Thesis  
Submitted to the School of Graduate Studies  
In Partial Fulfilment of the Requirements  
for the Degree  
Doctor of Philosophy

McMaster University  
© Copyright by Md. Jahidur Rahman, April 2014



## Abstract

Low angle grain boundary (LAGB) mobility is an essential parameter for developing the analytical models that describe the kinetics of recovery and predict the nucleation of recrystallized grains. The thesis is aimed at the molecular dynamics (MD) simulations study of LAGB mobility determination in pure Al and Al-Mg alloys. All the previous experimental studies reported that the presence of several defects, such as solutes and dislocations, retard the boundary motion and provide lower mobility. However, very few studies have been conducted in MD simulation to capture the interactions of those defects with the migrating grain boundary. This thesis is focused on providing complete understanding of LAGB determination along with a comprehensive explanation of solute and dislocation retarding effects on boundary motion.

The LAGB mobility in pure Al was computed from two different MD techniques as a function of temperature and misorientation. Within numerical uncertainties, both techniques provide the same magnitude of mobility at 300K for  $7.785^\circ$  boundary and at 700K for  $23.07^\circ$  boundary. It was observed that ADF method is not applicable to determine LAGB mobility at high temperature due to failure of order parameter computation. The MD derived activation energy is found to be approximately ten times lower than the experimental observations.

A strong solute pinning effect on boundary motion was observed at all misorientations and solute concentrations studied in Al-Mg alloys. An approximate linear relationship is found between the restraining force and the solute concentration in a distributed solute approach. In addition, the extrinsic dislocations are found to completely pin both  $7.785^\circ$  and  $23.07^\circ$  boundary motion at low driving forces in pure Al at 300K. The MD results do not reveal significant qualitative differences of the pinned boundary structure for the low and high angle boundaries and will be discussed in terms of the previous experimental observations.

## Acknowledgements

The author, Md. Jahidur Rahman, would like to express his sincere gratitude to his supervisor Prof. Jeffrey J. Hoyt for his valuable guidance, encouragement and patience throughout the course of this doctoral study. I am indebted to Dr. Hoyt for his suggestions and constructive instructions regarding this research subject that helps me to develop comprehensive understanding and technical skills. I appreciate his motivational support and extreme dedication to accomplishment of this research work. I wish to acknowledge my co-supervisor Dr. Hatem Zurob for his deliberate help to overcome a number of critical problems during the project work. The meetings with Dr. Zurob were exceptionally inspiring. It has been sincere privilege to me to have Dr. Gary Purdy as my committee members. His insightful inputs and comments during the supervisory committee meetings were very useful for this research work. The knowledge, I gained from these three professors, will be carried with me in my entire life.

Dr. Yves Brechet deserves a great deal of thanks for his helpful discussions and advice in the initial period of the project during the course ‘Physically based modelling’. The communications with David Olmsted regarding ‘Lambda integration technique’ are highly appreciated. The author is also pleased to thank Yuri Mishin for the conversations with him in TMS annual general meeting 2013.

The author would like to acknowledge the financial support for this research work by a Natural Sciences and Engineering Council of Canada (NSERC) discovery grant entitled ‘Microstructure evolution and optimization in metals’. The facilities of high performance computing resources to carry out this research work have been provided by Shared Hierarchical Academic Research Computing Network (SHARCNET).

The author intended to admit that the discussions in the weekly group meetings of computational materials science research group were very productive and enlightening. In particular, I have been benefited a lot through the conversations with my colleagues Huajing Song and Peyman Saidi. I gratefully appreciate their assistance. I would like to take this opportunity to acknowledge the past and present graduate students of JHE-356 office for their great company and support to me.

Finally, I would like to offer my best regards and sincere gratitude to my parents for their eternal love, endless support and encouragement for all my endeavours. Their souls and shadows are always with me whenever I am away from them and such comfort provides me extreme inspiration for my success. At last, but not the least, I am grateful to my wife, Shirajum Munira Roma, for her enduring love, understanding and sacrifices to me. Her every effort of keeping me healthy is much appreciated. The unwavering support and care of my wife helps me greatly to complete my doctoral study.

## Table of Contents

Abstract .....	iii
Acknowledgements .....	iv
Table of Contents .....	v
List of Figures .....	vii
List of Tables .....	xiii
List of Symbols .....	xiv
Dedication .....	xvii
<b>1    Introduction .....</b>	<b>1</b>
1.1    Application of Al and Al-Mg Alloys .....	1
1.2    Grain boundary and its properties .....	2
1.3    Importance of low angle grain boundary mobility .....	4
1.4    Role of solute atoms on the grain boundary motion .....	6
1.5    Role of extrinsic dislocations on the grain boundary motion .....	7
1.6    Objective of the thesis .....	11
<b>2    Low angle grain boundary mobility determination .....</b>	<b>13</b>
2.1    Experimental methods for determining grain boundary mobility .....	13
2.2    Computational techniques for determining grain boundary mobility .....	17
2.3    Significant results of previous studies .....	21
2.4    Embedded atom method (EAM) interatomic potential .....	30
2.5    Simulation Procedure .....	30
2.6    Application and results of random walk (RW) method .....	32
2.7    Application and results of artificial driving force (ADF) method .....	35
2.8    Activation energy calculation and discussions .....	45
2.9    Employment of different extrapolation functions .....	49
2.10    Summary of the chapter .....	51
<b>3    Solute pinning effect on low angle grain boundary motion .....</b>	<b>53</b>
3.1    Literature review .....	53
3.2    Simulation details .....	59
3.3    Semi grand canonical ensemble (SGCE) .....	61

3.4	Application of driving force .....	62
3.5	Results and discussion .....	63
3.6	Distributed solute approach .....	69
3.7	Solute pinning constant measurement .....	72
3.8	Summary of the chapter .....	75
<b>4</b>	<b>Extrinsic dislocation pinning effect on low angle grain boundary motion .....</b>	<b>76</b>
4.1	Literature review .....	76
4.2	Simulation Procedure .....	80
4.3	Application of artificial driving force technique .....	81
4.4	Results .....	82
4.5	Discussion .....	89
4.6	Summary of the chapter .....	92
<b>5</b>	<b>Conclusion .....</b>	<b>94</b>
<b>6</b>	<b>Future Work .....</b>	<b>97</b>
	<b>References .....</b>	<b>99</b>

## List of Figures

### Chapter – 1

Fig. 1.1	Use of Al-alloys in the automotive parts of Audi – A8 .....	1
Fig. 1.2	Low angle grain boundary: comprised of a set of discrete dislocations ....	3
Fig. 1.3	Subgrain growth process, (a) formation of nucleus, (b) growth of subgrain, (c) the nucleus reaches critical size to become viable nucleus for growing .....	5
Fig. 1.4	Grain boundary mobility in aluminum (a) and activation enthalpy (b) vs. impurity level. The open and filled symbols represent the misorientation angle of $38.2^\circ$ and $40.5^\circ$ respectively .....	7
Fig. 1.5	Variation of activation enthalpy of grain boundary motion in pure aluminum in 1.5(a) and boundary mobility at 400K in 1.5(b) and 900K in 1.5(c) as a function misorientation .....	10
Fig. 1.6	Interactions of grain boundary with network dislocations in (a) HAGB and (b) LAGB during the boundary migration .....	11

### Chapter – 2

Fig. 2.1	Schematic diagram of the sample geometry of Sun and Bauer technique .....	14
Fig. 2.2	Schematic illustration of bicrystal arrangement for boundary movement investigation with external driving force .....	14
Fig. 2.3	Illustration of the grain boundary motion monitoring technique .....	15
Fig. 2.4	Specimen geometry and its holder for the application of external stress on the grain boundary .....	16
Fig. 2.5	The initial bicrystal geometry of the simulation cell with the half loop .....	17
Fig. 2.6	The asymmetric planar grain boundary in a bicrystal geometry with free surface normal to the interface .....	18
Fig. 2.7	Snapshot of the grain boundary fluctuation showing the height of interface .....	19

Fig. 2.8	Bicrystal geometry of the simulation cell used for artificial driving force is method .....	19
Fig. 2.9	Snapshot of the simulation showing the 1-D random walk of grain boundary around its average position .....	20
Fig. 2.10	Grain boundary migration rate as function of driving pressure at different low annealing temperatures .....	21
Fig. 2.11	SEM micrograph of material deformed 70% at 350°C with (a) no annealing, (b) annealing for 3 hour at 300°C .....	23
Fig. 2.12	The changes in misorientation angle with the subgrain size as the annealing proceed .....	24
Fig. 2.13	Variation of low angle boundary mobility with misorientation in the regime $2.5^\circ < \theta < 5.5^\circ$ .....	25
Fig. 2.14	The boundary is rough at 1400K and moves continuously while at 800K boundary is smooth and migrates in step .....	26
Fig. 2.15	Mobility as a function of misorientation in EAM Ni at 1400K for 388 simulated grain boundaries .....	27
Fig. 2.16	Distribution of smooth boundary as function of temperature measured in EAM Ni .....	27
Fig. 2.17	Grain growth in polycrystal Ni containing different fraction smooth boundary computed from a mesoscale simulation .....	28
Fig. 2.18	Grain boundary mobility vs. misorientation angle determined using different MD techniques .....	29
Fig. 2.19	Dependence of different region of grain boundary migration mechanism on the applied driving force and temperature for symmetric sigma-5 boundary .....	29
Fig. 2.20	Bi-crystal simulation geometry, at 300K, containing a [112] symmetric tilt $7.785^\circ$ boundary with free surfaces at both ends. The position of the interface is shown with a solid line .....	31
Fig. 2.21	Schematic diagram of the dislocation arrangement in low angle symmetrical grain boundary .....	32
Fig. 2.22	A typical plot of centro-symmetry parameter as a function of x-position .....	33
Fig. 2.23	1-D random fluctuation of grain boundary position with time at 500K for the [112] tilt boundary with a misorientation of $7.785^\circ$ .....	34
Fig. 2.24	Time evolution of mean square displacement of grain boundary position at 500K for the $7.785^\circ$ misoriented LAGB .....	35

Fig. 2.25	Schematic illustration of the order parameter profile as a function of the distance normal to the boundary. For OP higher than $\xi_{hi}$ , potential energy is assigned and for OP less than $\xi_{lo}$ , zero potential energy is added ..... 36
Fig. 2.26	A schematic profile of the applied potential as a function of order parameter ..... 37
Fig. 2.27	Snapshots of the grain boundary migration with 0.0008 eV/atom driving force at 300K in pure Al. Free surfaces at the end of simulation cell normal to the interface ..... 40
Fig. 2.28	Potential energy as a function of time during the grain boundary migration with 0.0008 eV/atom driving force at 300K ..... 41
Fig. 2.29	Migration of the grain boundary with simulation time under applied force ..... 42
Fig. 2.30	Grain boundary velocity ( $v$ ) vs. applied driving force ( $P$ ) for the entire span of applied driving forces for the $7.785^\circ$ LAGB. GB velocity is calculated using Eq. 2.8 ..... 43
Fig. 2.31	Interface velocity ( $v$ ) plotted as a function of driving force ( $P$ ) in the regime of low driving force, from which the mobility is extracted. Error bars denote 95% confidence limits. The velocity is calculated using Eq. 2.8 ..... 44
Fig. 2.32	Arrhenius plot of LAGB mobility ( $M$ ) versus inverse temperature ( $T$ ). Mobilities from both ADF and RW methods are presented here. The inset shows the results at $T=300K$ and illustrates that the two MD techniques agree within uncertainty ..... 45
Fig. 2.33	Grain boundary mobility ( $M$ ) in pure Al plotted as a function misorientation angle ( $\theta$ ) at 300K from both ADF and RW method. The open symbols, in RW method, indicate that the mean square displacement of grain boundary was not enough to compute mobility ..... 46
Fig. 2.34	Grain boundary velocity ( $v$ ) vs. driving force ( $P$ ) plotted for $23.07^\circ$ and $7.785^\circ$ misorientation at 300K showing a driving force threshold needed to start grain boundary movement for the HAGB ..... 47
Fig. 2.35	Grain boundary mobility ( $M$ ) plotted as a function of misorientation ( $\theta$ ) at $T = 700K$ for both ADF and RW technique ..... 48
Fig. 2.36	GB mobility ( $M$ ) plotted at different lower cutoff ( $\xi_{lo}$ ) of order parameter (OP) showing variation of mobility with OP for $11.655^\circ$ and $23.07^\circ$ boundaries at 700K ..... 49

Fig. 2.37	Profile of potential energy vs. normalized order parameter for all the investigated artificial functions. All profiles show the same features except the magnitude of slope at the interface. For Tanh function, $a=1$ is used in this plot .....	50
Fig. 2.38	LAGB velocity plotted versus driving force at different artificial functions for the comparison of mobility .....	51

### Chapter – 3

Fig. 3.1	Cahn model: the applied driving force as a function of boundary velocity at different solute concentration. The dashed part shows the breakaway region .....	55
Fig. 3.2	Schematic illustration of (a) cusp formation on solute atoms on the grain boundary, and (b) pinning force ( $F_C$ ) on the cusp forming solute .....	57
Fig. 3.3	Simulation geometry of Al-2%Mg binary system with [112] symmetric tilt $7.785^\circ$ boundary at 300K. The golden colour atoms are solute atoms (Mg). The solid line shows the position of the grain boundary and there are free surfaces at both ends .....	60
Fig. 3.4	Principle of the Semi grand canonical ensemble (SGCE) approach in the Monte Carlo simulation showing the change in solute concentration with the variation in chemical potential differences between the species .....	61
Fig. 3.5	Grain boundary velocity vs. applied driving force in high driving force limit for the $7.785^\circ$ boundary in Al-2%Mg at 300K .....	64
Fig. 3.6	GB velocity as a function of applied driving force in high driving force limit for the $7.785^\circ$ boundary in Al-0.2%Mg at 300K .....	65
Fig. 3.7	Threshold driving force for all examined solute concentration, along with pure Al, as a function of boundary misorientation at 300K .....	66
Fig. 3.8	Simulation snapshot showing the segregation of Mg atoms (golden color) at the grain boundary for Al2%Mg system for the $7.785^\circ$ boundary at 300K .....	67
Fig. 3.9	The solute distribution profile the direction normal to the grain boundary for the $7.785^\circ$ boundary in Al-2%Mg alloy at 300K .....	68
Fig. 3.10	The equilibrium Al-2%Mg binary system with $7.785^\circ$ boundary at 300K. The lower panel clearly shows that Mg atoms are distributed in a confined region away from the grain boundary .....	70
Fig. 3.11	PE/atom vs. time for the $7.785^\circ$ boundary in Al-2%Mg alloy at 300K with 0.008 eV/atom applied driving force .....	71

Fig. 3.12	GB velocity as a function of driving force for the $7.785^\circ$ boundary in Al-0.2%Mg at 300K. The slope will almost passes through the origin .....	72
Fig. 3.13	$(V - MP)$ as a function of solute concentration for binary systems: Al with 0.1%, 0.15% and 0.2% Mg and pure Al for the $7.785^\circ$ boundary at 300K .....	73

## Chapter – 4

Fig. 4.1	Activation energy of grain boundaries as a function of misorientation for pure tilt (O) and mixed ( $\Delta$ ) boundary .....	77
Fig. 4.2	Schematic view of the dislocation arrangement at the LAGB in Lim's study, where intrinsic dislocations are shown in blue with Burgers vector $\mathbf{b}_1$ and extrinsic dislocations are pink with Burgers vector $\mathbf{b}_2$ .....	79
Fig. 4.3	Bicrystal simulation system of pure Al with [112] symmetric tilt $23.07^\circ$ boundary at 300K. It is clear that the right crystal contains two dislocations and there are free surfaces at both ends .....	81
Fig. 4.4	Potential energy change with time under the application of 0.002 eV/atom driving force on $7.785^\circ$ boundary. The steady state part corresponds to the complete pinning of the boundary.....	83
Fig. 4.5	Gliding of extrinsic dislocation due to the interaction with $7.785^\circ$ boundary with the application of 0.002 eV/atom. The square boxes are showing the position of the extrinsic dislocations.....	84
Fig. 4.6	Annihilation of extrinsic dislocation due to the interaction with $7.785^\circ$ boundary with the application of 0.01 eV/atom. The square boxes are showing the position of the extrinsic dislocations .....	85
Fig. 4.7	Motion of LAGB to the right in Lim's study with application stress higher than threshold stress. Gliding of extrinsic dislocations towards each other (shown in red) at $t = 30000$ that leads to annihilation of those dislocations .....	86
Fig. 4.8	Pinning of $23.07^\circ$ boundary and gliding of extrinsic dislocation with the application of 0.005 eV/atom .....	87
Fig. 4.9	Annihilation of extrinsic dislocation due to the interaction with $23.07^\circ$ boundary with the application of 0.015 eV/atom. The boxes are showing the position of the extrinsic dislocations .....	88
Fig. 4.10	Spatial arrangement of the intrinsic dislocations is shown based on the PE/atom for (a) $7.785^\circ$ and (b) $23.07^\circ$ boundary .....	90

Fig. 4.11	Arrhenius plot of grain boundary diffusion coefficient with inverse temperature for both sub grain boundary and high angle grain boundary .....	91
Fig. 4.12	Activation energy of grain boundary diffusion, in the direction parallel and perpendicular to the tilt axis, as a function of misorientation .....	92

## **List of Tables**

### **Chapter – 2**

Table 2.1	The rotation matrix of transformation and the nearest neighbour atoms at different axis for crystal-1 of $7.785^\circ$ boundary at 300K. The atom positions are in terms of lattice parameter .....	38
-----------	---	----

## List of Symbols

### Chapter – 1

$\Sigma$	Coincident lattice site in every this number of atoms at the interface
$r_c$	Critical subgrain size that is viable to initiate recrystallization
$\gamma_{gb}$	Grain boundary energy
$G(t)$	Stored energy that is the driving force of LAGB motion
$M_{sb}$	Low angle grain boundary mobility
$v_{sb}$	Subgrain growth rate
$r$	Subgrain size

### Chapter – 2

$P$	Applied driving pressure for grain boundary motion
$A$	Area of the grain boundary plane
$u_\xi$	Artificial potential energy per atom
$\Omega_s$	Atomic volume of the fcc Al
$\bar{h}(t)$	Average grain boundary position
$\bar{D}$	Average grain size
$k_B$	Boltzman constant
$\kappa_\gamma$	Capillary driving force
$V$	Chosen applied potential
$D$	Diffusion coefficient
$p$	Driving force given by a curved boundary
$f_o$	fraction of smooth boundary
$\kappa$	Grain boundary curvature
$M$	Grain boundary mobility
$v$	Grain boundary velocity
$\theta_{gb}$	High angle grain boundary misorientation
$\bar{D}_0$	Initial grain size

$r_0$	Initial subgrain size
$I_m$	Intermediate X-ray intensity corresponds to grain boundary
$\eta$	Intrinsic thermal noise
$a$	Inverse of the grain curvature
$I_0$	Maximum X-ray intensity corresponds to grain 1
$\langle \bar{h}^2 \rangle$	Mean square displacement of grain boundary
$T_m$	Melting temperature
$I_u$	Minimum X-ray intensity corresponds to grain 2
$\theta$	Misorientation angle at the boundary
$\omega_i$	Normalized order parameter
$N_1$	Number of atoms in crystal-1
$N_2$	Number of atoms in crystal-2
$N$	Number of nearest neighbours
$\xi_i$	Order parameter for atom $i$
$r_j^I$	Position of nearest ideal lattice site in a crystal with orientation $I$
$E_T$	Potential energy (PE) of the entire system
$E_1$	Potential energy of the reference (growing) crystal
$E_2$	Potential energy of the shrinking crystal
$M^*$	Reduced mobility of grain boundary
$T_c$	Roughening temperature that divides smooth and rough grain boundary
$\dot{E}$	Slope of potential energy vs. time plot
$\gamma_{sb}$	Sub-boundary energy
$\theta_{sb}$	Sub-boundary misorientation
$\sigma$	Surface tension of the curved boundary
$T$	Temperature
$N_T$	Total number of atoms
$\vec{R}_i$	Vector distance of particular nearest neighbour from central atom
$x$	x co-ordinate of the simulation cell
$y$	y co-ordinate of the simulation cell
$z$	z co-ordinate of the simulation cell

### Chapter – 3

$c$	Average concentration of the distributed solutes
$c_b$	Boundary solute concentration
$E(x)$	Boundary–solute interaction energy
$\lambda$	Boundary thickness
$\Delta G$	Dissipation of Gibbs energy due to diffusion
$C$	Impurity concentration
$C_o$	Impurity concentration in the bulk material
$P_i$	Impurity drag force
$\beta$	Impurity drag parameter at high velocity
$\alpha$	Impurity drag parameter at low velocity
$N_v$	Number of atoms per unit volume
$n_b$	Number of atoms per unit volume inside the boundary
$R$	Radius between the solute pinning points
$\delta$	Solute pinning constant
$F_C$	Solute pinning force on the boundary motion
$P_C$	Solute restraining pressure on the migrating boundary

### Chapter – 4

$Q$	Activation energy of grain boundary diffusion
$\mathbf{b}_2$	Burgers vector of extrinsic dislocations
$\mathbf{b}_1$	Burgers vector of intrinsic dislocations
$\zeta$	Dislocation line directions
$a$	lattice parameter

## **Dedication**

I would like to dedicate my PhD thesis  
to  
my parents:

Md. Iftekhar Hossain (father)  
and  
Nasrin Akter (mother)

## CHAPTER 1

### Introduction

#### 1.1 Applications of Al and Al-Mg Alloys

The reduction in weight and savings of fuel consumption make Al-alloys potential candidates for automotive purposes. Besides that, its corrosion resistance characteristics have lead automakers to offer longer warranties against body rust-out and component failure. Applications of aluminum alloys have been growing in automotive industries over the years, both in absolute quantity per car and as a percentage of vehicle weight. The Aluminum Association Inc., in 2001, reported that [1] the average aluminum content of a U.S. car increased up to around 250 pounds in 27 years from nearly 54 pounds in 1960, which is equivalently about 8 percent of the total weight from 1.4 percent. Aluminum has also been used in the bodies of U.S. Postal Service delivery vans for the last 28 years.

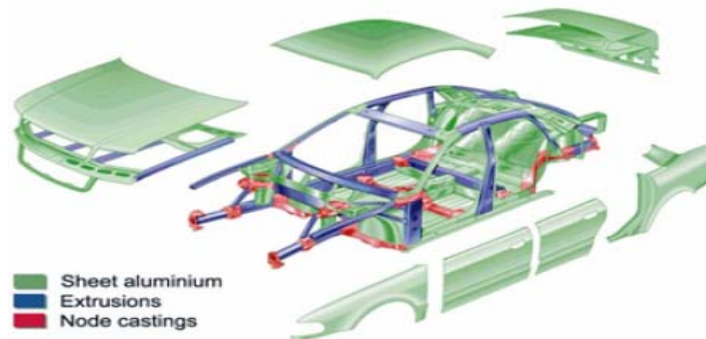


Fig. 1.1: Use of Al-alloys in the automotive parts of Audi - A8 (courtesy to master's thesis of Sanjay Kumar Vajpai) [2] [<http://www.keytometals.com>].

Magnesium is one of the most widely used alloying elements for automotive aluminum and is the principal element in the 5xxx series alloys. Al-Mg alloys are of great interest in commercial uses as they provide high strength with a wide range of ductility and durability. Al-Mg alloys are readily weldable and have excellent resistance to corrosion, even in marine environments and salt-water sensitive shore applications. Due to the high formability, these alloys are also used to produce beverage cans as well. The recyclability of Al-Mg alloys provides both economic and environmental benefits. The major applications of Al-Mg alloys in the automotive industries include interior body

panels and components such as splash guards, heat shields, air cleaner trays and covers, structural and weldable parts, load floors (sheets) and engine accessory brackets and mounts [2]. Mg is one of the main elements in 6xxx series automotive Al-alloys (Al-Mg-Si) which are usually utilized in the outer body panels. Al-Mg-Si alloys provide good quality strength as they can be strengthened through precipitation hardening. They also possess very good formability meeting the requirements of the forming of sheets for the outer panels. In Fig. 1.1, the general uses of Al-alloys in automotive parts are shown for the Audi - A8.

## 1.2 Grain boundary and its properties

Most modern technical applications involve polycrystalline materials. The mechanical, physical and chemical properties of those materials are mainly governed by their microstructures and defects such as grain boundaries, vacancies and dislocations that are introduced during different non-equilibrium processes. Microstructure is defined as the accumulation of some grains with varying orientation and as the distribution of internal defects, phases and grain size. In a polycrystalline material, the grain boundaries are directly linked to second phase formation, grain growth and coarsening. Hence grain boundary properties play an important role in the microstructural evolution during thermo-mechanical processing since the grain structure forms and changes through motion of the grain boundaries.

The boundary movement largely controls microstructural parameters such as grain size and texture, which in turn are considered to be key parameters in the optimization of some materials processing techniques. The thermodynamics and kinetics of the grain boundary migration are of fundamental importance [3,4] from the view point of both the technologists and the scientists. Therefore, an improved understanding of the grain boundary migration and its associated features are very significant for the development of microstructure evolution modelling and hence would be useful for a wide range of processing applications. Grain boundary motion is the most important atomistic mechanism that occurs during most solid-state microstructure transformations, for example recovery, recrystallization, grain growth.

Grain boundary (GB) is the interface between two differently oriented grains and the crystallography of GB can be defined using 5 degrees of freedom in terms of the macroscopic geometry [5]. Three parameters are required to specify the rotation between the crystals, such as rotation angle/axis and 2 parameters are needed to characterise the plane of the grain boundary. In addition to macroscopic degrees of freedom, GB can be defined with some microscopic freedom, such as translation of the lattices in the plane of the boundary. The misorientation of the boundary is amount of rotation, with respect to a reference frame, that is required to rotate one crystal of fixed orientation into that of another one. In place of misorientation, disorientation has also been in some literature to define the boundary crystallography. Disorientation is defined as the minimum possible

rotation to connect two differently oriented crystals. Grain boundary motion is significantly affected by all degrees of freedom [6], as an example, in spite of having same misorientation,  $\langle 111 \rangle$  incoherent twin grain boundary motion is comparatively faster compared to that of  $\langle 111 \rangle$  coherent twin boundary [7].

Grain boundary motion or equivalently the mobility of boundary migration strongly depends on extent of the crystallographic misorientations between the neighbouring crystals. Grain boundaries can be divided into two different categories, namely low-angle grain boundaries (LAGB) and high-angle grain boundaries (HAGB). Basically this categorization is based on the orientation difference of atomic arrangement between the crystals and whether they consist discrete dislocations in their structure at the boundary. HAGBs are the interfaces between crystals with large misorientation angle while LAGBs are formed between the grains with almost identical orientations. Usually grain boundaries with  $11^\circ$  to  $15^\circ$  misorientation angle or less are considered as LAGB while the HAGBs are defined as boundaries with misorientation larger than  $11^\circ \sim 15^\circ$ . LAGBs are comprised of a set of discrete dislocations and are generally considered as a  $\Sigma 1$  grain boundary. The  $\Sigma$ -value means there is coincident lattice site in every this number of atoms at the interface of two grains. In Fig. 1.2, a typical low angle grain boundary is shown with a misorientation angle  $\alpha$ .

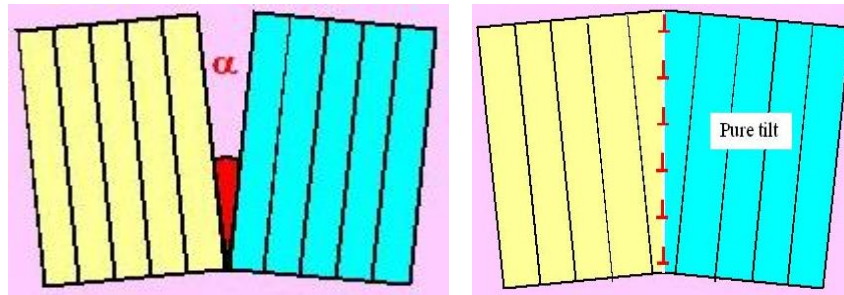


Fig. 1.2: Low angle grain boundary: comprised of a set of discrete dislocations [8].

Grain boundary mobility is defined as the constant of proportionality between the velocity of grain boundary motion and applied driving force. The expression for determining GB mobility is as follows:

$$v(T) = M(\theta, T)P \quad (1.1)$$

where  $v$  is the grain boundary velocity,  $M$  is the boundary mobility and  $P$  is the applied pressure. As shown in Eq. 1.1, the grain boundary mobility depends on the misorientation ( $\theta$ ) and the temperature ( $T$ ) and these effects are reported in a number of studies. In an extensive Molecular Dynamics (MD) study, Olmsted et. al. [9] described the dependence of the mobility ( $M$ ) on the misorientation ( $\theta$ ) showing decrease in  $M$  with increasing  $\theta$  in EAM pure Ni. Same trend of mobility with misorientation is also shown in another MD study in Cu [10] that is in agreement with a theoretical prediction [11]. In an experimental

study in pure Al, Winning et al. [12] showed lower mobility for low angle boundary than that of high angle boundary at low temperature (400K) and the behaviour is opposite at high temperature (900K). All of these studies will be discussed in Section 2.3 in detail. Olmsted et. al. [9] also studied the temperature dependence of boundary mobility and reported that the mobility changes with temperature following an Arrhenius type function. Most of the experimental and computational studies demonstrated the same behaviour for  $M$  vs.  $T$  plot. The Arrhenius relation is as follows:

$$M = M_0 \exp\left(-\frac{Q}{RT}\right) \quad (1.2)$$

where  $M_0$  is the pre-exponential factor,  $R$  is gas constant and  $Q$  is the activation energy of the grain boundary motion.  $Q$  can be determined from the slope of the Arrhenius plot.

### 1.3 Importance of low angle grain boundary mobility

Recrystallization is one of the most important thermo-mechanical processes. It is conducted to release the deformed stress through grain refinement and hence controls the texture of the microstructure. To date, some semi-empirical models [13,14] have been developed to predict and control this process through the investigation of recrystallization time, critical temperature, critical strain, final grain size etc. and several analytical models [15-23] have been proposed to describe recrystallization kinetics and texture. The models predict that the nucleation of recrystallized grains are directly linked to the subgrain size and its growth kinetics and hence sub-boundary mobility. Subgrains are generally formed when materials are annealed in a cold worked condition, the network of dislocation divides the material into small region/cell and accordingly the arrays are referred to as subgrain boundaries. Actually, the neighbouring regions in the sub-grain network form low angle boundaries at their interface. So, the subgrain growth of the material is critically controlled by the mobility of the low angle grain boundary. An example of the subgrain growth process is shown in Fig. 1.3.

According to Bailey and Hirsch [24], the driving force for stress induced grain boundary migration is  $G(t) = 2\gamma_{gb}/r$ , where  $G(t)$  is the stored energy,  $\gamma_{gb}$  is the grain boundary energy and  $r$  is size of the subgrain. A nucleus of the subgrain will form at the place where the subgrain will possess lower stored energy compared to its surroundings which is shown in Fig. 1.3(a). With time the growth will progress and the subgrain size will increase from  $r_1$  to  $r_3$  accordingly (Fig. 1.3(b)). The continuous growth process will reduce the term  $2\gamma/r$  in turn and once its value falls below the stored energy, the nucleus will start to grow into other neighbouring grains (Fig. 1.3(c)). At this state the size of the

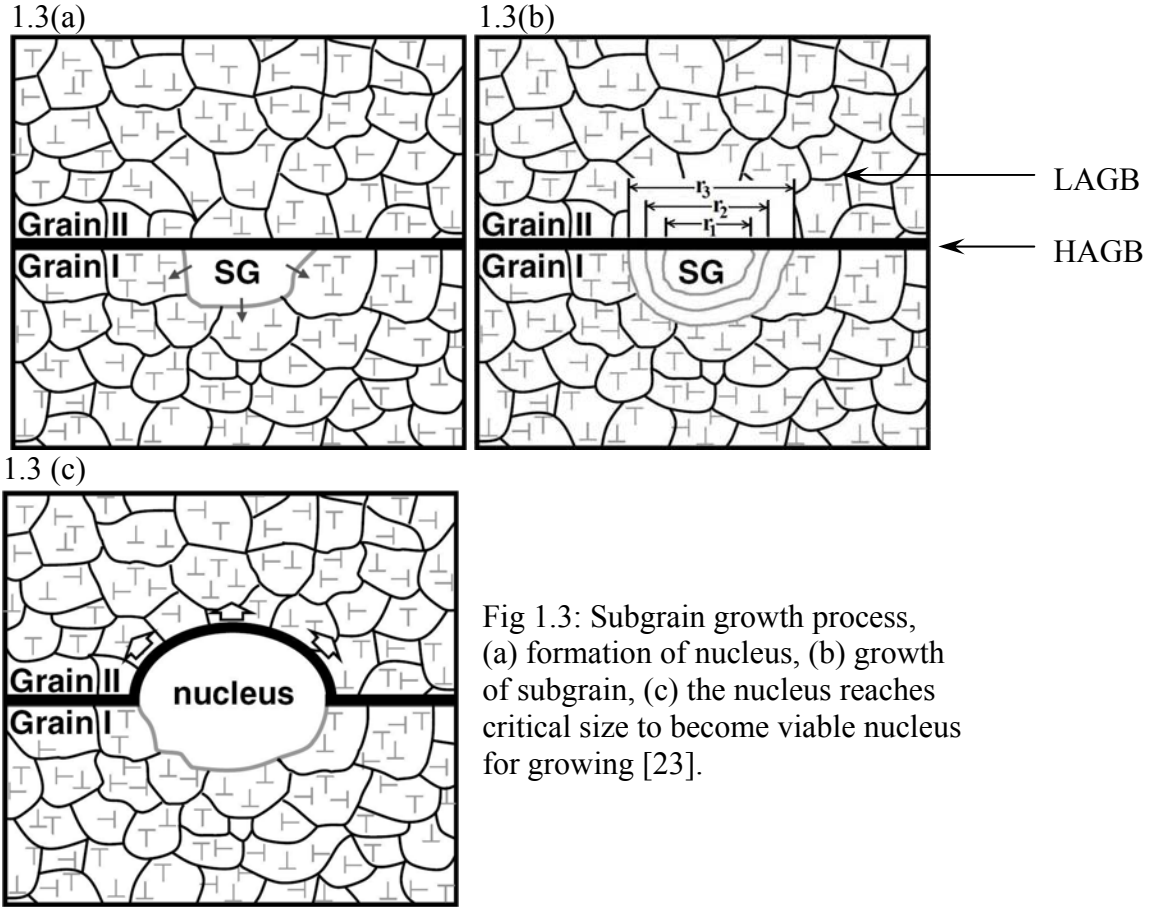


Fig 1.3: Subgrain growth process, (a) formation of nucleus, (b) growth of subgrain, (c) the nucleus reaches critical size to become viable nucleus for growing [23].

subgrain nucleus is considered to reach a critical value which is feasible to grow. The growth of the subgrains, with critical size, will initiate and the subsequently lead the recrystallization. The critical size of the recrystallization nucleus is:

$$r_c(t) = \frac{2\gamma_{gb}}{G(t)} \quad (1.3)$$

Therefore, the subgrain growth or equivalently the recovery process and its kinetics largely control the nucleation step of the recrystallization. The formation of viable recrystallization nuclei critically depends on the rate at which the subgrain will grow from  $r_1$  to  $r_3$  and eventually reach the critical size. As these grains form low angle boundaries at their interface, the motion of the dislocations will dictate the growth kinetics of these grains. The studies, that have been conducted to describe the mechanism of the dislocation movement, expressed the rate of subgrain growth as [18,25-26]:

$$v_{sb}(t) = M_{sb} G(t) \quad (1.4)$$

where,  $v$  is the velocity of the subgrain growth,  $M$  is the mobility of the sub-boundaries and  $G(t)$  is the driving force. Clearly, the mobility of the low angle boundary between the subgrains is very important to determine the rate of its growth to direct the recovery process and eventually to control the nucleation of the recrystallization.

The experimental measurements of the grain boundary mobility provide an average result determined from some growth processes [27-31]. The complicated activation and motion of grain boundaries results in less experimental investigation for low angle grain boundary migration. The motion of low angle boundaries is also rarely studied computationally for both pure and alloy systems. Due to the lack of LAGB mobility studies, the recovery kinetics and hence the nucleation process of the recrystallization are still poorly understood. This scenario has motivated the present study to observe the low angle grain boundary motion in detail in the pure aluminum system.

#### **1.4 Role of solute atoms on the grain boundary motion**

The grain boundary motion plays an important role in developing the microstructure of polycrystalline materials during different thermo-mechanical processes and hence controls the mechanical properties. Due to the significance of boundary motion kinetics, a number of studies have been carried out to determine the mobility and its dependence on various defects. As nearly all real materials contain at least some impurities or solutes, considerable attention has been paid to the effect of such defects on the boundary mobility. All the relevant studies have concluded that the presence of impurities or solutes provides resistance to the boundary movement. As impurities provide a drag effect on the interface motion, this phenomenon has been used in practical applications to control the grain size and hence improve the mechanical properties.

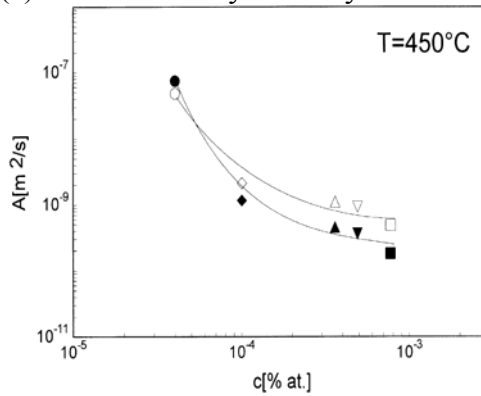
Due to the importance of the solute drag effect during different thermo-mechanical processes, it has been investigated in detail [32-43] since the late 1950s. To develop a fundamental understanding of solute drag, several classic models [32, 37-39] have been published. Among those models, Cahn's [38] and Hillert's [39] approaches are considered to be two leading theoretical analyses in the literature of solute drag. Over the last two decades, a number of studies [44-64] have been conducted to capture different aspects of the drag effect on boundary migration by extending the Cahn and Hillert models. Summarizing all the studies, it can be stated that the presence of even very small amount of solute can retard the grain boundary motion significantly. For example, in a study of static recrystallization, Hutchinson et al. [44] has described the importance of solute drag effect explicitly. The authors reported that 0.05at% Nb solute impedes the grain boundary motion very strongly in the ferrite phase in Nb-steel.

As the grain boundary kinetics is important, a huge number of experimental studies [12,28,31,65-73] have been conducted to determine the mobility of high angle boundaries. In addition to requiring sophisticated sample preparation methods,

experimental studies of grain boundary mobility are complicated by the presence of impurities, set up of grain boundaries with proper misorientation, controlling of pressure and other parameters. Therefore, in recent years computational approaches [74-84] have been employed to determine the intrinsic grain boundary mobility in several metal and model systems. From all the previous studies, it can be concluded that the computational approaches provide much higher boundary mobility compared to that of experiments. This discrepancy is usually attributed to the presence of impurities in real materials in the experimental measurement.

In a relevant experimental study, Molodov et al. [28] have investigated the grain boundary motion and its dependence on the effect of purity. It was found that the mobility and the activation enthalpy of migration strongly depend on purity level for  $\Sigma 7$  grain boundaries in aluminum. They have examined Al with  $0.4$  to  $7.7 \times 10^{-4}$  at% impurity at

1.4(a) Grain boundary mobility



1.4(b) Activation enthalpy of boundary motion

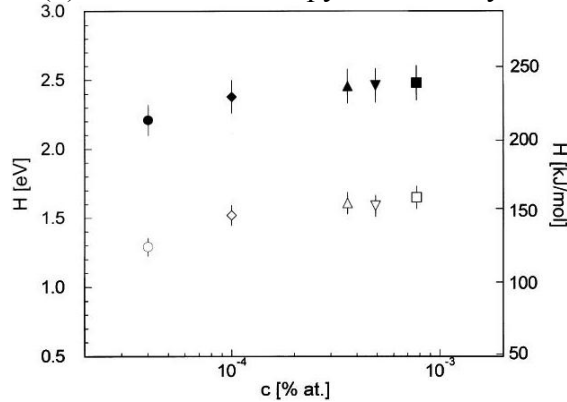


Fig. 1.4: Grain boundary mobility in aluminum (a) and activation enthalpy (b) vs. impurity level. The open and filled symbols represent the misorientation angle of  $38.2^\circ$  and  $40.5^\circ$  respectively [28].

different temperatures. The mobility was decreasing with an increase in the solute content in the system and in the range of impurity concentration they have investigated, the mobility was observed to decrease by more than two orders of magnitude. The effect of purity level is illustrated in Fig. 1.4. The variation grain boundary mobility and activation enthalpy with impurity content are shown in panel 1.4(a) and 1.4(b) respectively. The reason for lower mobility with impurity content is attributed to the high activation energy for the grain boundary migration due to the motion of impurity atoms at the interface. The boundary activation consists of two enthalpies: impurity diffusion and impurity adsorption. Hence the activation energy is raised even with the presence of the lowest impurity content which in turn decreases the boundary mobility.

As we mentioned earlier, due to the importance of solute drag, several works have studied this phenomenon experimentally. But, to date, few computational studies have been conducted to capture the solute drag/pinning effect. This research work will investigate the effect of solute pinning on the motion of grain boundaries in Al-Mg alloys using Molecular Dynamics (MD) simulations. Especially we will focus on low angle grain boundary (LAGB) motion. As MD simulations measure intrinsic mobility, this computational method will provide us a distinct advantage of comparing the boundary mobility of Al-Mg alloy with that of pure Al.

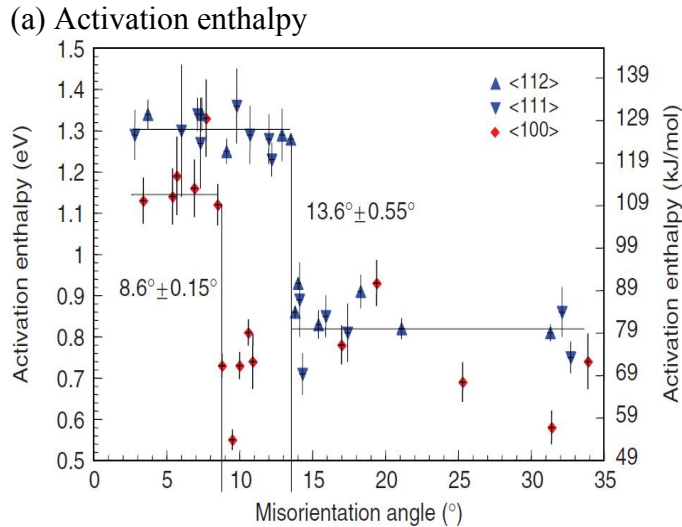
### **1.5 Role of external dislocations on the grain boundary motion**

As mentioned earlier grain boundary properties have been a subject of interest over many years because of their leading role in microstructure evolution. Particularly, grain boundary mobility has received main importance for controlling the mechanical properties due to its effects on the formation of grain structure. Several types of defects, such as network dislocations, vacancies, impurities introduced in the real polycrystalline materials from various thermo-mechanical processes have significant influence on the kinetics of grain boundary motion. Therefore, fundamental understanding of the interaction behaviour of these defects, mainly dislocations, with the migrating grain boundary is very essential.

We have discussed in the last section that the grain boundary mobility derived from computational approach is considerably higher than that of experiments. In addition, all the simulation works consistently provide smaller activation energies for boundary migration in comparison to those measured experimentally [72-73, 74-75]. The reason for this discrepancy is considered to be retarding effect of the impurities on the boundary motion in real materials. In addition to the impurities, the large discrepancy between experimentally measured and simulated grain boundary mobility can be explained in terms of the array of network dislocations that is in general present in any real metal. These external dislocations can act as pinning or drag points for a moving grain boundary and affect the interface kinetics by interacting with that migrating boundary. A small network of dislocations can have a strong effect on the experimentally determined grain

boundary mobility. But to date, the interaction of extrinsic dislocations with the migrating grain boundaries has been paid very limited attention. Therefore, it is interest to investigate the interface motion in the presence of externally introduced dislocations. As Molecular Dynamics studies provide intrinsic mobility, MD simulations can accurately capture the distinct effect individual dislocations on the grain boundary migration.

In a study of particular interest and relevance to this work, Winning et al. [12] measured the grain boundary mobility of symmetric [112], [111] and [100] tilt boundaries in pure Al for a wide range of misorientation from a stress induced experiment. They have investigated both the low and high angle planar boundaries. It was concluded by the authors that the grain boundary mobility is practically constant in both the high angle and low angle regime at a certain temperature. But, there is a transition misorientation angle that divides the high- and low-angle region showing a discontinuous step in the behaviour of grain boundary properties such as boundary mobility and activation enthalpy. The transition angle was marked as  $13.6 \pm 0.55^\circ$  which is independent of tilt boundary plane and impurity content. They found that the mobility of the LAGBs is lower than that of HAGBs at low temperature, but at high temperature, the mobility of low angle boundary exceeds that of high angle boundaries in the case of stress induced boundary motion. The results of Winning’s study are illustrated in Fig. 1.5, where the variation of activation enthalpy of grain boundary motion with the misorientation is shown in Fig. 1.5(a), and boundary mobility in Fig. 1.5(b) for low temperature and in Fig. 1.5(b) for high temperature. Fig. 1.5(a) demonstrated that the activation enthalpy for low angle boundary migration is higher than that of high angle boundary.



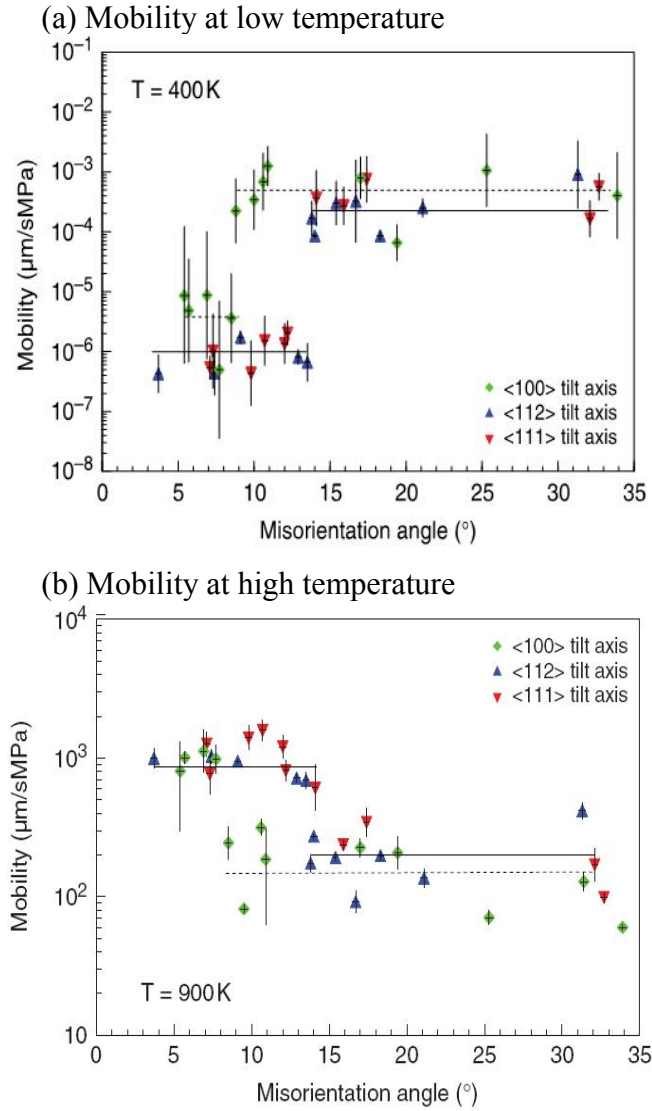


Fig. 1.5: Variation of activation enthalpy of grain boundary motion in pure aluminum in 1.5(a) and boundary mobility at 400K in 1.5(b) and 900K in 1.5(c) as a function misorientation [12].

Winning’s study [67] explained the importance of the interactions of grain boundaries with the network of dislocations present in the grain interior. The reason of the variation of mobility with misorientation was described in terms of the behaviour of extrinsic dislocations interacting with low angle and high angle boundaries. The authors illustrated that, at low temperature, these dislocations will be absorbed by high angle boundary during its migration. In contrast, as a low angle grain boundary (LAGB) is composed of arrays of discrete dislocations, the motion of a LAGB will be hindered by other network dislocations. At low temperature, the dislocation network pins the low

angle boundary strongly and provides lower mobility. These phenomena are illustrated in detail in Fig. 1.6. In this study, we will investigate the interaction of externally induced dislocations with the motion of low and high angle grain boundaries in pure Al to qualitatively validate the Winning's Model.

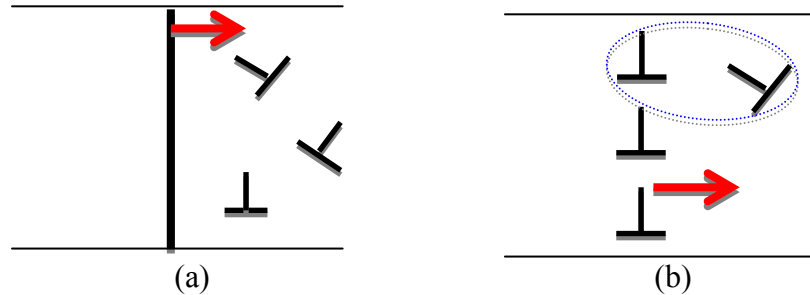


Fig. 1.6: Interactions of grain boundary with network dislocations in (a) HAGB and (b) LAGB during the boundary migration.

## 1.6 Objective of the thesis

The purpose of this research work is focused on the determination of low angle grain boundary (LAGB) mobility in pure Al and investigation of solute and dislocation interaction with the migrating grain boundary in the Al-Mg and pure Al system respectively. LAGB mobility will describe the recovery kinetics and the nucleation of recrystallization and provide some plausible explanations of some experimentally determined LAGB mobility. The solute interaction with the boundary will illustrate the solute pinning phenomenon in Al-Mg alloys using MD simulations and bridge the gap between the mobility values extracted from experiment and computational approach. The study of extrinsic dislocation with low and high angle grain boundary interaction will be useful to qualitatively validate Winning's model of boundary mobility variation with misorientation. The main objectives of the project are described below:

Low angle grain boundary (LAGB) mobility:

- (1) To determine the low angle grain boundary (LAGB) mobility in pure Al at different temperatures and misorientations using some atomistic simulation techniques below the melting point.
- (2) To examine the computational methods in detail for the measurement of low angle boundary mobility and computing the activation energy of the boundary migration to describe the kinetics.
- (3) To compare the MD derived LAGB mobility with the experimental observation and another MD study.

Solute interaction with grain boundary, especially LAGB:

- (1) To compute the low angle grain boundary mobility of Al-Mg alloys as a function of the solute content in the system to observe the effect of solute on the boundary migration.
- (2) To investigate of solute pinning phenomenon using different approaches in MD simulation with varying misorientation.
- (3) To compute the solute restraining force.

Extrinsic dislocation interaction with grain boundary:

- (1) To study the interaction of externally induced dislocation with the low angle and high grain boundary.
- (2) To validate the Winning's model of boundary mobility variation with misorientation qualitatively.

The thesis is organized as follows. The next chapters will describe in detail the determination of low angle grain boundary mobility. In the following two chapters, the grain boundary interaction with solute atoms and dislocation will be investigated. The last section will summarize all the significant results in the conclusion chapter and offer some suggestions in the final chapter. The major chapters will start with the literature review and end with the results and discussions.

## CHAPTER 2

### **Determination of low angle grain boundary mobility**

In this chapter, we will determine the low angle grain boundary (LAGB) mobility in pure Al system utilizing Molecular dynamics (MD) simulations. The mobility will be computed employing two different MD techniques, namely the artificial driving force (ADF) method and the random walk (RW) method, as a function of temperature and misorientation. We will critically analyze both techniques with a detailed comparison. MD derived LAGB mobility and activation energy of LAGB migration will be determined and compared with the experimental observations and the previous MD studies.

#### **2.1 Experimental methods for determining grain boundary mobility**

There are some major problems associated with the experimental investigations of grain boundary mobility, such as properly controlling the composition and purity of the material, accurately producing the crystallography, maintaining the driving force for grain growth and continuously monitoring the boundary displacement. But, Due to the technical importance of grain boundary kinetics in the prediction of microstructural evolution, there exists a vast literature on the determination of the mobility. Most of the experimental studies have been conducted on high angle grain boundary migration while few works on the motion of low angle grain boundary [71-72,85]. Traditionally, experimental measurements of grain growth in polycrystalline metals have been used to extract grain boundary mobility. However, simple growth experiments yield only an average mobility and therefore cannot distinguish the important role of misorientation on the rate of grain boundary motion. A number of experimental works of GB mobility measurement is based on application of driving pressure in different form, such as geometry induced force, applied stress and magnetic field, curvature driven, usage of triple junction.

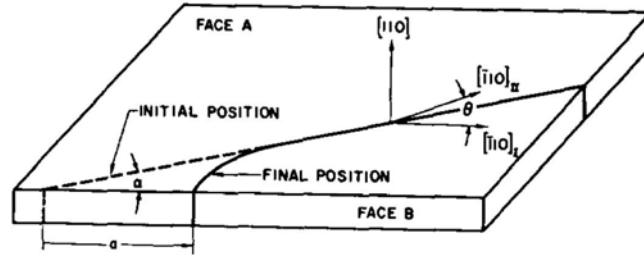


Fig. 2.1: Schematic diagram of the sample geometry of Sun and Bauer technique [67].

Over the past several decades, a number of experimental methods have been developed to measure the mobility for specific boundaries of known orientation. In the early 1970's Sun and Bauer [65] introduced a sample geometry consisting of initially straight boundaries intersecting free surfaces with an acute angle. The boundary then migrates to form minimum energy hyperbolic shapes due to the capillary force acting on it. Such a bicrystal specimen is schematically illustrated in Fig. 2.1. The Sun-Bauer geometry was subsequently used to study the mobility as a function of misorientation in Cu [66], Al [67], and Fe-3.5%Si [68].

In another experimental investigation, Molodov et al. [31] determined the mobility from a curvature driven grain boundary motion by employing bicrystals containing grain boundary loops. The bicrystal, with controlled crystallographic orientation, is set up with a curved interface boundary between the two grains and grown by the so called directional crystallization. The detail of the bicrystal growth is given in Ref. [31]. The grain boundary is allowed to move under the driving force  $p$  given by the surface tension  $\sigma$  of the curved boundary:  $p = \sigma/a$ , where  $a$  is the inverse of the grain curvature that will be shrinking during boundary migration, as shown in Fig. 2.2. This technique was used to investigate the effect of impurities on GB motion in Al [28].

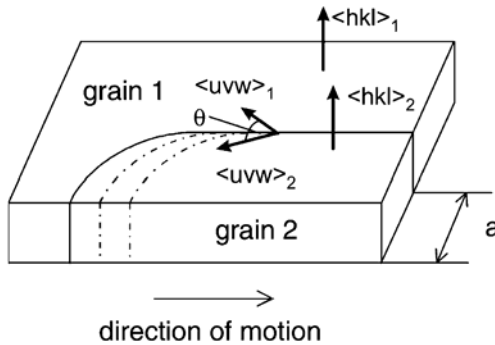


Fig 2.2: Schematic illustration of bicrystal arrangement for boundary movement investigation with external driving force [86]

The position of the moving grain boundary is continuously monitored through a special tracking device which is an X-ray device known as X-ray interface continuous tracking device (XICTD) [86]. The basic method of operation for continuous tracking of

grain boundary is demonstrated in Fig. 2.3 The bicrystal specimen is placed under the monochromatic X-ray beam in such a way that the crystal in one orientation is set in the Bragg condition while the other crystal is not. The X-ray beam, scanned through the sample, provides a distribution profile of the intensity (Fig. 2.3) which shows a sudden change with a sharp gradient at the grain boundary. During the boundary migration, maximum intensity  $I_0$  is observed when the X-ray beam was scanning the surface of grain 1 and after crossing the boundary, minimum intensity  $I_u$  is detected when the X-ray is focused on grain 2. The intermediate intensity reflects the position of the grain boundary. During the motion of the interface, the sample was moved with boundary migration in such a way that the intensity distribution remains the same. Then the velocity of the moving grain boundary is equivalent to the speed at which the specimen was displaced.

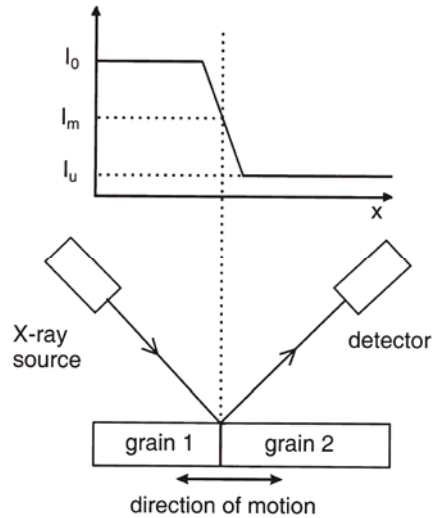


Fig 2.3: Illustration of the grain boundary motion monitoring technique [86].

In addition to a capillary driving force, grain boundary mobility has been measured through the application of a magnetic field in Bi [69] and Zn [70] bicrystal. By monitoring the position of triple junctions during the annealing process, Yang et al. [73] were able to obtain the energy and mobility vs. misorientation for a large number of grains in Al. The boundary mobility is measured from the geometry and crystallography of the triple junction considering hypothesis of boundary energy local equilibrium as illustrated by Herring [87]. The Yang results showed very different behaviour for low and high angle grain boundaries and reported that HAGB are much mobile compared to LAGB.

Application of the stress as the driving force for boundary motion has been studied since 1952, for example low angle boundary movement was investigated in Zn crystal [71-72]. In some experimental investigations [86,88] motion of the planar and symmetrical tilt grain boundary was examined by imposing external shear stress normal to the boundary. Winning et. al. [88] studied the movement of both planar low and high angle grain boundary under the influence of applied shear stress. It was reported that, the

variation of activation enthalpy for grain boundary with the extent of misorientation depends on the migration mechanism, such as stress induced migration and curvature dictated migration. Basically the application of shear stress depends on the specimen geometry and the experimental arrangement of the grain boundary set up as shown in Fig. 2.4. The shear stress acting on the plane of the interface exerts a force on the boundary to migrate and the continuous tracking of the grain boundary motion is monitored using the X-ray beam technique (XICTD) which is mentioned earlier. Generally the driving force of the symmetrical tilt boundary migration is measured by the Peach-Koehler equation [89] depending on the applied stress and the misorientation angle and the mobility is extracted from the boundary velocity and driving force relationship.

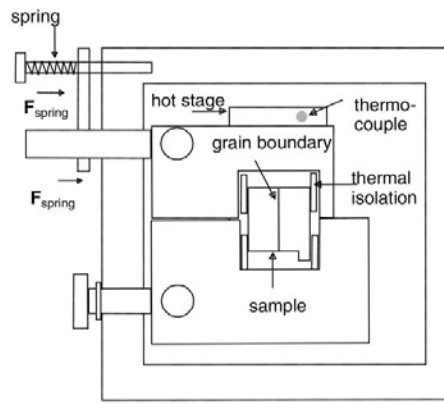


Fig. 2.4: Specimen geometry and its holder for the application of external stress on the grain boundary [86].

Another experimental approach is the measurement of grain boundary mobility during recrystallization which involves a combination of in situ annealing and electron backscattered diffraction (EBSD) in scanning electron microscope (SEM). This technique has been utilized to determine mobility of high angle grain boundary movement during recrystallization [29] and low angle grain boundary migration during recovery [90]. Generally the materials are cold rolled to different percentage of reduction (strain) which in turn introduces different amount of stored energy. The deformed specimen undergoes an in situ annealing experiment in the SEM at different temperatures. The dimension and orientation of the sub grains are extracted from the EBSD measurement. The stored energy in the materials provides a driving pressure on the boundary to migrate which is calculated employing the Read-Shockley relation. For sub-boundary misorientations  $\theta_{sb}$  and sub-grain sizes  $r$ , the expression for driving force is [29]:

$$P = \frac{2\gamma_{gb} \frac{\theta_{sb}}{\theta_{gb}} \left(1 - \ln \frac{\theta_{sb}}{\theta_{gb}}\right)}{r} \quad (2.1)$$

where  $\theta_{gb}$  is the misorientation of the high angle grain boundary which is usually taken as  $15^\circ$  and  $\gamma_{gb}$  is the boundary energy of HAGB which is commonly considered as  $0.324 \text{ J/m}^2$  [91] for aluminum crystals. The sub-boundary energy  $\gamma_{sb}$  is measured from the average sub-grain misorientation using the Read-Shockley equation and then the mobility of sub grain boundary (LAGB) is estimated from its growth and is given by:

$$M_{sb} = \frac{(r^2 - r_0^2)}{k t \gamma_{sb}} \quad (2.2)$$

where  $k$  is a geometrical constant and its value is considered to be  $1.34$ .

## 2.2 Computational techniques for determining grain boundary mobility

The experimental measurement of grain boundary mobility in any pure materials is difficult given the fact that even a material with high purity might contain some impurity elements and the small concentration of the impurities can, in turn, affect the actual boundary migration. But the complete exclusion of such elements is one of the main advantages of the computational approach for determining the grain boundary mobility. Moreover, the simulation technique also provides accurate control on the crystal orientation, temperature, pressure, energy etc. Over the last few years, the atomic scale simulation approach, such as Molecular Dynamics (MD), has emerged as an effective method for computing the grain boundary mobility. To lead to a better prediction of the boundary kinetics, to date, several approaches have been utilized to compute grain boundary mobility from MD simulations.

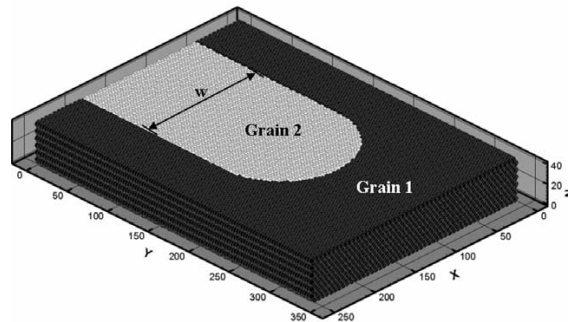


Fig 2.5: The initial bicrystal geometry of the simulation cell with the half loop [77].

One such MD technique determine the reduced mobility of the steady state curvature driven grain boundary migration. Reduced mobility is defined as the product of boundary mobility and boundary stiffness:  $M^* = M(\gamma_{gb} + \gamma_{gb}'' )$ , where  $\gamma_{gb}$  is the grain

boundary free energy,  $\gamma_{gb}''$  is the double derivative of  $\gamma_{gb}$  with respect to orientation and  $(\gamma_{gb} + \gamma_{gb}'')$  refers to the grain boundary stiffness. In this method, a half-loop bicrystal simulation geometry is set up with a U-shaped grain boundary inside of it. The bicrystal geometry of the simulation cell is shown in Fig. 2.5. The velocity and the mobility were determined from the motion of the curved boundary of the U-shape grain. The boundary migration, driven by the curvature of the grain, causes a decrease in the grain boundary energy [92] and that acts as a driving force and the rate of boundary motion is given by  $v = M(\gamma_{gb} + \gamma_{gb}'')\kappa$ , where  $\kappa$  is the boundary curvature. This approach was applied for both two-dimensional [78,93] and three-dimensional [77] systems. Computation of the reduced mobility,  $M^*$ , not the bare mobility,  $M$ , from the curved boundary is one of the main disadvantages of this technique.

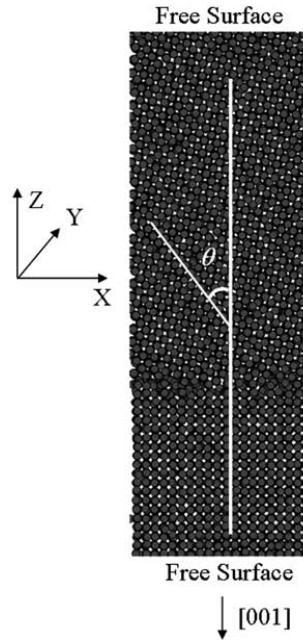


Fig 2.6: The asymmetric planar grain boundary in a bicrystal geometry with free surface normal to the interface [75].

Another MD approach has been developed [74-75] that can be employed to extract the grain boundary mobility itself, the bare mobility, from the planar interface of bicrystal geometry as shown in Fig 2.6. The motion of the boundary is induced by the application of the biaxial strain (tensile or compressive) in two orthogonal directions in the plane of grain boundary. The applied strain causes variation in the elastic energy density stored in one crystal relative to that of other one due to the elastic anisotropy. The difference in the elastic energy provides a driving force for the grain boundary to migrate. There is a limitation for this approach: this technique is only applicable to those crystallographic boundaries which provide elastic anisotropy. In order to utilize this MD approach, the neighbouring crystals must be set up with an asymmetric boundary to make

dissimilarity between grains in terms of stored energy. In this technique the importance of the simulation geometry and its variation in the bicrystal was first given emphasis to the determination of boundary mobility.

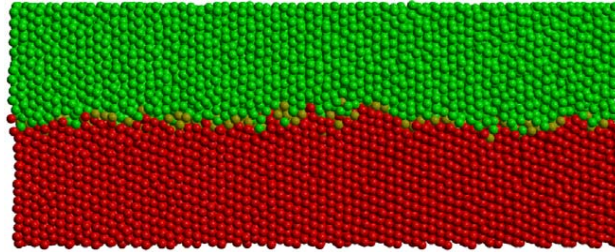


Fig. 2.7: Snapshot of the grain boundary fluctuation showing the height of interface [84]

Later on, Foiles and Hoyt had demonstrated a new MD technique [84] for computing grain boundary mobility and this work measured the boundary stiffness for the first time. The kinetics of the curvature controlled boundary motion is measured by the mobility of the grain growth and the grain boundary stiffness. It was reported that the stiffness is not constant for any given planar boundary, rather it possesses strong dependence on the direction of misorientation within the plane of the boundary. The grain boundary stiffness is defined as the sum of grain boundary free energy and the second derivative of that free energy with respect to boundary orientation,  $(\gamma_{gb} + \gamma''_{gb})$ . Here the second term is very important as it holds the orientational dependence of the boundary distortion. Basically the stiffness was determined employing an analysis of the equilibrium fluctuations of grain boundary in a bicrystal slab during MD simulations. And the mobility was extracted from the dynamics of the interfacial fluctuation spectrum where the time dependent relaxation behaviour of fluctuation is analyzed. Fig. 2.7 shows a snapshot of the interface at high temperature, which illustrates that there is considerable fluctuation in the height of interface. This approach is good for continuum model such as high angle grain boundary case while this is not a suitable approach for low angle grain boundary migration because the dislocations are discrete in the case of low angle grain boundary (LAGB).

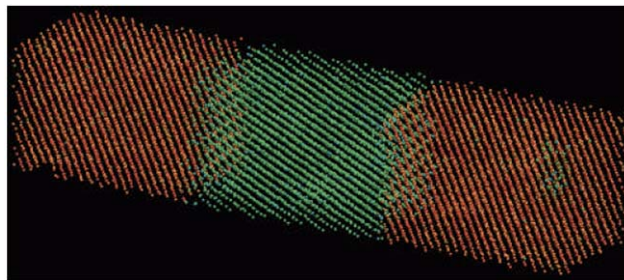


Fig. 2.8: Bicrystal geometry of the simulation cell used for artificial driving force is method [79].

Another MD technique has been developed by Janssens et al. [79] where the bare grain boundary mobility is computed through the application of an artificial driving force on the boundaries. This method provides a measure of the mobility for any random planar boundary in the whole span of crystallographic misorientation angle. In this approach, an artificial potential energy that depends on the crystal orientation of the nearest neighbours is introduced to each atom in the system. The synthetic driving force is added to one crystal of a bicrystal slab which increases the free energy of that crystal relative to the other and hence provides driving force acting on the grain boundary. This driving pressure causes the boundary to migrate in such a way that the shrinkage of the crystal of added energy, or equivalently growth of the other crystal, will result in a decrease in the free energy. In Fig 2.8, a bicrystal is shown, where high potential energy (PE) is added to the green atoms and zero PE is added red atoms. The movement of the grain boundary leads to the determination of the velocity and mobility of the boundary motion.

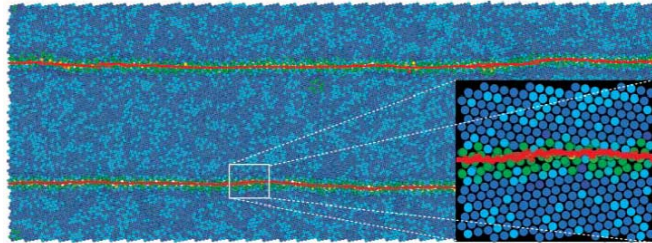


Fig. 2.9: Snapshot of the simulation showing the 1-D random walk of grain boundary around its average position [82].

In a recent study, another computational approach has been formulated to extract the interface mobility from atomic scale simulation through an analysis of the equilibrium fluctuation of grain boundary position [82-83]. In this alternative procedure, the absolute value of the interface mobility is extracted without the application of any driving force, i.e. in the limit of zero driving force. During MD simulation, the grain boundary is only allowed to fluctuate in the direction normal to interface. The boundary mobility is calculated from the random walk of the average interface position. In Fig 2.9, a fluctuated grain boundary is shown that undergoes random walk. In the all previous methodologies, the grain boundary mobility has been studied through the utilization of the driving force in different forms[74-75,77-79,93], such as interfacial curvature, strain induced bulk driving force, external applied potential energy, stored energy of deformation etc. The drawbacks of the applied driving force methods are considered as the high force that is required to cause the motion of boundary. In this regime of forces, the interface might deviate from the linear relationship between interface velocity and applied force may no longer exist and as a result the kinetics of the boundary motion might change to some extent. In that respect, the random walk technique possesses advantages due to the absence of the driving force.

### 2.3 Significant results of previous studies

A number of computational and experimental investigations have been conducted to determine the value of grain boundary mobility to have a better fundamental understanding utilizing the above discussed methods. Most of the studies were carried out on high angle grain boundaries and very few are done on low angle boundaries. Summarizing all the computational and experimental observations, some general findings can be stated regarding boundary migration rate and variation of the mobility with temperature. It was reported in most of the investigations that the velocity of the grain boundary motion is directly proportional to the driving force applied to the boundary to cause its movement. Mobility is the proportionality constant between driving pressure and boundary velocity such that  $v = MP$  where  $M$  and  $P$  denotes mobility and driving force respectively and  $v$  is the boundary migration rate. In an experimental study of HAGB mobility in Al-0.05wt%Si alloy by Huang and Humphreys [29], it was noticed that there might be a threshold driving pressure which is required to cause the migration of the grain boundary at low driving pressure and low temperature. This is shown in Fig. 2.10, where the limiting driving pressure is 0.02 MPa at  $\sim 300^\circ\text{C}$ . Their experiment was based on in situ annealing and electron backscattered diffraction in the SEM has been utilized to measure the boundary mobility during recrystallization. In almost all experimental studies, it was found that the variation of the mobility with temperature follows an Arrhenius type function which is also true for all the simulation investigations as well. And the activation energy for boundary migration is generally calculated from the slope of the Arrhenius plot.

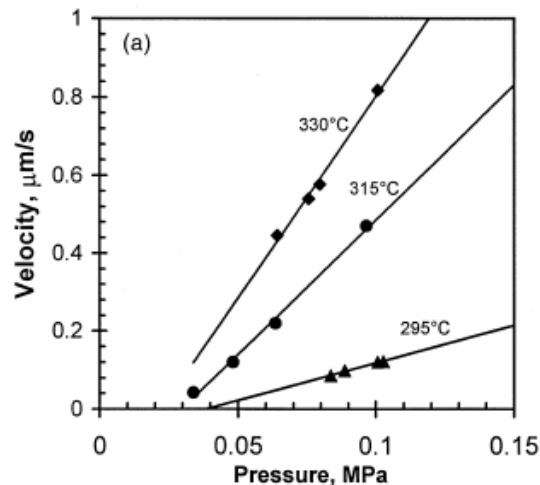


Fig. 2.10: Grain boundary migration rate as function of driving pressure at different low annealing temperatures [29].

Winning and Molodov [86,88,92,94-95] have conducted some experiments to observe the stress induced grain boundary migration and summarized their findings of boundary mobility in pure Al for both low and high angle planar symmetrical grain

boundary. As mentioned in section 1.5, In Winning's study [12,88], it was noted that mobility is nearly constant for both high and low angle boundary at a specific temperature, but there is a transition misorientation angle between these two extreme. The authors reported a roughly two orders of magnitude increase in the mobility as the misorientation angle increased from below  $\sim 10^\circ$  to above  $\sim 15^\circ$ . Mobility is higher for high angle boundary compared to that of low angle at low temperature and, in contrast, the trend is reversed at high temperature. These phenomena are shown in Fig. 1.5. The dramatic jump in mobility was explained in terms of the interaction of the boundaries with network dislocations. For LAGBs, which can be viewed as a periodic array of distinct edge dislocations, the motion can be pinned by other network dislocations. For HAGBs, on the other hand, network dislocations are absorbed by the migrating boundary. This explanation is consistent with an earlier proposal by Viswanathan and Bauer [66] who observed an activation energy for the LAGB in Cu that is consistent with dislocation climb and a much lower activation energy for the case of HAGBs.

The dependence of the mobility on the misorientation angle as a function temperature is investigated in Ref. [31,78] in detail. Molodov et. al. [31] have shown that, in aluminum bycrystal, at low temperature ( $T < 430^\circ\text{C}$ ), the boundary mobility is highest at  $38.2^\circ$  misorientation angle while above  $430^\circ\text{C}$  the mobility is found to be highest at  $40.5^\circ$ . The highest magnitude of mobility is attributed to high pre-exponential mobility factor, even though the activation energy is high at that condition. The linear dependence of these two terms is considered as compensation effect and the corresponding critical temperature is referred as compensation temperature. Such variation of mobility or activation enthalpy with misorientation angle is irrespective of the impurity content.

Molodov et al. [28] have also investigated the grain boundary motion to observe the effect of impurity of material. As illustrated in section 1.4, Molodov's study has shown a strong dependence of impurity level on the grain boundary migration in pure aluminum. They reported reduction in boundary mobility by two orders of magnitude due to 0.4 to  $7.7 \times 10^{-4}$  at% impurity content at two different temperatures. This effect is illustrated in Fig. 1.4. The presence of very small amount of impurity decreases the boundary mobility, as the diffusion and adsorption of these impurities increases the activation enthalpy of the boundary migration.

It was mentioned earlier that, in addition to high angle grain boundary, some works focused on the motion of low angle boundary. In one of such experimental studies, Hunag and Humphreys [90] have characterized the subgrain motion extensively by describing the growth kinetics in annealing treatment and measuring the low angle boundary mobility in detail in their study of Al-0.05% Si. They observed that the subgrain growth is different from the normal grain growth in a way that the regions of subgrain show a non-uniform growth nature. Some of the subgrains are found to grow continuously at a slower rate while some others grow discontinuously at much faster rate. The rapidly growing areas produce comparatively high misorientation angle with the surroundings. An example is shown in Fig 2.11. To emphasize their prediction of

different mechanism of subgrain growth than that of normal grain, they have reported the subgrains did not grow proportionally. The standard deviation of the subgrain grain size distribution was not constant, rather it was found to increase significantly during the growth. The abnormal growth subgrains are claimed to be consistent with some other earlier experimental and computational works [20,96-98].

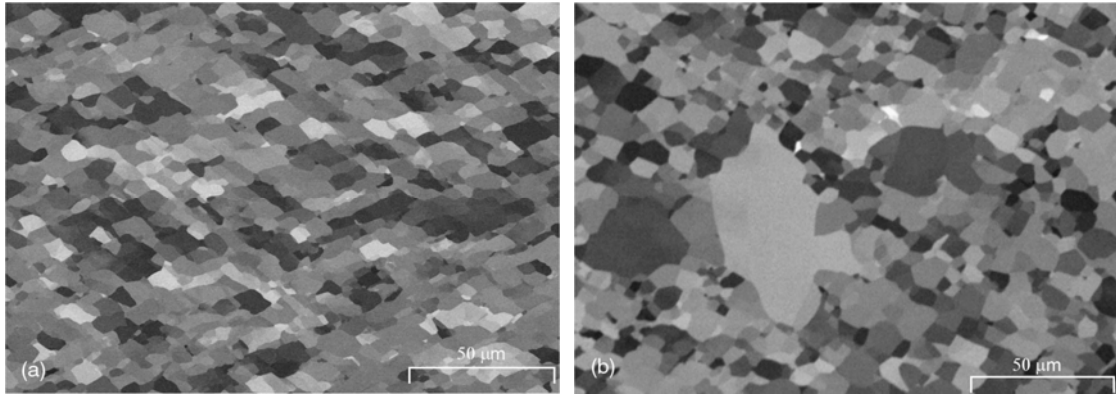


Fig 2.11: SEM micrograph of material deformed 70% at 350°C with (a) no annealing, (b) annealing for 3 hour at 300°C [90].

In Huang's study, the mean misorientation between the subgrains was shown to reduce with the annealing time during the continuous growth but the misorientation gradient was not of long range. The decrease in the misorientation is related to the increase in subgrain size through an empirical equation,  $\frac{\bar{\theta}}{\bar{\theta}_0} = \left(\frac{\bar{r}}{\bar{r}_0}\right)^{-0.13}$  where  $\bar{\theta}_0$  and  $\bar{r}_0$  are the initial mean misorientation and initial mean subgrain size. The reduction in misorientation during subgrain growth is shown in Fig. 2.12 for different temperature. The small decrease in mean misorientation during annealing in Huang's experiment is found to be consistent with some other analysis [20,99] and some simulation work [97] of subgrain growth. In contrast, for the case of discontinuous growth, mean misorientation is found to increase with size up to ~5-15  $\mu\text{m}$  which is followed by

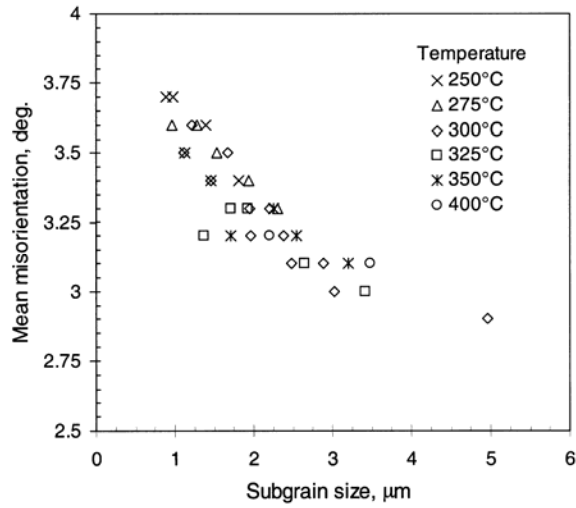


Fig. 2.12: The changes in misorientation angle with the subgrain size as the annealing proceed [90].

remaining nearly constant. The abnormally growing subgrains develop very fast producing a large value of  $\bar{\theta}$  in early stage of annealing and the plateau value of misorientation approaches the mean value.

Generally, during isothermal annealing, the grain growth kinetics is controlled by the equation,  $\bar{D}^n - \bar{D}_0^n = kt$ , where mean grain size  $\bar{D}$  is related to the initial grain size  $\bar{D}_0$  and annealing time  $t$ . For the normal grain growth, the value of  $n$  is usually considered as 2 which indicate a parabolic growth. In contrast, the studies [100-103] on sub-grain growth have shown that a good fit of the experimental data is found to demonstrate the value of the exponent in the range of 3-8. In their study, Huang et al. [90], also investigated the dependence of low angle grain boundary mobility with boundary misorientation in regime  $2.5^\circ < \theta < 5.5^\circ$ . They reported an empirical power law relation between LAGB mobility and misorientation that is defined as  $M_{sb} = A\theta^C$ , where  $A = 3 \times 10^{-6} m^4 / Js$  and  $C = 5.18$ . It was also mentioned that this relation will not be a good fit outside the examined range of misorientation. The variation of low angle boundary mobility with misorientation is shown in Fig. 2.13.

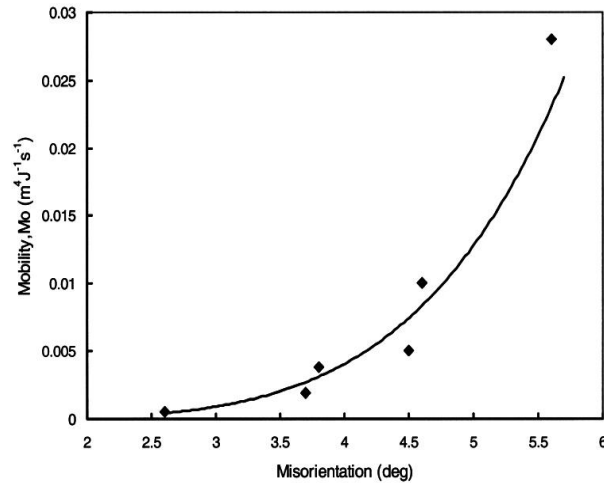


Fig. 2.13: Variation of low angle boundary mobility with misorientation in the regime  $2.5^\circ < \theta < 5.5^\circ$  [90].

According to the grain growth theory of Hillert [104], the rate of subgrain growth is considered to be proportional to the driving force, i.e.  $v_{sb} = M_{sb}P$ , where  $v_{sb}$  is the growth velocity which is measured from the rate of change in subgrain size and  $M_{sb}$  and  $P$  refers to the mobility and the driving pressure respectively. The activation energy of the low angle grain boundary is obtained 134 KJ/mol in Huang's study of Al-0.05%Si. In most cases, the activation energy of grain boundary motion determined from the experimental measurements was observed to be considerably different than that of computational techniques [75,78,105]. In general, the reason is attributed to the presence of the impurities in the pure system during experimental investigation, compared to the bare mobility in computational techniques.

Besides experimental observation, there exist a number of significant results in the computational approaches of grain boundary mobility determination. As described for experimental results, most of the computational methods provide linear relationship between boundary velocities and applied driving force. The variation of mobility with temperature follows Arrhenius type function. Some of the major results, obtained from simulation studies will be discussing below.

In a study of grain boundary mobility computation in fcc Ni, Olmsted [106] has described the nature of the grain boundary interface at different temperature region and its effect on the mobility. The authors stated that there is a roughening temperature ( $T_c$ ), below which the grain boundaries are smooth and, above which the boundaries are rough. It was observed that the boundary motion was linear with time for the rough boundaries at higher temperature while it exhibited a stepwise behaviour during migration of the smooth boundaries at lower temperature. This trend is shown in Fig. 2.14. It was reported that the mobility is low below the roughening temperature and increases sharply above it. The concept of  $T_c$  has a considerable effect on the microstructure evolution.

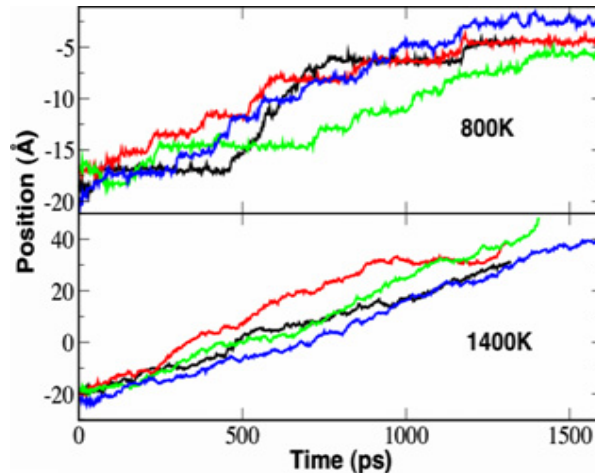


Fig. 2.14: The boundary is rough at 1400K and moves continuously while at 800K boundary is smooth and migrates in step [106].

In a comprehensive MD study, Olmsted et. al. [9] computed mobility of 388 grain boundaries in EAM pure Ni. The authors mainly studied the temperature and misorientation dependence of boundary mobility and its migration mechanism. Olmsted reported that some boundaries, including  $\langle 111 \rangle$  twist, are immobile in the mobility resolution limit of MD simulation. The resolution limit is shown as solid line in Fig. 2.15, below which, the boundary mobilities are considered zero. It was shown that the migration mechanism of most of the highest mobility boundaries, except  $\Sigma 3$  incoherent twins, is controlled by the mechanism of shear-coupled motion as described by Cahn and Mishin [107-108]. The authors demonstrated the temperature effect on mobility in terms of non-activated boundary motion and boundary transition temperature. The thermally activated boundary motion is characterized by increase in mobility with temperature following an Arrhenius function. Olmsted reported that 117 boundaries showed non-activated boundary motion, where mobility decreases with temperature in a certain temperature range. The authors also extensively observed the existence of roughening temperature in their study.

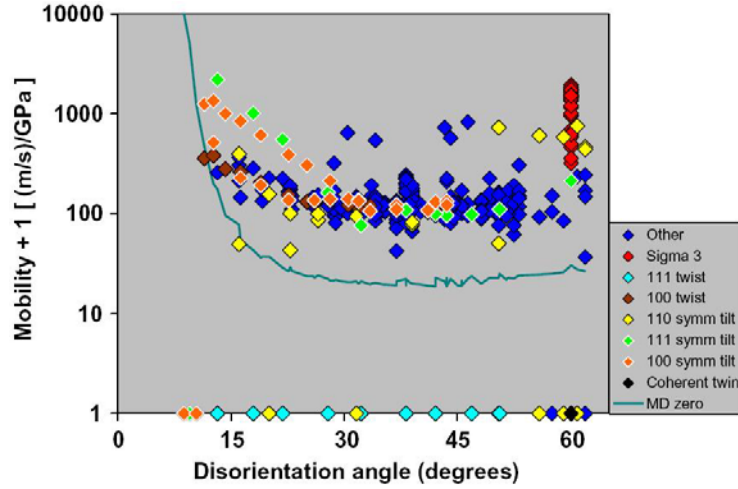


Fig. 2.15: Mobility as a function of misorientation in EAM Ni at 1400K for 388 simulated grain boundaries [9].

The importance of boundary roughening is illustrated in a computational study by Holm et. al. [109], where roughening is shown as stagnation mechanism of grain growth. The polycrystal materials usually contain smooth and rough boundaries that correspond to slow and fast boundary motion respectively. The authors reported that the grain growth can be stopped due to the presence of small fraction of smooth boundary even in very high purity material. It was shown that, in EAM Ni, at low temperature 90% boundaries are smooth, however, there exist at least 10% smooth (slow) boundary even at  $0.9T_m$ , where  $T_m$  is the melting point. This is illustrated in Fig. 2.16.

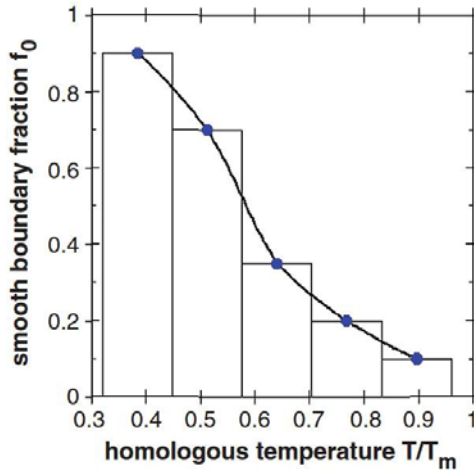


Fig. 2.16: Distribution of smooth boundary as function of temperature measured in EAM Ni [109].

The authors investigated the effect roughening on the grain growth by incorporating boundary mobility and roughening statistics from Fig. 2.16. The grain

growth kinetics in Ni polycrystal as a function of smooth boundary fraction is shown in Fig. 2.17 that was computed from a mesoscale simulation. The time is given in monte carlo step (MCS). The authors reported that the stagnation of the grain growth is observed for all fractions of smooth (slow) boundary examined, even at  $f_o = 0.1$ .

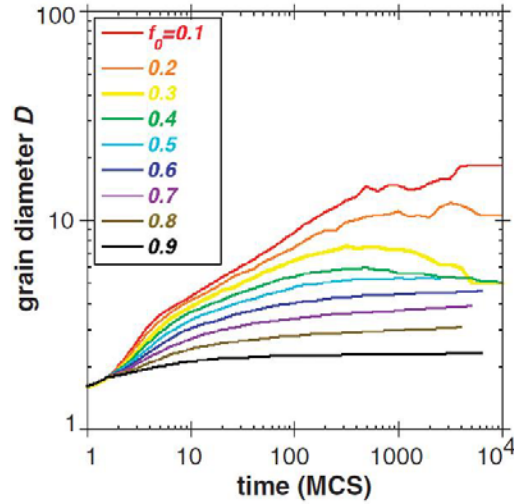


Fig. 2.17: Grain growth in polycrystal Ni containing different fraction smooth boundary computed from a mesoscale simulation [109].

As mentioned earlier, in a study of boundary motion mechanism, Cahn, Mishin and Suzuki [107] demonstrated that some grain boundaries are coupled in the sense that shear deformation parallel to the boundary plane induces motion normal to the boundary. Karma et al. [10] then showed that for coupled boundaries the capillary fluctuation spectrum has a different wavenumber dependence than uncoupled boundaries. Of particular relevance to the present work, the Karma et al. study compared three different MD techniques, fluctuations, random walk, stress driven motion and observed GB mobility dependence as a function of misorientation in the range  $5^\circ \leq \theta \leq 37.5^\circ$ . The authors concluded that mobility increases with decreasing misorientation at 1200K in pure Cu system, as shown in Fig. 2.18, which is in agreement with theoretical prediction [11].

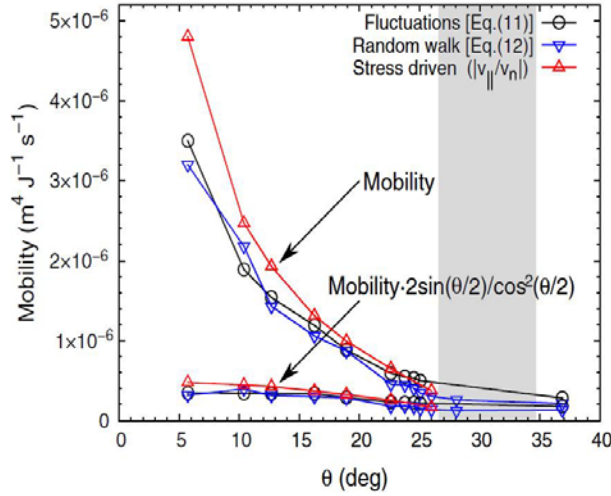


Fig. 2.18: Grain boundary mobility vs. misorientation angle determined using different MD techniques [10].

In a recent atomistic investigation of grain boundary motion, Deng and Schuh [110] studied the boundary motion mechanism in terms of velocity–driving force behaviour depending on temperature. The authors reported that, in addition to have linear function of velocity with applied force, there are two distinct regimes to describe this behaviour. At low driving force the grain boundary migration is controlled by diffusional motion and, in contrast, by ballistic motion at high applied force. This is illustrated in Fig. 2.19. The transition regime is wide at low temperature, but it is sensitive at high temperature motion. The authors claimed that the different migration mechanism can attributed to the discrepancy of boundary activation energies determined from computational and experimental techniques.

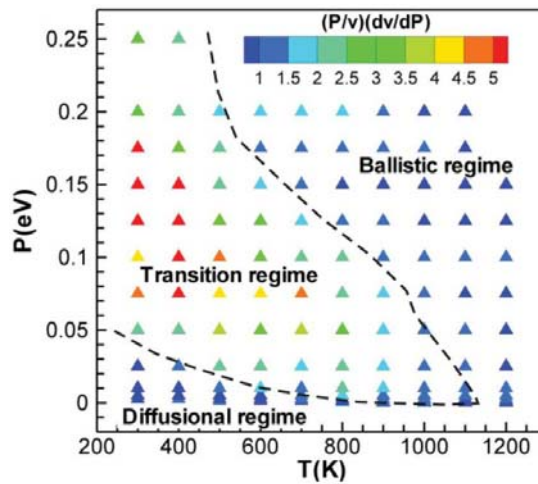


Fig. 2.19: Dependence of different region of grain boundary migration mechanism on the applied driving force and temperature for symmetric sigma-5 boundary [110].

## 2.4 Embedded atom method (EAM) interatomic potential

The atomic interactions of the model pure Al system, studied in this thesis, are described by an embedded atom method (EAM) type interatomic potential developed by Mendeleev et al. [111]. EAM is a semi-empirical potential and incorporates many body interactions to compute the total energy of the system. This approach was first introduced by Daw and Baskes [112] to calculate ground state properties of the metallic systems. In this method, the energy is determined by embedding an atom into the local electron density of its neighbour. EAM method can be utilized for semi quantitative and quantitative description of several phenomena, such as impurities, fracture, melting, crystal growth, alloying and so on in the metallic systems [113]. The energy of atom  $i$  in the EAM method is given by the following equation:

$$E_i = F_\alpha \left( \sum_{i \neq j} \rho_\beta(r_{ij}) \right) + \frac{1}{2} \sum_{i \neq j} \phi_{\alpha\beta}(r_{ij}) \quad (2.3)$$

where  $F$  is the embedding energy function,  $\rho$  is the partial electron density contribution,  $r_{ij}$  denotes the distance between atom  $i$  and  $j$ ,  $\phi$  is the pair potential,  $\alpha$  and  $\beta$  are the element types of atom  $i$  and  $j$ .

## 2.5 Simulation Procedure

The low angle grain boundary simulation systems were generated at different temperatures in accordance with the corresponding equilibrium lattice parameter. A symmetric [112] tilt boundary was used where the misorientation angle between two crystals is  $7.785^\circ$ . The bicrystal slab was set up such that crystal-1 has the orientation  $x \Rightarrow [17 \ 19 \ \bar{1}]$ , meaning that the  $x$  direction corresponds to the crystallographic direction  $[17 \ 19 \ \bar{1}]$ ,  $y \Rightarrow [\bar{1} \ 1 \ 2]$ ,  $z \Rightarrow [39 \ \bar{33} \ 36]$  and crystal-2 has  $x \Rightarrow [19 \ 17 \ 1]$ ,  $y \Rightarrow [\bar{1} \ 1 \ 2]$ ,  $z \Rightarrow [33 \ \bar{39} \ 36]$  and the  $x$ -axis was the direction normal to the grain boundary. The simulation cell contains a total of 82895 atoms and was  $40\text{\AA}$  by  $127\text{\AA}$  in the plane of boundary ( $yz$  plane). The dislocation spacing was 5 atomic planes at the grain boundary. The simulation geometry is kept periodic in the plane of the grain boundary while there are two free surfaces in the direction normal to the boundary. According to Cahn and Mishin [104], and verified in our simulations, the [112] tilt boundaries studied undergo coupled shear motion. The free surfaces employed in our simulations accommodate the coupled motion and avoid the build up of stress as the boundary migrates. A simulation snapshot of the bicrystal slab, at 300K, with the low angle grain boundary (LAGB) is shown in Fig. 2.20.

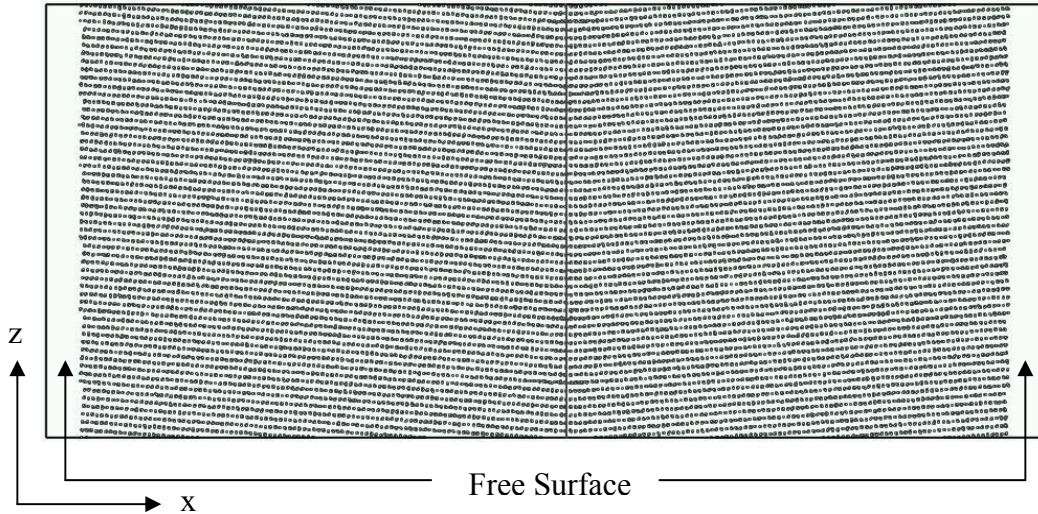


Fig. 2.20: Bi-crystal simulation geometry, at 300K, containing a  $[112]$  symmetric tilt  $7.785^\circ$  boundary with free surfaces at both ends. The position of the interface is shown with a solid line.

The equilibration MD runs were performed in NVT (constant number of atoms, volume and temperature) ensemble for a few ns. The equilibration was monitored by tracking the steady state variation in pressure and energy of the system. After a preliminary equilibration period, the simulation system was utilized to generate statistics in the random walk (RW) and the artificial driving force (ADF) method to compute low angle boundary mobility. All the performed MD simulations of this study employed the LAMMPS (Large-scale Atomic/Molecular Massively Parallel Simulator) code [114-115] and a time step of 1fs was used throughout. The LAGB is generated with perfect crystal dislocations which are considered to be  $[110]$  lattice dislocations and the Burgers vector is located in a  $(1\ 1\ -1)$  glide plane. A schematic view of the dislocation structure of such LAGB symmetrical tilt boundary is shown in Fig. 2.21. Three more bi-crystal systems with  $11.655^\circ$ ,  $17.408^\circ$  and  $23.07^\circ$  misorientation were generated at different temperature to investigate the interface mobility and the variation with the change in misorientation and temperature. The systems were set up following the same procedure as discussed for the  $7.785^\circ$  boundary.

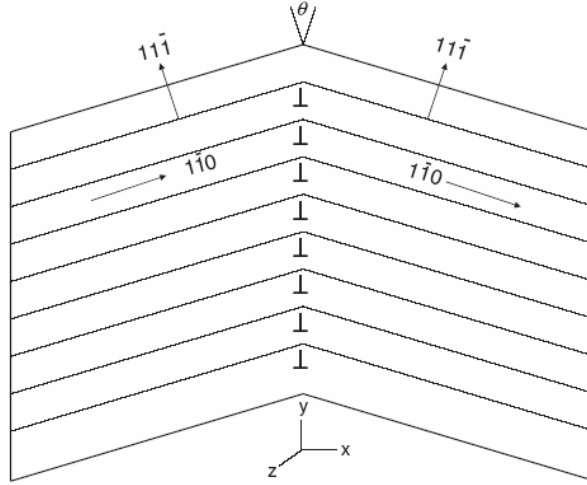


Fig. 2.21: Schematic diagram of the dislocation arrangement in low angle symmetrical grain boundary [12].

## 2.6 Application and results of random walk (RW) method

In the RW technique, grain boundary mobility is extracted from the random walk motion of the average interface position. This method considers the temperature dependent fluctuation analysis of the grain boundary in a bi-crystal slab. In the equilibrium fluctuation spectrum, the interface migration rate,  $v$ , is directly linked to the capillary driving force,  $\kappa_\gamma = (\gamma_{gb} + \gamma_{gb}'' ) \kappa$ , and Langevin force,  $\eta$  that represents intrinsic thermal noise uncorrelated in space and time, as  $v = M(\gamma_{gb} + \gamma_{gb}'' ) \kappa + M\eta$ , where  $M$  represents grain boundary mobility. The integration of this expression over space and time, along with the Langevin description of noise, yield the mean square displacement of the average interface position as [82]:

$$\langle \bar{h}^2 \rangle = Dt = \frac{2Mk_B T}{A} t \quad (2.4)$$

where  $D$  is the diffusion coefficient and  $A$  is the area of the interface plane. Thus, the interface location shows a classical random walk where  $\langle \bar{h}^2 \rangle$  increases linearly with time and the slope of  $\langle \bar{h}^2 \rangle$  vs.  $t$  plot provides the value of the interface mobility.

The average position,  $\bar{h}(t)$ , of the grain boundary was determined utilizing the centro-symmetry (CS) parameter approach [116]. The centro-symmetry is a useful parameter that can be used to define the defects such as dislocations and grain boundaries in the simulation geometry. The calculation of CS parameter is described as the following formula:

$$CS = \sum_{i=1}^{N/2} \left| \vec{R}_i + \vec{R}_{i+N/2} \right|^2 \quad (2.5)$$

where,  $N$  is number of nearest neighbours of each atom, for example 12 and 8 for fcc and bcc structure respectively.  $\vec{R}_i$  and  $\vec{R}_{i+N/2}$  refer to the vector distance of a pair of nearest neighbours from the center atom. The CS parameter will be zero for an atom that is surrounded by the atoms on a perfect lattice. The surface atoms and the presence of any defects break symmetry and possess a large value of the CS parameter. Therefore, the position of the grain boundary corresponds to the jump in the centro-symmetry number when the CS parameters for each atom are plotted as a function of x-position of the simulation cell. A typical plot of the centro-symmetry parameters with x-position of the bicrystal geometry with  $7.785^\circ$  boundary is shown in Fig. 2.22 and this snapshot is taken at 300K.

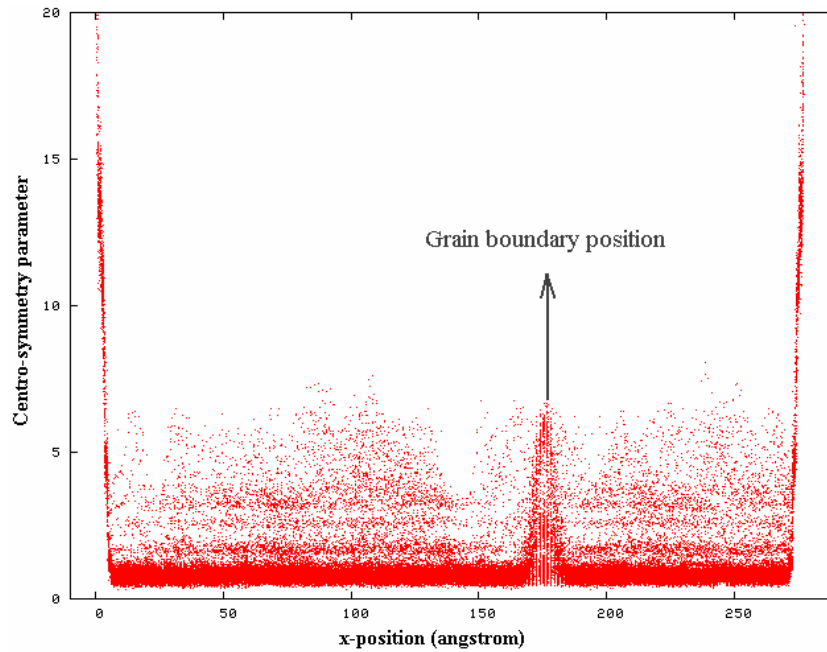


Fig. 2.22: A typical plot of centro-symmetry parameter as a function of x-position.

In this approach, the equilibrium MD simulations were performed in a pure Al system ranging from 300K to 800K. The bicrystal systems were set up at each temperature following the same procedure described for 300K. An NVT ensemble was applied to the system during the simulation of equilibration and the fluctuations of the grain boundary was considered in the direction normal to the boundary interface. The statistics of the boundary fluctuations were collected using the same ensemble. At each temperature every system was run for around 3~5ns and the position of grain boundary is tracked at every 50ps time interval. As mentioned earlier, the position of the grain

boundary was determined from the centro symmetry parameter measurement. The mean square displacement,  $\langle \bar{h}^2 \rangle$ , of the interface position is then calculated from 1-D random walk analysis of the grain boundary. A representative 1-D random walk of low angle grain boundary at 500K is shown in Fig. 2.23 for the case of a [112] LAGB with a small misorientation of  $7.785^\circ$ . In this figure, the grain boundary position is observed to fluctuate randomly within the range of approximately 20-22 Å around its average position.

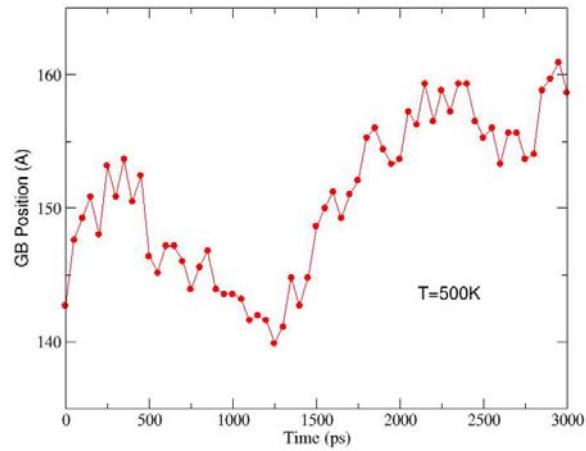


Fig. 2.23: 1-D random fluctuation of grain boundary position with time at 500K for the [112] tilt boundary with a misorientation of  $7.785^\circ$ .

A typical plot of  $\langle \bar{h}^2 \rangle$  vs. time at 500K is shown in Fig. 2.24. As is standard practice in MD analyses of correlation functions, the time origin is arbitrary and the error bars (standard error) in the figure represent 40-60 independent times from a lengthy simulation. Again, the results refer to the  $7.785^\circ$  misorientation LAGB. The linear relation of the function  $\langle \bar{h}^2 \rangle$  vs. time has supported the prediction of the random walk approach and the mobility of the boundary migration is computed from the slope of this plot. From this plot, the mobility of the LAGB is found to be  $3.0 (\pm 0.4) \times 10^{-6}$  m/s/Pa at 500K. Following the same procedure, the magnitudes of mobility are extracted at all temperatures in the range of 300K – 800K. The LAGB mobility is found to increase with the increase in temperature in the investigated range.

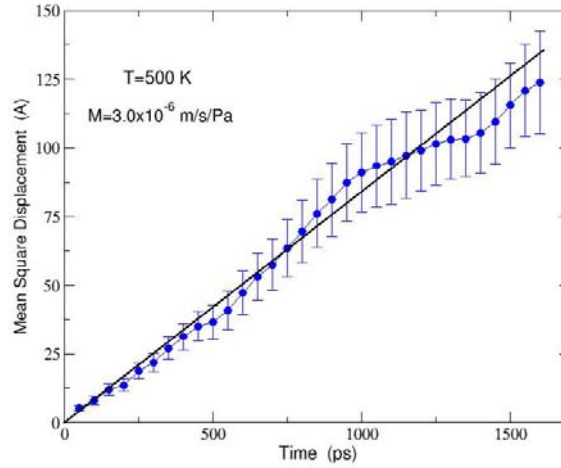


Fig. 2.24: Time evolution of mean square displacement of grain boundary position at 500K for the 7.785° misoriented LAGB.

## 2.7 Application and results of artificial driving force (ADF) method

The artificial driving force (ADF) technique involves application of an orientation dependent synthetic potential energy to the MD simulation cell. The driving pressure is applied to one of the grains in a bicrystal geometry. Therefore, this approach requires proper identification of the atoms in differently orientated crystal. The atoms in crystal-1 and crystal-2 are differentiated using an order parameter, OP ( $\xi$ ), measurement [79]. OP is calculated from the orientation of nearest neighbour atoms in the crystal lattice. The order parameter for atom  $i$  is defined as the following expression [79]:

$$\xi_i = \sum_j |r_j - r_j^I| \quad (2.6)$$

where  $j$  refers to the nearest neighbour atoms which is 12 for the f.c.c material,  $r_j^I$  is the position of nearest ideal lattice site of the crystal with specific orientation  $I$  and  $r_j$  denotes the position of the nearest neighbour after a local deviation from its ideal position. At the ideal condition, the value of  $\xi_i$  is zero. Local deviation of an atom position from the orientation of an ideal lattice for one crystal orientation in the two grain system will cause a clear jump in the OP and hence determine whether any specific atom belongs to crystal-1 or crystal-2. The atoms whose order parameter is lower than a threshold given by  $\xi_{low}$ , are assumed to be in one grain, while the atoms whose order parameter is higher than  $\xi_{high}$ , belong to the other grain. The atoms with order parameter  $\xi_{low} < \xi < \xi_{high}$ , are considered to be in the interface region and are assigned an energy as

described below. A schematic plot of the order parameter profile as a function of distance normal to the grain boundary is illustrated in Fig. 2.25.

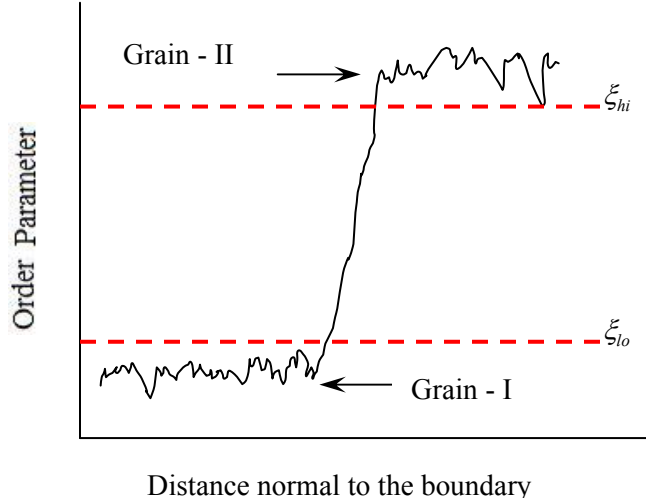


Fig. 2.25: Schematic illustration of the order parameter (OP) profile as a function of the distance normal to the boundary. For OP higher than  $\xi_{hi}$ , potential energy is assigned and for OP less than  $\xi_{lo}$ , zero potential energy is added.

The assignment of the artificial potential energy involves the use of order parameter cut off values. In a bi-crystal slab, once the atom positions in two differently oriented crystals is defined, the orientation dependent potential energy will be applied to one of the crystals to create a driving force on the low angle grain boundary, which will cause the boundary migration. The function for this artificial potential energy per atom ( $i$ ),  $u_\xi$ , is defined as [79]:

$$u_\xi = \begin{cases} 0 & \xi_{low} < \xi_i \\ \frac{V}{2}(1 - \cos 2\omega_i) & \xi_{low} < \xi_i < \xi_{high} \\ V & \xi_{high} < \xi_i \end{cases} \quad (2.7)$$

where  $\omega_i$  is the normalized order parameter, which is defined as  $\omega_i = \frac{\pi}{2} \frac{\xi_i - \xi_{low}}{\xi_{high} - \xi_{low}}$  and

$V$  corresponds to the chosen driving potential. A typical plot of the applied potential energy vs. order parameter  $x = (\xi - \xi_{lo}) / (\xi_{hi} - \xi_{lo})$  is shown in Fig. 2.26. The energy plot illustrates that a certain amount of potential energy, according to Eq. 2.7, has been added to crystal-2 (OP = 1) with respect to crystal-1 (OP = 0), where zero PE is added. The extrapolation function in Fig. 2.26 provides zero slope at both ends (OP = 0 and 1), and there is a smooth transition in the potential curve through the interface. That means, due

to the addition of orientation dependent artificial energy, no force is added to the bulk grain of crystal-1 and crystal-2 and the amount of total force that drives the grain boundary is determined by the magnitude of the slope in the potential energy profile from the region of  $0 < OP < 1$ .

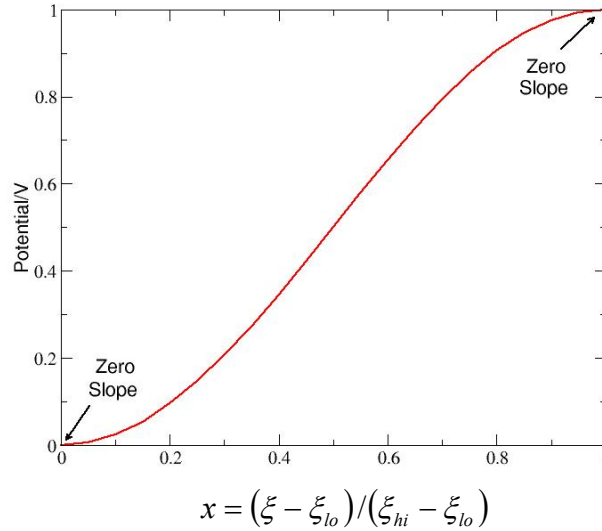


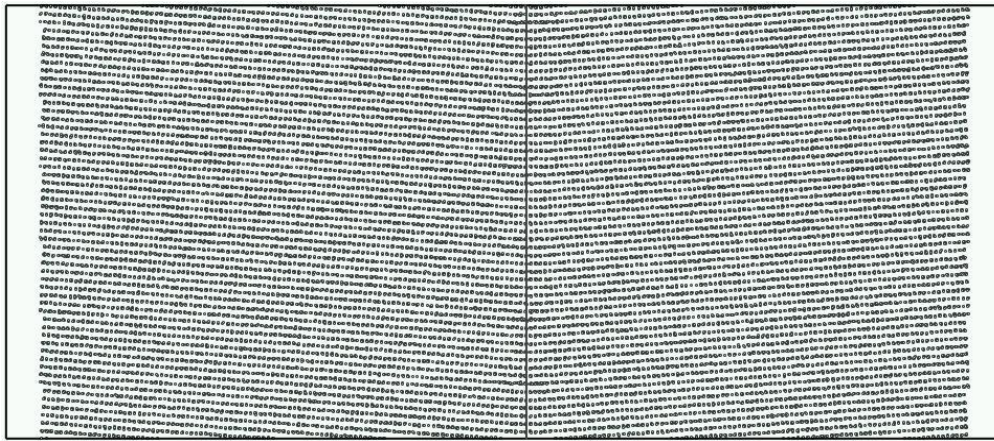
Fig. 2.26: A schematic profile of the applied potential as a function of order parameter.

As mentioned earlier, the ADF technique applies an orientation dependent artificial driving force to the atoms nearest to the planar grain boundary for the boundary migration to occur. The grain orientations of the two crystals are specified by the nearest neighbour atoms position in the Al fcc crystal lattice at their proper orientation. The nearest atom positions are calculated for the original axis system ( $x = [100]$ ,  $y = [010]$ ,  $z = [001]$ ) which is then transformed to new axis ( $x = [110]$ ,  $y = [\bar{1} 1 2]$ ,  $z = [1 \bar{1} 1]$ ). The new axis is then once again transformed to the proper orientation, such as for crystal-1 of  $7.785^\circ$  boundary at 300K:  $x = [17 19 \bar{1}]$ ,  $y = [\bar{1} 1 2]$  and  $z = [39 \bar{3} 36]$ . All the transformations of the axis was done using a rotation matrix (R) and the formula is  $[New] = [R] \times [Old]$ . The properties of the rotation matrix (squared summation of all elements in the column is equal to one and that of row elements is one as well) was observed in the derived matrix. The rotation matrix and nearest neighbour atoms for crystal 1 are shown in the Table 2.1.  $R_1$  is the rotation matrix for the first transformation and  $R_2$  is the rotation matrix for the second transformation of axis. The Al system has a coordination number of 12 being fcc lattice, but only 6 are mentioned due to the symmetry.

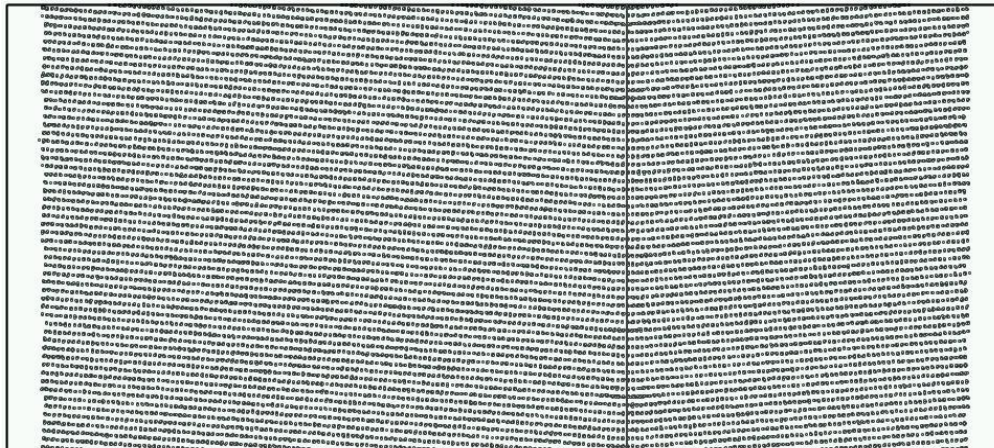
Table 2.1: The rotation matrix of transformation and the nearest neighbour atoms at different axis for crystal-1 of 7.785° boundary at 300K. The atom positions are in terms of lattice parameter.

[100], [010], [001]	[110], [ $\bar{1}$ 12], [ $1\bar{1}$ 1])	[1719 $\bar{1}$ ], [ $\bar{1}$ 12], [393 $\bar{3}$ 36]
$R_1 = \begin{bmatrix} \frac{1}{\sqrt{2}} & \frac{1}{\sqrt{2}} & 0 \\ -\frac{1}{\sqrt{6}} & \frac{1}{\sqrt{6}} & \frac{2}{\sqrt{6}} \\ \frac{1}{\sqrt{3}} & -\frac{1}{\sqrt{3}} & \frac{1}{\sqrt{3}} \end{bmatrix}$	$R_2 = \begin{bmatrix} \frac{18\sqrt{2}}{\sqrt{651}} & 0 & \frac{-1}{\sqrt{217}} \\ 0 & 1 & 0 \\ \frac{1}{\sqrt{217}} & 0 & \frac{18\sqrt{2}}{\sqrt{651}} \end{bmatrix}$	
(0.5, 0.5, 0)	(0.707106781, 0, 0)	(0.705475621, 0, 0.048001536)
(-0.5, 0.5, 0)	(0, 0.40824829, -0.577350269)	(0.03919309, 0.40824829, -0.576018432)
(0.5, 0, -0.5)	(0.35355339, -0.612372435, 0)	(0.35273781, -0.612372435, 0.024000768)
(-0.5, 0, -0.5)	(-0.35355339, -0.204124145, -0.577350269)	(-0.31354472, -0.204124145, -0.6000192)
(0, 0.5, -0.5)	(0.35355339, -0.204124145, -0.577350269)	(0.3919309, -0.204124145, -0.552017664)
(0, -0.5, -0.5)	(-0.35355339, -0.612372435, 0)	(-0.35273781, -0.612372435, -0.024000768)

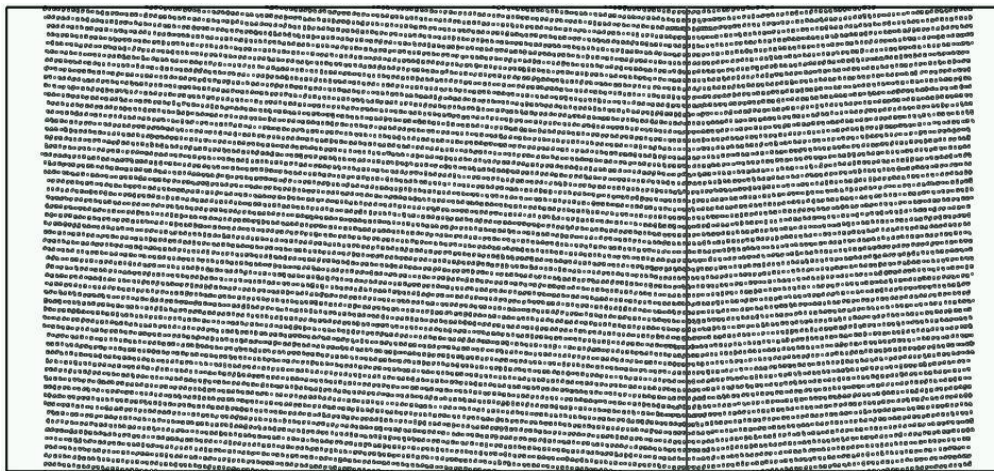
For the migration of low angle grain boundaries, a wide span of artificial potential energy, ranging from 0.0004 to 0.09 eV/atom was applied at 300K. The driving force is introduced in the equilibrated structure that contains free surfaces in the direction normal to the interfaces. An NVT thermostat is used to control the temperature during the course of the simulation. A positive potential energy is added to crystal-2, so the grain boundary will move in such a way that the second crystal will shrink and the first crystal will grow to reduce the potential energy of the system. Subsequent migration of the grain boundary takes place with time, and boundary motion was monitored through the change in the total potential energy (PE) of the system. Some snapshots of the 7.785° grain boundary migration were captured at 300K during the application of 0.0008 eV/atom driving force and shown in Fig. 2.27.



$t = 0$  ns



$t = 1$  ns



$t = 2$  ns

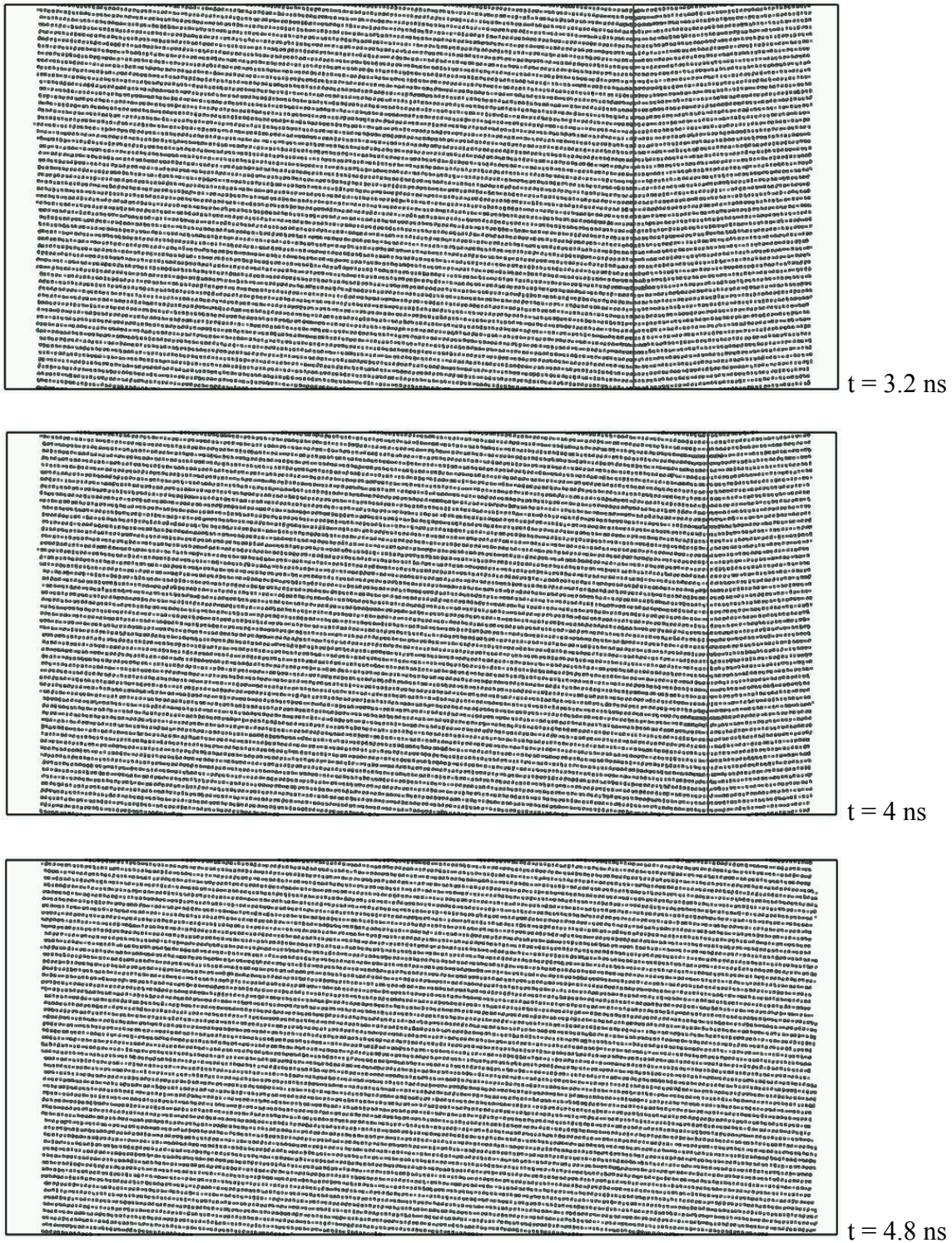


Fig. 2.27: Snapshots of the grain boundary migration with 0.0008 eV/atom driving force at 300K in pure Al. Free surfaces at the end of simulation cell normal to the interface.

During the course of the simulation, the grain boundary migration is monitored through the change in the total potential energy (PE) of the system. PE is observed to decrease with time resulting in shrinking of that crystal to which the artificial driving force is added. The energy decreases because the system tries to reduce the extra added potential energy. The profile of total PE of a bicrystal pure Al system during the  $7.785^\circ$  grain boundary migration with  $0.0008$  eV/atom driving force at  $300\text{K}$  is shown in Fig. 2.28 as a function of simulation time. The sudden drop in the potential energy after  $4.5$  ns indicates that the transformation is completed. The rate of change of PE with time is required to calculate the velocity of grain boundary motion. The steady state portion of this plot is considered to extract the slope. The boundary migration rate is proportional to the rate of change of potential energy with simulation time. The details of interface velocity calculation and LAGB mobility determination are discussed below.

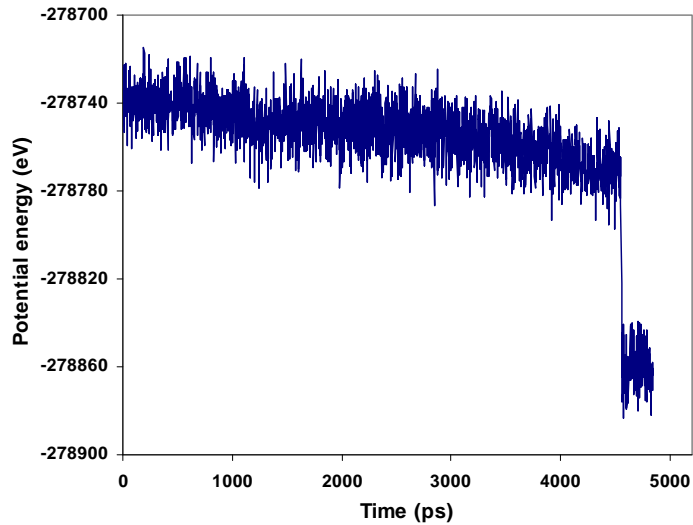


Fig. 2.28: Potential energy as a function of time during the grain boundary migration with  $0.0008$  eV/atom driving force at  $300\text{K}$ .

An alternative technique was also applied to compute the grain boundary migration velocity where the interface position was plotted as a function of simulation time. The grain boundary position is determined utilizing the centro-symmetry (CS) parameter approach [116] as discussed in the previous section. Grain boundary motion velocities, obtained from both approaches, are comparable at all driving forces. An example of such plot is shown in Fig. 2.29 for  $7.785^\circ$  boundary at  $0.002$  eV/atom driving force at  $300\text{K}$ . The figure is showing the migration of the low angle grain boundary under the application of artificial force. The boundary motion is linear with time. The slope of this plot determines the velocity directly.

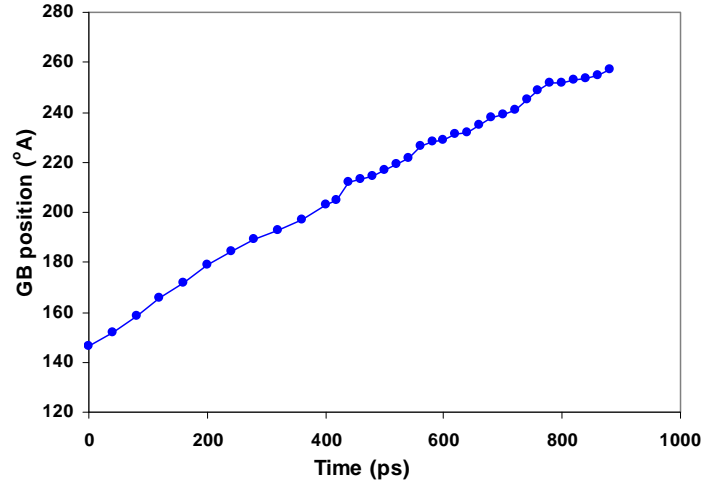


Fig. 2.29: Migration of the grain boundary with simulation time under applied force.

In this MD study, LAGB mobility is determined from the migration rate at which the interface is moving in ADF method. The grain boundary velocity is extracted by tracking the potential energy (PE) of the entire system with simulation time. Specifically the LAGB velocity is obtained from the following equation:

$$v = \frac{\dot{E} \Omega_s}{A(E_2 - E_1)} \quad (2.8)$$

where  $\dot{E}$  is the slope of PE vs. time plot,  $\Omega_s$  is the atomic volume of the fcc Al at the corresponding temperature,  $A$  is the cross sectional area of the simulation cell,  $E_2$  and  $E_1$  represent the potential energy per atom of the shrinking crystal and reference (growing) crystal respectively. The term  $(E_2 - E_1)$  in the equation is equivalent to the applied artificial driving pressure. The rate of PE change with time is calculated at each driving force and, by plugging this slope, the grain boundary velocity was determined following the Eq. 2.7. The expression of interface velocity in the Eq. 2.7 is based on the two characteristics constraints of the bicrystal system utilized in the MD simulation. The total number of atoms is the summation of atoms in the crystal-1 and that of crystal-2 ( $N_T = N_1 + N_2$ ). The potential energy (PE) of the entire system is the linear combination of weighted PE of both crystals ( $N_T E_T = E_1 N_1 + E_2 N_2$ ).

In Fig. 2.30, the velocity of grain boundary motion is plotted as a function of driving force at 300K for the  $7.785^\circ$  boundary. In this figure, the velocity is plotted for the whole span of driving force that is applied to track LAGB motion. The velocity does not maintain a linear relationship in the entire range of employed driving force. There are three regimes observed in the plot. The initial part with lower slope where the driving force is very low (0.0004 – 0.002 eV/atom), the middle part with higher slope in the range

of 0.003 – 0.03 eV/atom driving force, and there is plateau tendency in the last part with very high driving force (0.04 – 0.09 eV/atom). The phenomenon of non linear velocity at higher driving force was also observed in the MD study of solid-liquid interface migration [117]. The change in velocity–driving force behaviour has been discussed in terms diffusive vs. ballistic motion by Deng and Schuh [110].

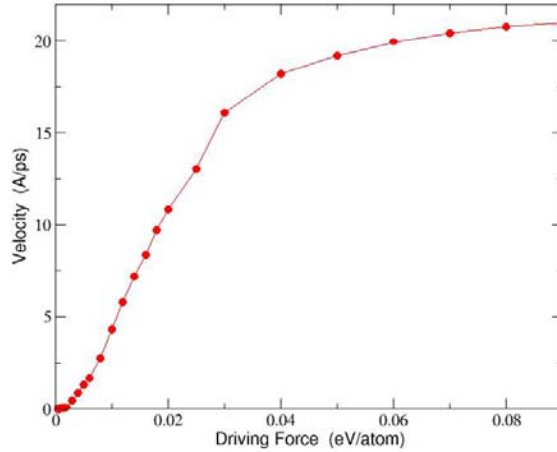


Fig. 2.30: Grain boundary velocity ( $v$ ) vs. applied driving force ( $P$ ) for the entire span of applied driving forces for the  $7.785^\circ$  LAGB. GB velocity is calculated using Eq. 2.8.

The grain boundary migration velocity deviates from the initial linearity at 0.003 eV/atom driving force. In spite of observing linearity in the middle region of Fig. 2.30, only the initial part of the interface velocity, at lower driving force, was considered to extract low angle grain boundary mobility. It should be noted that, by selecting the low driving force region, we are approaching the experimental driving force regime. In an experimental study of stress induced grain boundary motion, Winning et al. [82] reported the range of applied driving force as  $10^{-7} \sim 10^{-5}$  eV/atom. Therefore of, prime importance should be on selecting the proper range of driving force to determine grain boundary mobility utilizing the ADF technique in MD simulation. For LAGB migration, another essential consideration was found to be the order parameter (OP) which is 0 or 1 for the ideal grain orientation. But due to thermal vibrations, the OP would be greater than 0 or smaller than 1. This effect was taken into account by considering different cutoff values such as 0.25, 0.30, 0.35, 0.4 etc. for the lower cutoff,  $\xi_{low}$ . No discernable trend was found for the mobility with changing  $\xi_{low}$ , and in the results to follow each individual run was averaged to find the mobility. The average velocities of the grain boundary movement in the lower driving force region at 300K are plotted in Fig. 2.31. The magnitude of velocities in Fig. 2.31 was averaged over at least three different simulation runs and the error bars show 95% confidence levels. The solid line in the plot is the fit to a linear relationship. At 300K, the low-angle ( $7.785^\circ$ ) grain boundary mobility was found to be  $37 \pm 8.2$  Å/ps/(eV/atom) or equivalently  $3.9 (\pm 0.9) \times 10^{-7}$  m/s/Pa.

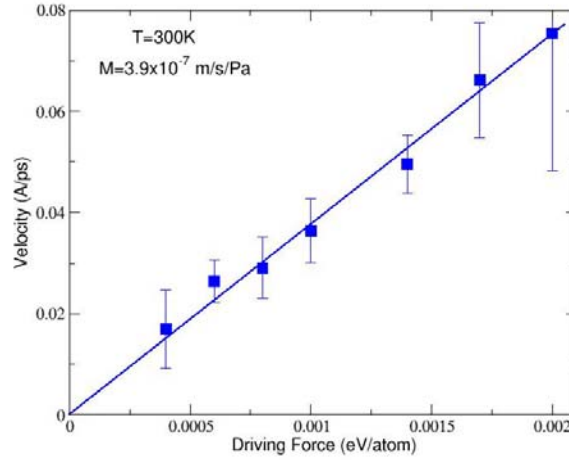


Fig. 2.31: Interface velocity ( $v$ ) plotted as a function of driving force ( $P$ ) in the regime of low driving force, from which the mobility is extracted. Error bars denote 95% confidence limits. The velocity is calculated using Eq. 2.8.

For LAGBs, the orientation difference between crystal-1 and crystal-2 is, by definition, small. The nearly equivalent orientations can lead the ADF method to misidentify atoms, which in turn implies that the actual driving force may not be equal to the selected values. For every run, we have corrected the driving force using a lambda integration technique [118-119]. In separate simulations of both the oriented (reference) and misoriented crystals, the actual potential energy increase vs. the applied value is integrated up to the selected  $V$ . It was found that the lambda integration can be quite significant, for example over 30% in the case of the  $7.785^\circ$  boundary.

In comparison to the experimental results, the magnitude of low angle grain boundary (LAGB) mobility obtained from these MD techniques is much higher. According to the measurement by Winning et al. [88] from a stress induced experimental technique, the LAGB mobility is around  $4.5 \times 10^{-16}$  m/s/Pa in pure Al at 473K, while our result is  $5.76 (\pm 1.3) \times 10^{-7}$  m/s/Pa at 300K from the artificial driving force simulation study and is  $3.0 (\pm 0.4) \times 10^{-6}$  m/s/Pa at 500K from the random walk approach. In a study of curvature driven high angle grain boundary migration in Al [77], it was reported that the simulation techniques provide much higher values of mobility compared to that from experiment. It was found in all the relevant previous studies [74-75,78] that the activation energies for grain boundary migration are much lower for the simulation than experiments. The reason of this discrepancy is usually attributed to the existence of the extrinsic factors such as impurity drag or dislocations even in the highly pure materials in the experimental investigations [75-77], while simulation techniques provide the intrinsic value of the grain boundary mobility.

For computing LAGB ( $7.785^\circ$ ) mobility at different temperatures, the artificial driving force method was also applied to some higher temperatures such as 400K and

500K. However, these simulations were unsuccessful. As discussed above, the ADF method, when applied to LAGBs, can result in misidentified atoms in the two grains of a bicrystal system. At higher temperatures, the thermal fluctuations are sufficiently large such that the order parameter computation fails. This leads us to predict that at 400K or higher temperature, the artificial driving force method is not suitable to determine LAGB mobility for very small misorientations.

## 2.8 Activation energy calculation and discussions

The Arrhenius plot of low angle grain boundary mobility of pure Al at  $7.785^\circ$  misorientation is shown in Fig. 2.32. This figure includes mobility from both ADF and RW techniques. As illustrated in the figure, mobilities at higher temperatures were obtained from the random walk method while mobilities at the lower temperatures were extracted from the artificial driving force approach. There is one common temperature (300K) where the two computational approaches were successful and it is evident that the mobilities determined from the two methods do not exactly match. To be precise, the mobility at 300K computed from artificial driving force method is found to be somewhat lower than that determined from the random walk approach at that temperature. But, as shown in the inset, both ADF and RW methods produce same LAGB mobility at 300K

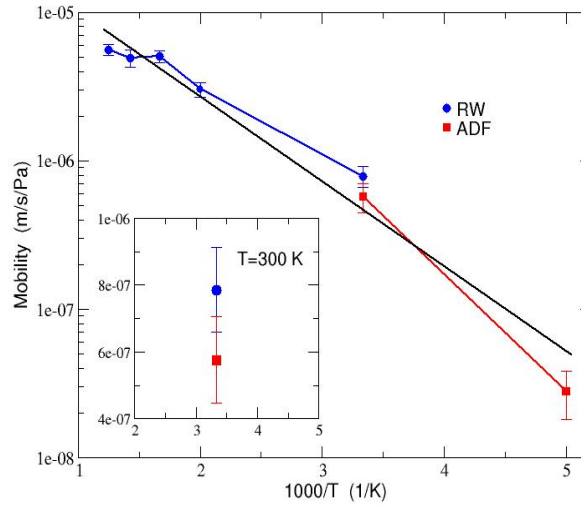


Fig. 2.32: Arrhenius plot of LAGB mobility ( $M$ ) versus inverse temperature ( $T$ ). Mobilities from both ADF and RW methods are presented here. The inset shows the results at  $T=300\text{K}$  and illustrates that the two MD techniques agree within uncertainty.

within numerical uncertainties. In a recent publication Mendeleev et. al. [120] provide a detailed comparison of the mobility of a  $\Sigma 5$  [010] tilt boundary in an EAM model of Ni using both an applied biaxial strain technique and the RW method. The authors conclude that the driven and zero driving methods yield the same mobility provided the linear

velocity-driving force regime is properly employed in the analysis. The agreement shown in Fig. 2.32 at  $T=300\text{K}$  and, as shown below, at  $T=700\text{K}$  for the  $23.07^\circ$  HAGB provide further evidence that grain boundary mobility is independent of driving force. However, in the results to follow, we also discuss the cases where discrepancies are found between the RW and ADF techniques and will address the sources of these discrepancies.

As shown in Fig. 2.32, a fit to a linear relationship was performed for all the mobilities from both techniques in the Arrhenius plot and slope of this linear fit provides the activation energy of low angle grain boundary motion. The activation energy of LAGB migration calculated from this plot, according to Eq. 1.2, is  $11\pm 2$  KJ/mol. In the experimental work conducted by Huang and Humphreys [90], the low angle grain boundary movement is investigated from the sub-grain growth kinetics and an activation energy is reported as 134 KJ/mol. As was found in all previous MD simulations of GB mobility, the activation energy is roughly a factor of ten lower than that of experiment.

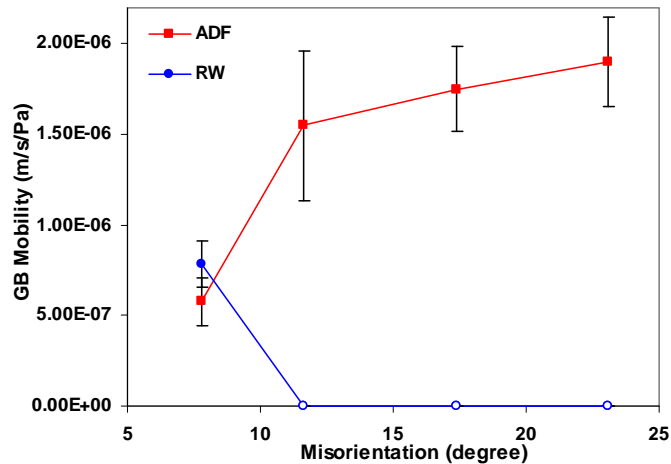


Fig. 2.33: Grain boundary mobility ( $M$ ) in pure Al plotted as a function misorientation angle ( $\theta$ ) at 300K from both ADF and RW method. The open symbols, in RW method, indicate that the mean square displacement of grain boundary was not enough to compute mobility.

In addition to investigating in detail MD techniques for computing LAGB mobility, this study has also been extended to determine the grain boundary mobility as a function of misorientation angle and temperature. The magnitudes of mobility were determined using both the RW technique and the ADF method and corrected through the lambda integration technique. The extracted mobilities, from the ADF approach, for [112] grain boundaries in pure Al at 300K are plotted against the misorientations in Fig. 2.33 and a dramatic increase in mobility between low angle and high angle boundaries is observed. It is interesting to note that in an experimental study by Winning et al [12] a similar jump, although much larger, in mobility at a misorientation of roughly  $13.6^\circ \pm 0.55^\circ$  was measured. The authors attribute the abrupt change in mobility to the

interaction of the moving boundary with network dislocations. It is tempting to conclude from the MD data that a discontinuous jump is also observed in the case of intrinsic mobility. In contrast, however, the work of Karma et al. [10], as well as theoretical predictions [11], indicate that the intrinsic mobility should decrease as a function of misorientation in the low angle limit.

In order to understand the ADF results of Fig. 2.33 the mobility computation was repeated using the RW method. At 300K in the case of  $11.655^\circ$ ,  $17.408^\circ$  and  $23.07^\circ$  boundaries, the mean square displacement of the boundary was found to be essentially zero suggesting zero mobility and the results are shown in Fig. 2.33. The RW results are qualitatively consistent with past studies and are in agreement with theory [11]. The RW data also propose that the ADF derived mobilities are in error. The reason for the discrepancy between the RW and ADF results at higher misorientations is illustrated in Fig. 2.34. Here the grain boundary velocity, computed from ADF method, is plotted against driving force for misorientation  $23.07^\circ$  and  $7.785^\circ$  at 300K. The figure shows that for the low angle case a linear extrapolation of the data to zero velocity intersects the origin, whereas for the higher angle boundary the extrapolation, although linear, intersects the x axis at a high driving force. The results thus indicate that there is a barrier at higher misorientation, in terms of driving force, which must be overcome in order to observe any motion of the grain boundary. This observation implies that the ADF method is providing us misleading mobilities for high angle grain boundaries at 300K as we need to apply unrealistically large driving forces to initiate boundary motion.

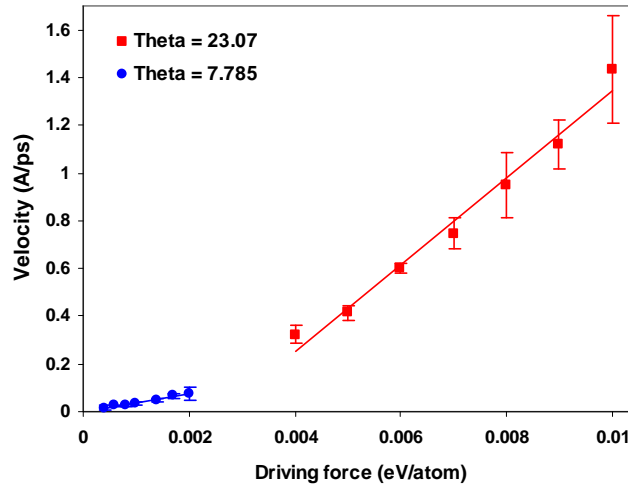


Fig. 2.34: Grain boundary velocity ( $v$ ) vs. driving force ( $P$ ) plotted for  $23.07^\circ$  and  $7.785^\circ$  misorientation at 300K showing a driving force threshold needed to start grain boundary movement for the HAGB.

Both RW and ADF methods have also been employed to compute grain boundary mobility at high temperature (700K) as a function of misorientation angle. In both

methods, we followed the same computational procedure as in the 300K case to compute grain boundary mobility in  $11.655^\circ$ ,  $17.408^\circ$  and  $23.07^\circ$  systems. The square symbols in Fig. 2.35 represent the data obtained from the RW technique and the results show that the mobility decreases with increasing misorientation at 700K in pure Al. Our RW result of mobility at high temperature is found, as discussed above, to be consistent with a previous MD investigation by Karma et. al [10], where they computed mobility at 1200K in the pure EAM Cu system. This trend of mobility variation with misorientation also confirms theoretical considerations [11] and is also observed in a previous MD study [9].

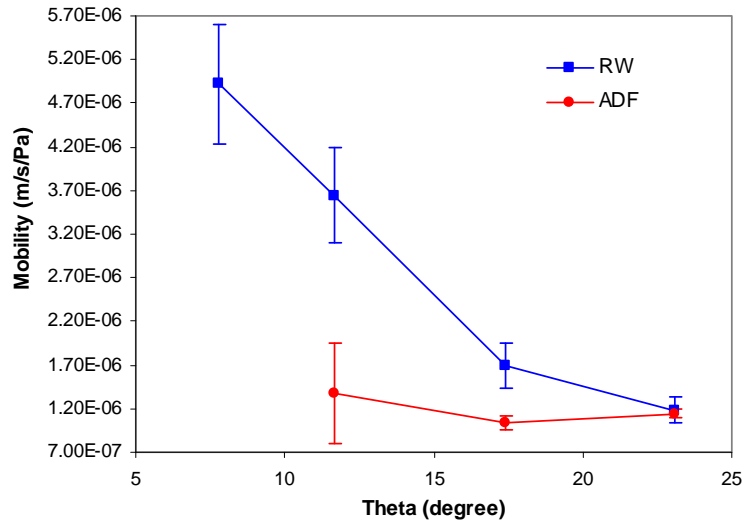


Fig. 2.35: Grain boundary mobility ( $M$ ) plotted as a function of misorientation ( $\theta$ ) at  $T = 700\text{K}$  for both ADF and RW technique.

Fig. 2.35 shows that the magnitude of mobility in  $17.408^\circ$  and  $23.07^\circ$  systems determined from RW and ADF method are very close, but there is noticeable difference in the case of  $11.655^\circ$  system at 700K. As discussed earlier, the large thermal fluctuations at high temperature can cause a failure of the order parameter computation with the decrease in misorientation and we were unable to apply the ADF method successfully at the lowest misorientation. However, Fig. 2.35 also shows considerable deviation between the RW and ADF methods at  $11.655^\circ$  and  $17.408^\circ$ , which suggests that the assignment of an order parameter is also problematic at these higher angles. The order parameter difficulty is also manifest in the dependence of mobility on the cutoff value (see Eq. 2.7 above), as is illustrated in Fig. 2.36. The grain boundary mobility for the  $23.07^\circ$  boundary (squares) at high temperature is roughly the same for different lower cut off values of order parameter, as was the case for the ADF method for all boundaries at lower temperature. But, the mobility in  $11.655^\circ$  at 700K varies considerably with the change in lower cut off value of order parameter and the computed value does not appear to converge. This result suggests that the ADF method provides a misinterpretation of the

11.655° mobility at 700K in pure Al and illustrates the need to examine the effect of lower cutoff value when computing the mobility via the ADF method.

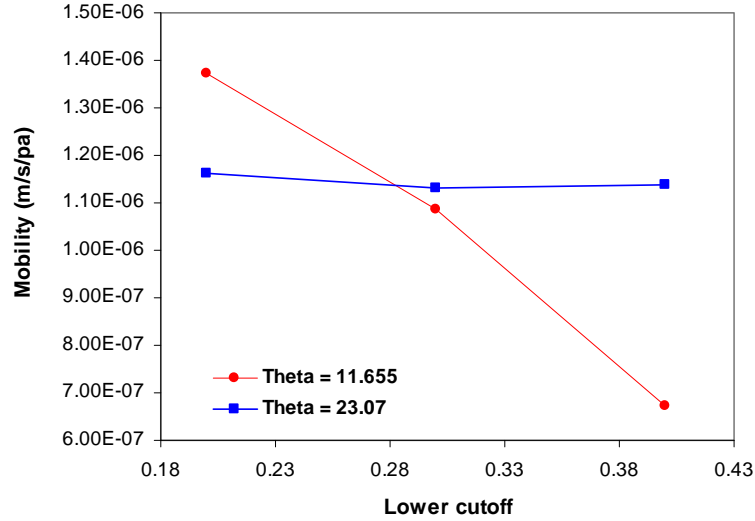


Fig. 2.36: GB mobility ( $M$ ) plotted at different lower cutoff ( $\xi_{lo}$ ) of order parameter (OP) showing variation of mobility with OP for 11.655° and 23.07° boundaries at 700K.

## 2.9 Employment of different extrapolation functions

The above results illustrate that there can be discrepancies between the ADF and RW techniques for the computation of grain boundary mobility. Therefore we have investigated one other factor that may play a role in the mobility computation from the ADF technique. In Eq. 2.7, the extrapolation function used in the ADF formalism was introduced. However, this functional form is an arbitrary choice and there exists an infinite number of extrapolation schemes. Therefore we have repeated the mobility simulations using three additional extrapolation functions. The functions, that we considered, are as follows:

$$\text{Original: } u = \frac{V}{2}(1 - \cos \pi x)$$

$$\text{Polynomial: } u = V(6.432x^3 - 11.756x^5 + 8.718x^7 - 2.393x^9)$$

$$\text{Tanh: } u = \frac{V}{2} \left( 1 - \tanh \left[ \frac{a}{x} - \frac{a}{1-x} \right] \right)$$

where  $x = 2\omega_i/\pi$  and  $\omega_i$  is the normalized order parameter. In the hyperbolic of the tangent function,  $a$  refers to a tuning parameter for that extrapolation function.

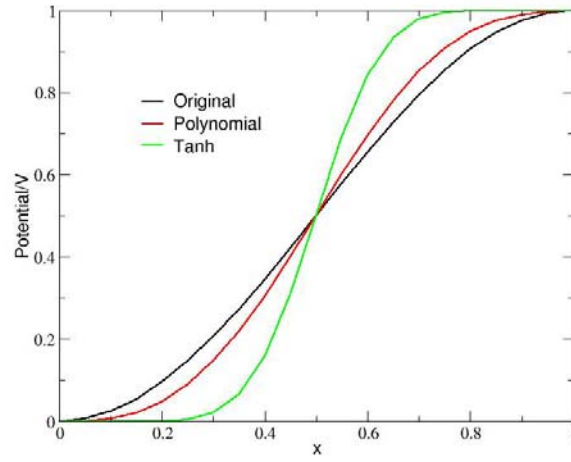


Fig. 2.37: Profile of potential energy vs. normalized order parameter for all the investigated artificial functions. All profiles show the same features except the magnitude of slope at the interface. For Tanh function,  $a=1$  is used in this plot.

The potential energy curves, corresponding to each function, are shown in Fig. 2.37 illustrating their characteristic features, where  $x=0$  and  $1$  refers to the reference crystal and misoriented crystal respectively and the functions are odd about  $x=0.5$  and  $u = V/2$ . In addition, all extrapolation functions exhibit a zero slope at  $x=0$  and  $x=1$ . It is noticeable that the only difference, among the three curves, is the change in slope in the energy curve at the interface region between two crystals. The polynomial function produces a higher slope than that of the original function, while the Tanh function provides the highest slope at the boundary. In fact, the aim of choosing different extrapolation functions was to investigate the effect of change in slope in the applied energy profile on the magnitude of the MD derived low angle boundary (LAGB) mobility. This result is shown in Fig. 2.38, where LAGB migration velocities are plotted against applied driving force for all the employed functions.

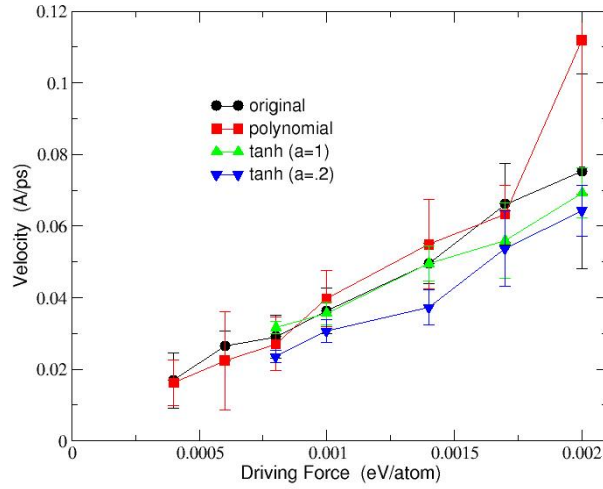


Fig. 2.38: LAGB velocity plotted versus driving force at different artificial functions for the comparison of mobility.

It was found that the variation of interface velocity with driving force is approximately constant, considering uncertainties, for all investigated artificial functions. The extracted magnitudes of mobility at different artificial functions are as follows; Original:  $3.9 (\pm 0.9) \times 10^{-7}$  m/s/Pa, for Polynomial:  $4.0 (\pm 0.9) \times 10^{-7}$  m/s/Pa, for Tanh (a=1):  $3.3 (\pm 0.8) \times 10^{-7}$  m/s/Pa and for Tanh (a=0.2):  $3.5 (\pm 1) \times 10^{-7}$  m/s/Pa. Therefore, it can be stated that the ADF technique is not sensitive to the choices of the extrapolation functions as the mobility does not change significantly.

## 2.10 Summary of the chapter

In this chapter we focused on determining the low angle grain boundary (LAGB) mobility in pure Al system as this parameter is significantly important in developing the analytical model of recovery kinetics. But, to date, few works have been conducted to capture the LAGB motion both experimentally and computationally. We determined LAGB mobility of [112] symmetric grain boundaries in pure Al using two different molecular dynamics (MD) techniques, namely the artificial driving force (ADF) method and the random walk (RW) method. Detailed comparison of the two methods shows that they produce nearly the same mobility, within error bars, at 300K for the grain boundary with  $7.785^\circ$  misorientation and the  $23.07^\circ$  boundary at a temperature of 700K. A thorough investigation demonstrates that the ADF method is not applicable to compute mobility at temperatures  $\geq 400$ K for the case of the lowest misorientation. There is also considerable discrepancy between the RW and ADF results for all misorientation less than  $23.07^\circ$  at the high 700K temperature. The MD results indicate that considerable care must be taken in applying the ADF technique to the case of low angle boundaries.

The ADF technique is found to be not sensitive to different choices of the extrapolation function used to assign the artificial energy in the grain boundary region. The activation energy of the LAGB mobility has been extracted from an Arrhenius plot and is observed to be approximately ten times lower than the experimental results. A similar discrepancy between experiment and simulation has been observed in virtually all previous MD studies. The discrepancy is most likely due to the difference between the intrinsic mobility and the mobility determined in the presence of impurities and/or network dislocations.

## CHAPTER 3

### **Solute pinning effect on low angle grain boundary motion**

In chapter 2, the low angle grain boundary (LAGB) mobility was determined in pure Al system and the dependence of boundary mobility on the misorientation and temperature was investigated. The MD derived results discussed in the last chapter did not include the effect of the solutes on the boundary migration. As mentioned in chapter 1, even small amount of solute can provide strong retarding effect on the grain boundary motion. Therefore, in this chapter we will determine the mobility, especially for LAGB, in Al-Mg alloy to investigate the solute pinning effect on the boundary migration. We will use two different approaches, namely segregated and distributed solute system, in artificial driving force (ADF) technique.

#### **3.1 Literature review**

Grain boundary motion controls the rate of the important metallurgical processes of grain growth and recrystallization. The kinetics of boundary motion has been examined in a number of studies and considerable attention has been paid to the solutes and impurities on the boundary mobility. The effect of solute drag during different processing has been investigated in detail over the last 50/60 years. It is now well established that the presence of even very small amount of solute can retard the grain boundary motion significantly. Both experimental and computational investigations have been carried out to study this phenomenon explicitly and to incorporate it to different thermo-mechanical processes. A systematic review of the literature available for solute drag and pinning effect on the migration of grain boundary will be discussed below.

Because of the significance of solute drag on the interface motion, numerous studies had been conducted to develop its basic fundamentals. The first quantitative analysis was published in late 1950 by Lücke and Detert [32], where solute drag effect was reported in terms of the force exerted by a solute atmosphere. They concluded that the attraction force between the grain boundary and the solute atoms segregated into it exerts drag on the migrating boundary. In the study of recovery and recrystallization, Lücke and Stüwe [36] quantitatively described the solute drag in terms of the impurity controlled grain boundary motion and its temperature dependence. The authors reported the following equation to express the total drag force provided by the impurities:

$$P_i = -N_v \int_{-\infty}^{+\infty} C \frac{dE(x)}{dx} dx \quad (3.1)$$

where,  $N_v$  is number of atoms per unit volume,  $C$  is the impurity concentration,  $E(x)$  is the boundary–solute interaction energy. The term  $\frac{dE(x)}{dx}$  refers to the force by an impurity atom on the boundary and the total force is obtained by integrating over all atoms. Lücke and Stüwe [37] also developed an atomistic model to estimate the impurity drag on the boundary migration. There are some major limitations [38] in Lücke and Detert’s work [32]. In fact, the authors made some questionable assumptions [38] in their studies.

Lücke’s first work was followed in 1962 by Cahn’s [38] classic model of impurity drag on the boundary migration, where the number Lücke’s approximations was reduced. Cahn’s description was mainly based on the drag force exerted by impurity atoms on the grain boundary. He modified Lücke and Stüwe equation by adding a term and obtained the following equation to describe the total impurity drag force on the boundary:

$$P_i = -N_v \int_{-\infty}^{+\infty} (C - C_o) \frac{dE(x)}{dx} dx \quad (3.2)$$

where,  $C_o$  is the impurity concentration in the bulk material considerably away from the grain boundary at steady state. In this pioneering study, Cahn suggested two types of force–velocity relationships depending on the impurity concentration of the system. Considering both low and high velocity limit, the approximate impurity drag equation of the Cahn model is:

$$P_i = \frac{\alpha VC_o}{1 + \beta^2 v^2} \quad (3.3)$$

where,  $\alpha$  and  $\beta$  are impurity drag parameters that are dominant at very low and high velocities respectively. These two parameters are nearly reciprocal of the diffusivity and are described as below:

$$\alpha = 4N_v k_B T \int_{-\infty}^{+\infty} \frac{\sinh^2 \frac{E(x)}{2k_B T}}{D(x)} dx \quad (3.4)$$

$$\alpha/\beta^2 = \frac{N_v}{k_B T} \int_{-\infty}^{+\infty} \left( \frac{dE}{dx} \right)^2 D(x) dx \quad (3.5)$$

According to Cahn’s analysis, at low driving forces the impurities segregated to the boundary are able to diffuse along with the moving boundary, producing a large drag. In contrast, at higher driving forces the velocity can exhibit a discontinuous jump where the boundary has broken free of the solute atmosphere and the drag effect is reduced. The transition from low to high driving force occurs at  $v\beta = \sqrt{3}$ . Cahn’s solute drag model is illustrated in Fig. 3.1, where driving force vs. velocity profile is shown at different impurity concentration. At the applied force, after the inflection point, the faster diffusing impurities can exert drag on the boundary. Therefore, Cahn’s treatment shows higher solute drag at low boundary velocity that reaches maximum at a critical velocity and reduces to negligible drag at high velocity.

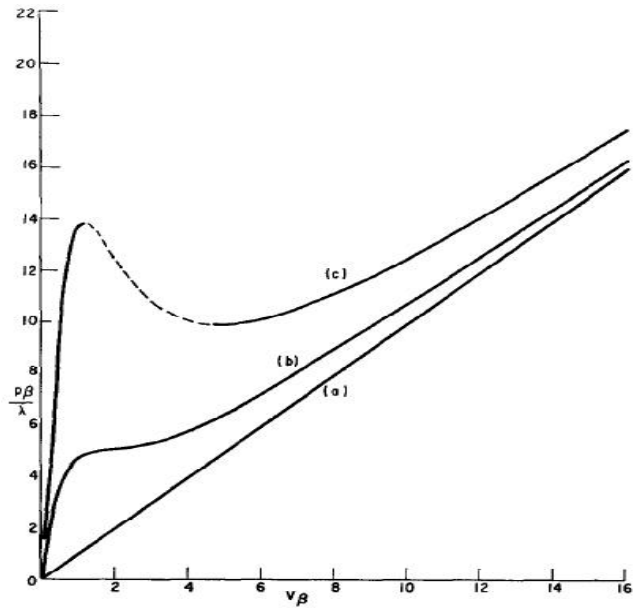


Fig. 3.1: Cahn model: the applied driving force as a function of boundary velocity at different solute concentration. The dashed part shows the breakaway region [38].

The Cahn-Lücke-Stwüie impurity drag analysis is applicable only to the motion of grain boundaries in one phase materials during, for example, recrystallization and grain growth. This model has been applied to the case of one dimensional interface motion. In 1975, Roy and Bauer [121] developed a two dimensional solute drag model of boundary migration considering lateral diffusion of impurities. The authors described the drag effect on the change in boundary shape. Later, this approach has been modified by Korzhenevskii et al. [122] and considerably different stability behaviour was reported.

In addition to Cahn-Lücke-Stüwe model, another important solute drag analysis was developed by Hillert and Sundman [39] in 1976. This model focused on the dissipation of free energy due to the diffusional processes that take place during interface migration. The authors proposed the following equation to illustrate the solute drag force on the migrating boundary:

$$P_i = -N_v \int_{-\infty}^{+\infty} (C - C_o) \frac{d(\Delta G)}{dx} dx \quad (3.6)$$

where,  $\Delta G$  represent the dissipation of Gibbs energy caused by diffusion. Hillert et al. modified the Cahn's equation by changing the driving force of interface motion from solute-boundary interaction energy to free energy dissipation. In contrast to Cahn model, Hillert's analysis reported a continuous raise in the solute drag that tends to reach an asymptotic value with increasing velocities. The treatment of Hillert et. al. can be applied to phase transformations and grain growth as well. A complete analysis of this model of solute drag phenomena is described in detail in Ref. [123]. Subsequently, Hillert extended his model [124] to estimate the solute drag and the generalized approach can be applied equivalently to grain boundary migration and phase transformation.

Hillert's and Cahn's models are considered to be two leading theoretical approaches in the literature of solute drag and both models have been employed in several studies [125-126,45-51] of phase transformation and grain growth. Brechet and Purdy extended the solute drag studies to study examine the effect of elastically induced force [45], to describe the dilute massive phase transformations [46] and to demonstrate solute-solute interactions in ternary solid solutions [57]. Cahn's model has also been utilized in some other studies, such as, by Sinclair et al. [58] to analyze quantitatively the solute drag effect of Nb on recrystallization and grain growth of ultra-high-purity bcc ferrite, by Zurob et al. [43] to describe the interaction of static recrystallization and strain induced precipitation and by Lissel et al. [59] to illustrate the solute drag effect during hot rolling of Nb-steel. Mendeleev and Srolovitz have captured some additional features through the study of solute drag on boundary migration in the case of both regular solid solutions [61] and ideal solutions [62].

The effect of solute atoms on migrating boundary has also been studied in terms of discrete pinning points along the boundary [127-128]. In a relevant study, Machlin [127] described retarding of the migrating interface by the formation of cusps at the grain boundary during the interaction with solutes. In another solute pinning model, Hersent et al. [128] considered that the key effect of the cusping is the stress concentration or equivalently pinning force on the cusp-forming atoms. In Fig. 3.2, a schematic representation of cusp formation at the position of solute atoms on the moving boundary (Fig. 3.2(a)) and the resulting cusping force,  $F_c$ , on the solutes (Fig. 3.2(b)) are illustrated. The authors reported that the restraining pressure triggers the solute atoms out of the boundary and determines the rate of grain boundary migration in an alloy system.

According to the Cahn solute drag model, the force-velocity relationship in the high driving force limit is linear with a mobility that is independent of the bulk concentration. The work of Hersent [128] suggests that in fact the uniform concentration field can act as a back-stress on the moving boundary in the high driving force limit. The authors provide a theoretical model for the back stress, which predicts a linear dependence on composition.

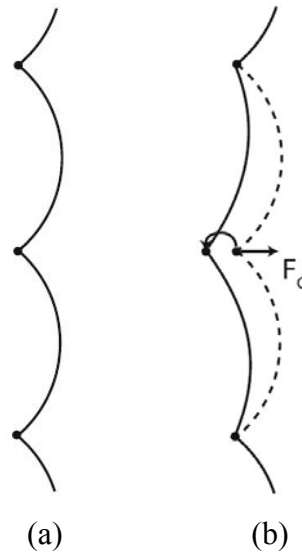


Fig. 3.2: Schematic illustration of (a) cusp formation on solute atoms on the grain boundary, and (b) pinning force ( $F_c$ ) on the cusp forming solute [128].

In addition to on high angle grain boundaries, very few solute drag studies have been conducted on the low angle boundary migration. In a study of subgrain boundary motion by Sandström [25] in 1977, it was reported that the mathematical description of solute drag effect for the high and low angle boundary is analogous, even though the two cases follow different growth mechanism. The grain growth takes place through the attachment of individual atoms to the growing crystal. In contrast the subgrain grows by the combination of climb and glide of dislocations that form the boundary. The authors illustrated that the solute drag on sub-boundaries in alloy system is mainly due to the interaction of solute atoms with the intrinsic dislocations as the solutes are likely to cluster around the dislocations. It was described that the elastic misfit interaction between solutes and dislocations provides important to their interaction energy [129] that controls the solute drag during subgrain growth. In another study, Sandström et. al. [130] investigated subgrain growth during annealing and proposed different growth mechanism in Al and Al-1% Mn. The authors demonstrated that the sub-boundaries move through the combined motion of the boundary dislocations in alloys system, while, on the contrary, sub grain growth occurs extractions of boundary dislocations separately. In a study of impurity atoms controlled stress induced low angle tilt boundary motion in Zn-Ag alloys, Syn et. al. [131] observed jerky motion during boundary migration. The authors attributed

the reason of this discontinuous motion to the impurity and solutes that segregated at the low angle boundary and pin the intrinsic dislocation motion. Their observations are in agreement with other previous studies [72] of LAGB motion in Zn crystals.

Due to the importance of solute drag, in addition to the classical analytical models and experimental studies, a number of computational investigations had been conducted to capture the micro-scale, nano-scale and atomistic features of this phenomenon. One such widely used computational tool is the phase field model, which employs a description of a diffuse interface to study solute drag effect on boundary migration. In a phase field study by Cha et. al. [132], the solute drag effect is incorporated by considering segregation potential well in the grain boundary. Their 1-D steady state model reproduces both Cahn and Hillert's treatment. Grönhagen [133] presented a phase field model of solute drag by incorporating concentration dependent potential well in the Gibbs free energy. The authors described the dynamics of solute drag by illustrating the variation of composition and drag effect as a function of velocities. Phase field simulation has also been utilized to study the effect of solute drag during the austenite to ferrite phase transformation in steel by Loginova et al. [134], where the simulation results produce qualitatively similar features as that of solute drag.

The phase field crystal (PFC) model, whose defining feature is the ability to capture atomistic length scales but diffusive time scales, is another new technique that has emerged [135-136] to study solute drag. Greenwood et al. [137] developed a new approach for a binary PFC model to investigate applied pressure induced interface motion and capture solute drag on the boundary migration. Their results show good agreement with Cahn's classic impurity drag theory. In addition, Kinetic Monte Carlo (KMC) and Molecular Dynamics (MD) simulation have also been utilized to investigate solute–boundary interactions at the atomistic length scale. Using KMC, Mendeleev et. al [62] simulated boundary migration in the presence of impurities and concluded that the formation and propagation of kinks controls the boundary migration and hence classical continuum models are not applicable. A three dimensional KMC model was developed by Wicaksono et al. [138], where the effect of solute concentration and solute diffusivity on the solute drag pressure was studied. The authors reported that the solute diffusivity affects the maximum drag pressure, which is caused by the change in the interface structure during migration. Besides KMC simulation, over the last decade Molecular Dynamics (MD) has been proven to be effective in investigating interface migration and determining its associated kinetic properties [74-84]. Recently solute drag has been studied using MD during liquid-solid phase transformation in a model Lennard-Jones and Ni-Cu binary system by Yang et al. [139].

To date very few works [11-12,140-141] have focused LAGB motion and its associated features, such as mobility. In the previous chapter, determination of LAGB mobility is described in detail utilizing different MD techniques in an EAM-Al system. It was demonstrated that the boundary mobility decreases with increasing misorientation at 700K in pure Al, which agrees well with another MD study of mobility determination in

EAM Cu system by Karma et. al [10] and is consistent with the theoretical predication by Cahn and Taylor [11]. The present work is an investigation of solute (Mg) interaction with migrating grain boundaries, especially low angle boundaries, in a model Al-Mg binary system utilizing MD simulations. In this study, we focused on LAGB as not much work has been conducted to examine sub-boundary motion in the presence of solute atoms. We will be using the artificial driving force (ADF) technique to induce grain boundary motion in MD simulation. The boundaries chosen for this study are [112] symmetric tilts with Mg content varying from 0.02% to 2% and with different misorientation angle. Specifically we will focus on the solute pinning effect and threshold driving force for depinning the boundary. In addition, we will investigate the mobility in the high driving force limit and its dependence on solute concentration, an effect, as mentioned above, that is absent in the classic model by Cahn [38]. The next section includes the binary simulation structure and numerical procedures. In the results and discussion section, the pinning effect of the solutes will be summarized for segregated and distributed solute system. A comparison, in terms of threshold applied force, of these two approaches suggests that the dispersed solute will provide less restraining force on the LAGB motion, but still provides reduced boundary velocity than that of pure Al system.

### 3.2 Simulation details

The atomic forces of the model Al-Mg binary system are given by the same embedded atom type interatomic potential, developed by Mendeleev et. al [111], which we have used for LAGB mobility determination. In this study, a bicrystal of Al-Mg system with a symmetric [112] tilt boundary was used to perform all the simulations for investigating solute interaction with a migrating interface. A combination of Monte Carlo (MC) and Molecular Dynamics (MD) simulation has been utilized to equilibrate the system. The first step in the simulation procedure is the construction of the tilt boundary in pure Al and we have followed the similar procedure described in the first chapter. The structure was a bicrystal consisting of two differently oriented grains and the misorientation was defined as the angular difference between these two crystals. The binary system with lowest misorientation has  $7.785^\circ$  boundary and dislocation spacing of 5 atomic planes along the grain boundary and contains a total of 82895 atoms. Crystal-1 of the binary bicrystal slab has the orientation  $x \Rightarrow [17\ 19\ \bar{1}]$ ,  $y \Rightarrow [\bar{1}\ 1\ 2]$ ,  $z \Rightarrow [39\ \bar{33}\ 36]$  and crystal-2 has  $x \Rightarrow [19\ 17\ 1]$ ,  $y \Rightarrow [\bar{1}\ 1\ 2]$ ,  $z \Rightarrow [33\ \bar{39}\ 36]$  and the x-axis was the direction normal to the grain boundary. As mentioned in Chapter-2, there were free surfaces x-direction on both sides of simulation cell to eliminate the shear stress that develops during the boundary migration due to the coupled shear motion at the interface as discussed by Cahn and Mishin [107]. Periodic boundary conditions were used in the remaining two spatial directions. In addition to  $7.785^\circ$  boundary, three more binary Al-Mg bicrystals with  $11.655^\circ$ ,  $17.408^\circ$  and  $23.07^\circ$  misorientation at 300K were used to

study the dependence of solute–boundary interaction on the magnitude of boundary misorientation at different solute concentration.

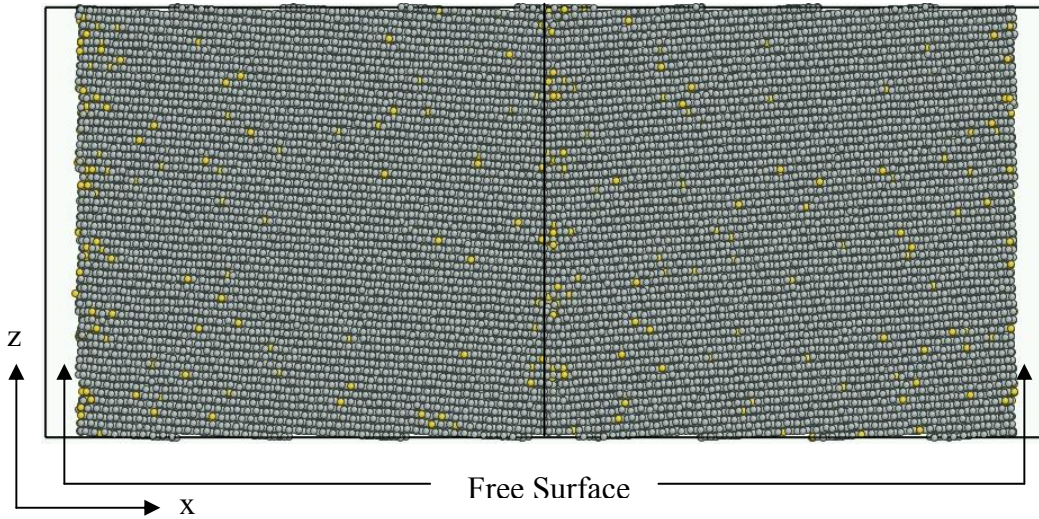


Fig. 3.3: Simulation geometry of Al-2%Mg binary system with [112] symmetric tilt  $7.785^\circ$  boundary at 300K. The golden colour atoms are solute atoms (Mg). The solid line shows the position of the grain boundary and there are free surfaces at both ends.

To generate a binary alloy system, the initial pure Al system in MD was subsequently followed by loading the system with Mg solutes using MC simulation. A Semi grand canonical ensemble (SGCE) was employed in the MC simulations to obtain an equilibrium distribution of the solutes (Mg) in the bulk phases and at the grain boundary of the binary Al-Mg alloy system. In addition to sampling atomic displacements, the MC steps sampled compositional changes by attempting changes of atom type during the simulation according to an imposed chemical potential difference between the species. The SGCE approach is discussed in detail in the next section. The entire simulation system was not allowed to change its dimension during the SGCE runs. Total runs of approximately  $5 \times 10^4$  steps per atom were applied for the relaxation of composition profiles. The Monte Carlo controlled relaxed binary bicrystal was then transferred to MD simulation to relieve the stress of the entire system. The equilibration runs in MD was performed using an NVT (constant number of atoms, volume and temperature) ensemble and the stress relaxation has been taken care of by the free surfaces. The equilibrium will be obtained when the change in energy and pressure of the binary system will be in a steady state. A typical equilibrated and stress free simulation geometry of Al-2%Mg bicrystal system with  $7.785^\circ$  boundary at 300K is shown in Fig. 3.3. The solute atoms (Mg) are shown in golden colour in the figure. All the Al-Mg binary systems at different misorientation were generated following the same technique as that of  $7.785^\circ$  boundary. A time step of 1 fs has been used in all MD runs of equilibration and statistics generation. We have used LAMMPS (Large-scale Atomic/Molecular Massively Parallel Simulator) code [114-115] to conduct the MD

simulations in this study. The well equilibrated Al-Mg binary simulation system was utilized for applying driving force on the boundary.

### 3.3 Semi grand canonical ensemble (SGCE)

As mentioned in the earlier section, the equilibrium solute distribution in the entire binary Al-Mg system was obtained through the employment of Monte Carlo (MC) simulations in the so-called Semi grand canonical ensemble [142,143]. SGCE refers to the system of fixed chemical potential difference between solute and solvent species,  $\Delta\mu = \mu_{Mg} - \mu_{Al}$ , fixed temperature and total number of atoms with variable number of Al and Mg atoms, that is, the solvent and solute atoms can switch types. Actually MC simulation allows the system to change relative composition depending on the applied external driving force ( $\Delta\mu$  and  $T$ ) during the simulation. In these simulations, an external chemical potential is imposed which leads the system to a stable state by adjusting the solute concentration over the course of simulation and eventually an equilibrium composition is achieved corresponding to that applied  $\Delta\mu$  for each specific temperature.

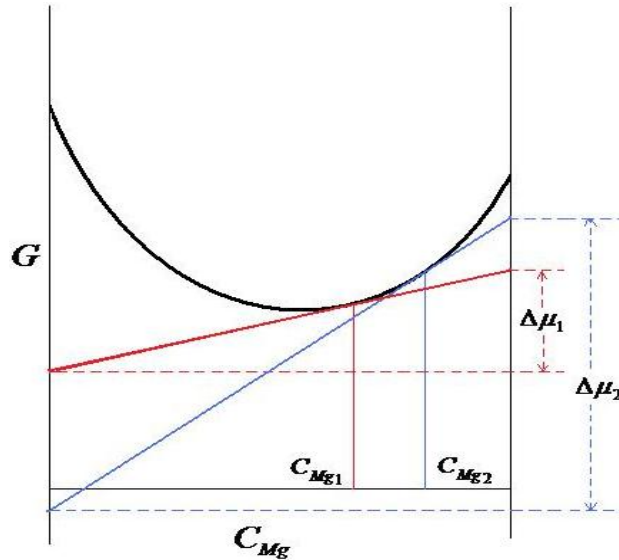


Fig. 3.4: Principle of the Semi grand canonical ensemble (SGCE) approach in the Monte Carlo simulation showing the change in solute concentration with the variation in chemical potential differences between the species

The principle of SGCE approach in the Monte Carlo simulation is illustrated schematically in Fig. 3.4. This is a schematic plot of free energy as a function of the solute composition, which is Mg in this study. The difference between end points, which intersect the  $G$  axes, of a tangent drawn to the free energy curve represents the chemical potential difference while the point at which it is tangent to the curve describes the

equilibrium composition for that  $\Delta\mu$  at a certain temperature. If  $\Delta\mu_1$  is applied to the system, this will produce equilibrium Mg concentration  $C_{Mg1}$  in the entire binary system. Imposing a higher value of chemical potential difference  $\Delta\mu_2$  ( $\Delta\mu_2 > \Delta\mu_1$ ) will result in a higher magnitude of solute concentration  $C_{Mg2}$  ( $C_{Mg2} > C_{Mg1}$ ) as shown in Fig. 3.4. The employment of  $\Delta\mu$  will also place the Mg atoms in the positions where these are supposed to be at a fixed temperature. Following this procedure, all the binary Al-Mg alloys were generated with the equilibrium solute concentration and distribution in the MC simulation using SGCE technique.

### 3.4 Application of driving force

To cause the migration of the grain boundary, the artificial driving force (ADF) technique [79] has been employed in the binary simulation geometry. The details of the application of driving force according to this approach are discussed in Ref. [79]. Briefly, a synthetic potential energy, which depends on the spatial orientation of the atoms, is applied to one of the crystals of the bicrystal system. The position of the atoms in either crystal was determined by an order parameter (OP) description [79]. As mentioned in Eq. 2.5, OP is calculated from the position of the nearest neighbours. The OP profile of the entire system shows higher value for the misoriented crystal compared to that of the reference crystal, as illustrated in Fig. 2.25. The atoms in between these two crystals are in the region of grain boundary, where the driving force is applied.

After defining the atom positions in each crystal, the potential energy is assigned using the OP cut off values according to Eq. 2.7. As shown in Fig. 2.26, the slope of applied potential energy profile in the interface region determines the force that will drive the grain boundary. Besides the atom position from OP profile, the application of artificial force requires the proper orientation of the nearest neighbour atoms. The orientation of the atoms was introduced through the rotation matrix as summarized in Table 2.1 using the corresponding lattice parameter of the alloy systems. We applied the artificial driving pressure to the misoriented grain that causes shrinking of this grain and growth of the reference grain through the migration of the boundary. As the entire simulation system consists of equilibrium distribution of solute atoms, the migrating interface interacted with the solute during its motion. The GB-solute interaction behaviour was investigated as a function of different amount solute content and misorientation in the Al-Mg binary system at 300K.

In the ADF technique, a wide range of driving forces has been applied for the migration of the boundary at 300K. The migration of the boundary was tracked by monitoring the change in the total potential energy (PE) of the system. An NVT ensemble was used as the controlling thermostat for the binary crystal during the simulation period. The rate of change of PE with time yields the velocity of the boundary motion and then

the mobility can be calculated from the migration rate. An advantage of the ADF method is that the amount of applied energy can be varied up to any extent. Large applied force might be needed to overcome any barrier resulted from the solute atoms. However, at high driving forces the atomic mechanism of migration may be altered [110] and may not represent the actual growth mechanism in real boundaries. To compare the grain boundary mobility in the Al-Mg alloy with that of pure Al, the region of applied driving force was analyzed critically. As reported in the previous chapter, attention must be paid to the selection of applied pressure for the extraction of mobility, as the boundary velocity does not vary linearly in the entire range of driving force. The calculation of the velocity and mobility of interface migration with respect to different driving force region in Al-Mg alloy and comparison of that with pure Al will be described in the following section. The interaction of solutes with migrating grain boundary and its subsequent consequences will also be analyzed in detail.

### 3.5 Results and discussion

In this study, we employed the artificial driving force (ADF) method to drive the tilt grain boundary in a model Al-Mg system. In particular, we investigated the solute interaction with the migrating boundary and studied the solute pinning effect on the grain boundary motion in terms of mobility and interface restraining force in binary system compared to that of pure system. In ADF, an orientation dependent synthetic energy is added to one of the crystals and the boundary will start to move accordingly. As mentioned earlier, in this study we applied the potential energy to the second crystal of the Al-Mg binary system that shrinks over the course of simulation. The position of the migrating boundary was tracked by monitoring the entire potential energy (PE) of the system. In fact PE decreases with time as the interface moves, which is followed by a discontinuous drop in the energy profile referring to the completion of the transformation. The rate of change of potential energy with time was extracted to calculate the velocity of boundary migration following the equation:

$$v = \frac{\dot{E} \Omega_s}{A(E_2 - E_1)} \quad (3.7)$$

where  $\dot{E}$  refers to the rate of change of PE with time,  $\Omega_s$  is the temperature dependent atomic volume of the Al-Mg binary system,  $A$  is the interface area,  $E_2 - E_1$  corresponds to the potential energy difference between the shrinking and growing crystal, which is equivalent to the applied artificial driving force. The boundary mobility can be calculated from the slope of velocity vs. driving force plot.

In Fig. 3.5, the velocity of grain boundary migration is plotted vs. driving force at 300K for the  $7.785^\circ$  boundary in Al-2%Mg. The magnitudes of the velocity are the average of three separate MD runs and error bars denote the standard deviation. The

velocities are plotted only for that region of driving force at which the boundary was observed to migrate. As shown in the figure, there is a threshold driving force that is necessary to start the boundary migration. At all other applied forces, lower than the threshold value, the grain boundary did not move on an MD time scale. The lowest driving force, applied to observe boundary migration, is 0.05 eV/atom for Al-2%Mg binary system at 300K. Since this threshold is much higher than typical driving forces achieved experimentally, it appears that the presence of Mg atoms provides a significant barrier to the initiation of grain boundary movement. For comparison, in pure Al (see Section 2.7) the minimum and maximum driving pressures are just 0.0004 and 0.002 eV/atom respectively to observe the boundary migration. On a comparison of this study with classical impurity drag model by Cahn [38], it can be said that we can qualitatively simulate the high driving force regime of Cahn's treatment utilizing MD simulation. As there is no solid state diffusion in MD, we were not able to produce the low driving force part of Cahn's analysis.

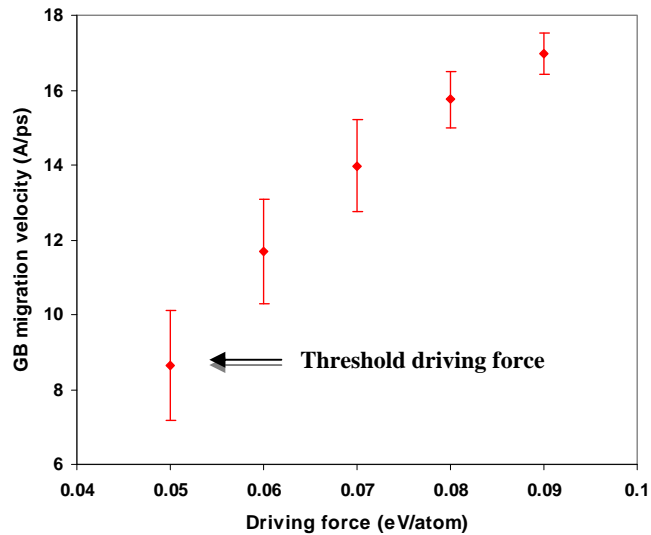


Fig. 3.5: Grain boundary velocity vs. applied driving force in high driving force limit for the  $7.785^\circ$  boundary in Al-2%Mg at 300K.

In Fig. 3.5, it is apparent that the velocity does not maintain a linear relationship with driving force at high applied pressure. The deviation from the linearity in the velocity vs. driving force plot was very obvious in the case of pure Al with the same Al inter-atomic potential. As mentioned in the previous chapter (Section 2.7), the proper grain boundary mobility depends on the careful selection of driving force regime. For the relevant low angle boundary mobility in pure Al, we have considered the very low driving force ( $\leq 0.002$  eV/atom) regime, which approaches the experimental range of applied pressure. The other reason of selecting the low driving force region is the different migration mechanism at different driving force region as discussed by Deng and Schuh [110]. For examining the grain boundary motion of similar mechanism, we

considered same driving force region as that of pure Al to compute the boundary migration velocity and eventually the mobility in Al-Mg binary system. Since the observed threshold driving pressure for Al-2%Mg is larger than the acceptable range for pure Al we are not able to report a reliable mobility for this composition and can only state that the addition of 2% Mg essentially pins the boundary at 300K.

To investigate the effect of different level of solute content on boundary motion, we extended our work by considering two other binary systems with 0.2% and 0.02%Mg. The objective of selecting the amount of solute was to study the interface migration in the similar applied force region for the alloys as that of pure system and eventually the effect of solute on the boundary velocity and mobility. In Fig. 3.6, we plotted the velocity of grain boundary migration vs. driving force for the  $7.785^\circ$  boundary in Al-0.2%Mg at 300K to compare the effect of 0.02%Mg on boundary velocity with that of 2%Mg. As shown in the figure, the threshold driving force for Al-0.2%Mg is 0.03 eV/atom, which is still higher than the experimental range of applied forces. Therefore it can be stated that, even with 0.2%Mg, we are observing a strong pinning barrier to the motion of the grain boundary. The non linear relationship of velocity with driving force is noticeable in Fig. 3.6. As we are not in the suitable range of driving force yet as that of pure Al, boundary mobility will not be reported for  $7.785^\circ$  boundary in Al0.2%Mg system at 300K.

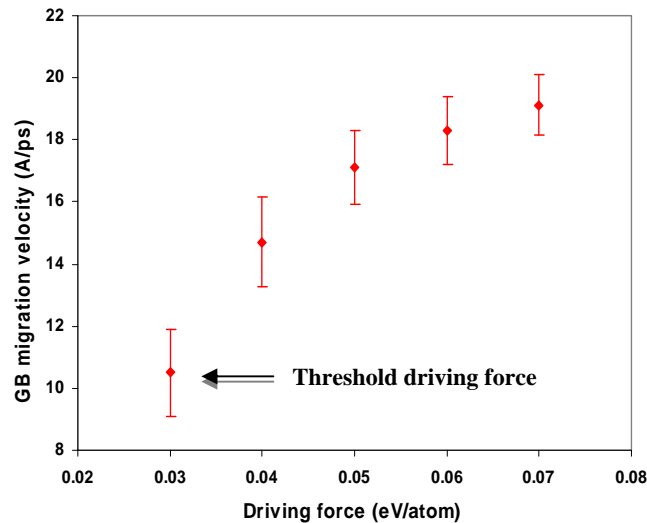


Fig. 3.6: GB velocity as a function of applied driving force in high driving force limit for the  $7.785^\circ$  boundary in Al-0.2%Mg at 300K.

In addition to binary systems with varying concentration, we also studied different alloy compositions as a function of misorientation. Besides  $7.785^\circ$  boundary, we employed three other boundaries with  $11.655^\circ$ ,  $17.408^\circ$  and  $23.07^\circ$ . A strong dependency of the solute content on threshold driving force is observed, which is summarized in Fig. 3.7 in terms of the threshold pressure for all binary alloys examined. In this figure, it is shown that at all misorientations the minimum applied force to start grain boundary

motion is much higher for every binary system and the pinning effect increases with increasing solute content. As in the case of Al with 2%Mg and 0.2%Mg, all other compositions studied also showed a threshold force that lies outside the regime of acceptably low driving forces and the mobility can not be stated with confidence. Therefore none of these compositions, at any misorientation, was considered for mobility determination to compare with that of pure Al.

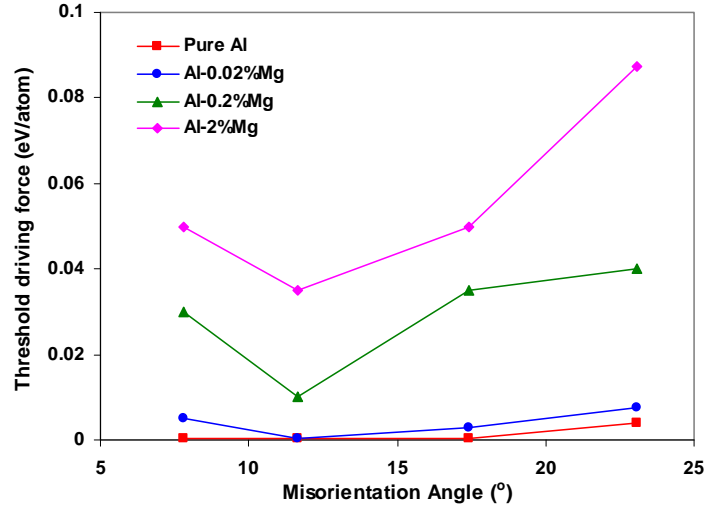


Fig. 3.7: Threshold driving force for all examined solute concentration, along with pure Al, as a function of boundary misorientation at 300K.

To study in detail the solute effect on the migrating boundary, the solute distribution across the boundary was examined. In Fig. 3.8, a simulation snapshot of the grain boundary region is shown, where the golden atoms are the solutes (Mg). As the initiation of the grain boundary is completely pinned by the solute atoms and the boundary remains stationary at low driving force, we focused on the interface regime to investigate closely the interaction of solutes with the boundary. To show the grain boundary region explicitly, only the interface portion is zoomed-in in the lower panel. It is clear from the figure that the number of solute atoms at the grain boundary is much higher than in the bulk crystal. The binary system is equilibrated in MC simulations and hence the solute atoms are considered to be in their preferred sites. The grain boundary collects a number of Mg atoms due to the strong interaction between the boundary and the solutes. As the low angle boundary consists an array of discrete dislocations, the solutes are observed to be positioned in the vicinity of each boundary forming dislocation. Therefore the Mg atoms are found to be clustered after every 5/6 atomic planes (equivalent to dislocation spacing) in the grain boundary. The presence of large number of solute atoms at the interface provides huge pinning effect on the motion of the low angle boundary, even on the starting of the boundary movement.

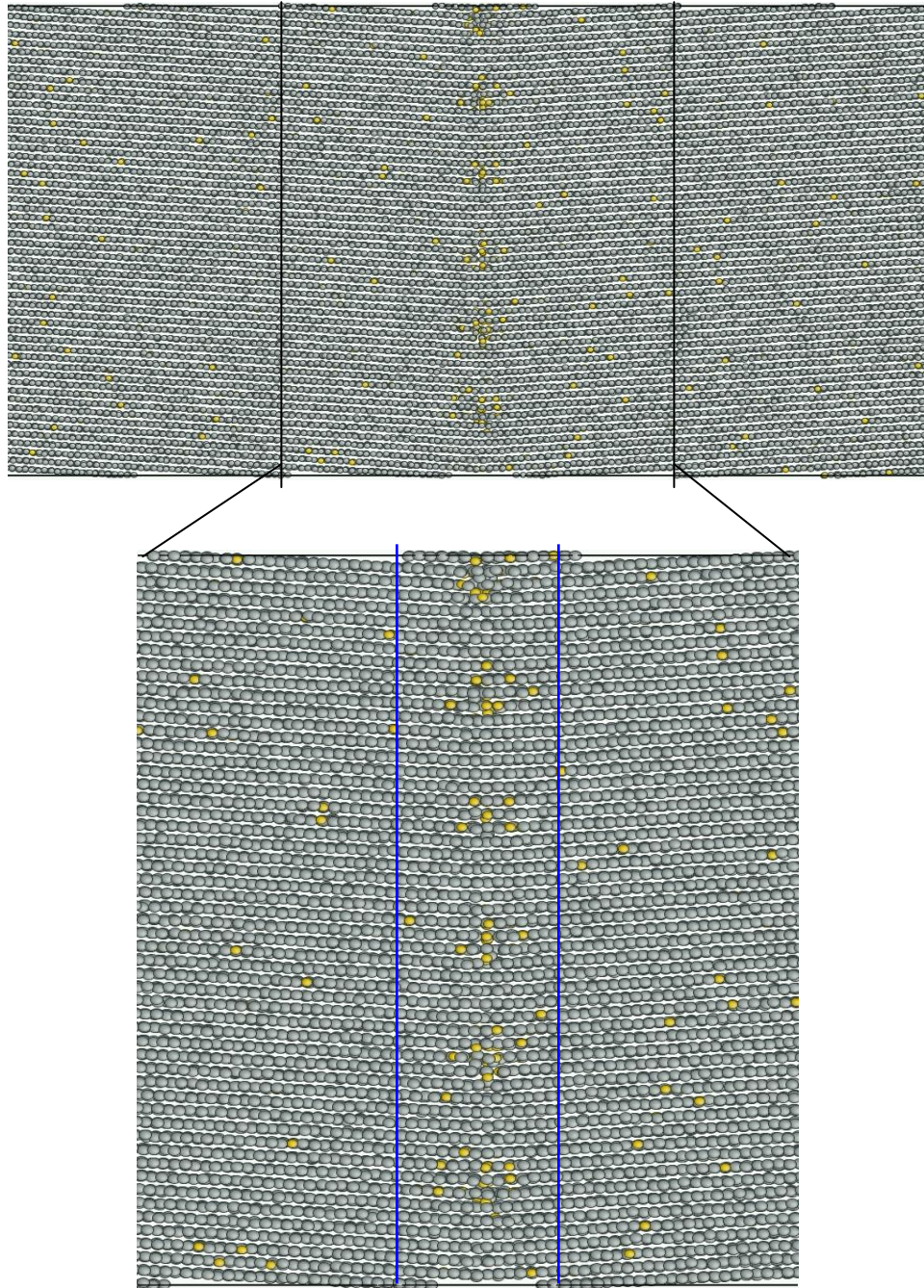


Fig. 3.8: Simulation snapshot showing the segregation of Mg atoms (golden color) at the grain boundary for Al2%Mg system for the  $7.785^\circ$  boundary at 300K.

In Fig. 3.9, the concentration of solute distributed in the Al-2%Mg alloy was plotted for the  $7.785^\circ$  boundary in the direction normal to the interface. To determine the concentration of Mg atoms, the entire binary system was divided into several bins in the

x-direction (normal to the GB). Each point in the figure refers to the average solute concentration in each bin. The peak at the centre of the plot of Fig. 3.9 corresponds to the concentration of solutes at the grain boundary region. That peak illustrated that the content of solutes segregated at the grain boundary, corresponds to 7.5at% solute, is too high in the MC equilibrated system. In particular, as shown in Fig. 3.8, the solutes clustered surrounding the intrinsic dislocations that form the grain boundary. The group of solute atoms at the grain boundary provides large restraining force on the initiation of boundary motion. This pinning force causes the mobility determining driving force to be shifted to a region of higher magnitude in Al-Mg binary alloys compared to that of pure Al.

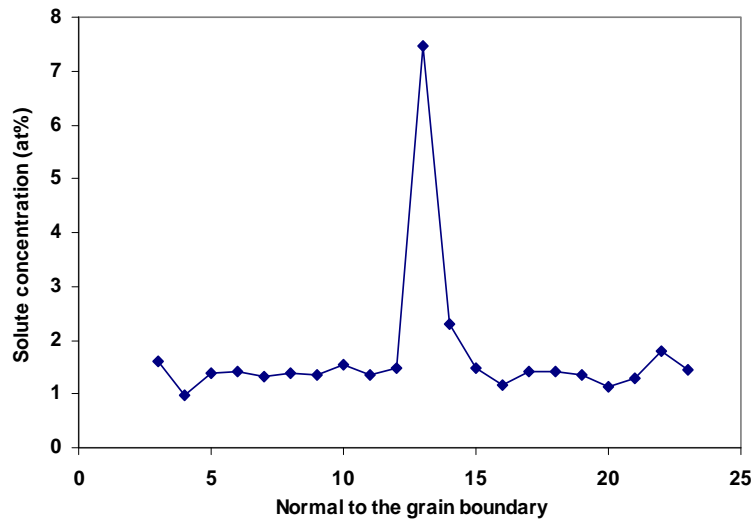


Fig. 3.9: The solute distribution profile the direction normal to the grain boundary for the  $7.785^\circ$  boundary in Al-2%Mg alloy at 300K.

Our observation is comparable to the work by Olmsted and Curtin [144], where they studied the mobility of dislocation in Al-Mg alloys and reported that dislocation motion is pinned due to the local solute atmosphere at low applied stress and this is more pronounced at lower temperature. The authors [144] reported a threshold stress of 0.15 MPa/K, equivalent to 0.005 eV/atom at 300K, in Al-2.5Mg alloy to illustrate the effect of pinning/depinning in dislocation motion. In comparison, we found a threshold driving pressure of 0.05 eV/atom for the motion of  $7.785^\circ$  boundary in Al-2%Mg at 300K. In comparison, our observed threshold pressure is 10 times of that reported by Olmsted. We can propose three fold reasons for this discrepancy: (1) we focused on the threshold force that completely pins the boundary, while Olmsted's study described the threshold stress at which the dislocation motion only slows down; (2) the intrinsic dislocations at the grain boundary are completely packed and the dislocation spacing is roughly 5 atomic planes in our study, while, the individual dislocations are randomly distributed in Ref. [144]; (3) finally, two different interatomic potentials has been employed in this and Olmsted study that can provide different effects. As we detected the clustering of solute atoms around

the intrinsic dislocations at grain boundary in our Al-Mg alloys, another relevant study of Olmsted et al. [145] have reported that Mg atoms in their Al-Mg system segregated above and below the slip plane due to high interaction energy and provide strong local pinning on dislocation movement, while no considerable restriction was observed by one or few solute atoms.

### 3.6 Distributed solute approach

The segregation of large number of solutes at the interface requires very high driving pressure to initiate the grain boundary migration in Al-Mg alloys at all composition and misorientation investigated. Complete pinning is observed even for the lowest concentration examined in the low driving force regime. Mobility in binary system, extracted in that applied force region, can not be compared with that of pure system due to different migration mechanism at higher driving force. However, we have employed another approach to study the solute interaction with migrating boundaries specifically in the limit of high driving force. The additional simulations again use SGCE-MC to place Mg in the simulation cell, but now the Mg additions are confined to a region away from the grain boundary and in the shrinking grain. That is there are no Mg atoms segregated at the grain boundary and at the surface. The procedure is illustrated in Fig. 3.10, which shows an equilibrated Al-2%Mg binary system containing a  $7.785^\circ$  boundary at 300K. In this figure, the golden color atoms are Mg and the rest are Al atoms. It is clear that grain boundary and surfaces do not have any Mg atoms and the solute atoms are distributed only in a certain region at the shrinking crystal (right) as indicated in the figure (for clarity, only the right half of the cell is shown in the lower panel). In the course of the simulations, the Mg atoms will act as evenly dispersed pinning sites for the migrating boundary during the shrinking of the solute containing crystal, but segregation of Mg to the individual dislocation cores was not allowed. In this approach, only the  $7.785^\circ$  boundary has been used at 300K for the binary systems of Al with 2%, 0.2%, 0.15%, 0.1% Mg.

Again the artificial driving force (ADF) method [79] was employed for the migration of the grain boundary and a wide range of driving forces was used to extract the boundary mobility. In Fig. 3.11, the change in PE/atom with time over the course of simulation for the  $7.785^\circ$  boundary in Al-2%Mg alloy at 300K is plotted where the applied driving force was 0.008 eV/atom. The continuous decrease in the PE corresponds to the migration of the grain boundary and the sudden drop at the end in the profile refers to the completion of the transformation. The figure clearly shows that there is a change in the slope of PE plot at around 10ps and this abrupt change corresponds to the point where the migrating boundary enters the region containing Mg solute. Since the slope decreases, it is obvious that the Mg atoms exert a pinning effect on the motion of the grain boundary.

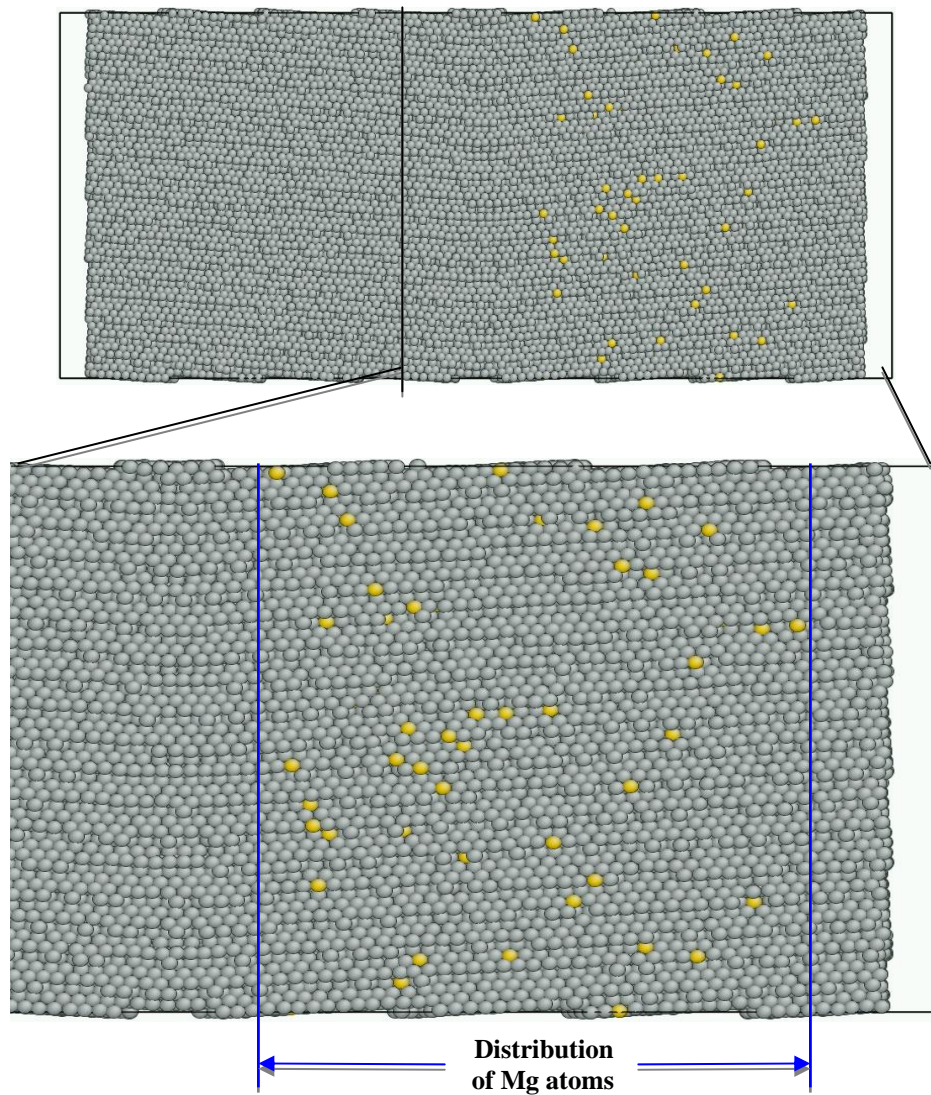


Fig. 3.10: The equilibrium Al-2%Mg binary system with  $7.785^\circ$  boundary at 300K. The lower panel clearly shows that Mg atoms are distributed in a confined region away from the grain boundary.

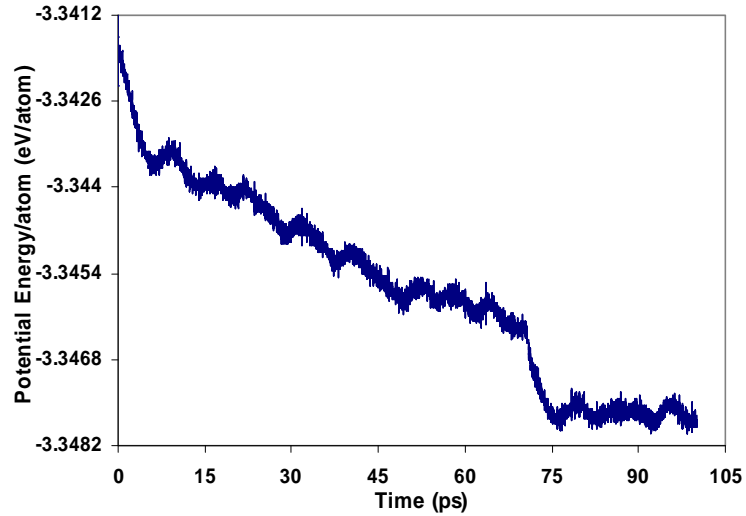


Fig. 3.11: PE/atom vs. time for the  $7.785^\circ$  boundary in Al-2%Mg alloy at 300K with 0.008 eV/atom applied driving force.

It is important to note that, there is still a threshold driving force for the  $7.785^\circ$  boundary in Al-2%Mg at 300K that was required to overcome the pinning barrier of the dispersed solutes. With the application of any driving force, which is below the threshold value, the boundary is completely pinned by the distributed Mg atoms in the binary system with 2% solute. The minimum driving force for depinning from the uniform solute field in Al-2%Mg was 0.006 eV/atom, which is much higher than the maximum applied force (0.002 eV/atom, see the previous chapter) in pure Al in the low driving force limit. That leads us to consider some other binary systems with lower solute concentration, such as Al with 0.2%, 0.15% and 0.1% Mg to compare the boundary mobility with that of pure Al. All of these alloys were constructed following the same procedure as Al-2%Mg.

A typical plot of velocity as a function of driving force is shown in Fig. 3.12 for the case of Al-0.2%Mg with the  $7.785^\circ$  boundary at 300K. For the boundary velocity, we have considered three different MD simulations and taken the average value and the standard deviation of those measures the error bars. It should be noted that in the case of pure Al, the upper limit of applied force for which a linear relationship between velocity and driving is observed was roughly 0.002 eV/atom. As can be seen in Fig. 3.12, the same range of driving forces can be examined for the alloy. The boundary velocities in the figure show a linear relationship and the solid line represents a fit to these points and the extension of this line passes through the origin. Therefore the velocity of grain boundary in Al-Mg binary systems measured from the selected driving force region can be utilized to analyze the effect of solute on the motion of  $7.785^\circ$  boundary at 300K. It was found that, in the case of Al with 0.15% and 0.1% Mg, the range of applied force, at which the boundary was observed to migrate, was similar to that of pure Al. To measure the solute pinning effect on the boundary motion, we calculated the velocity at all those

compositions in the acceptable driving force range by tracking the potential energy profile.

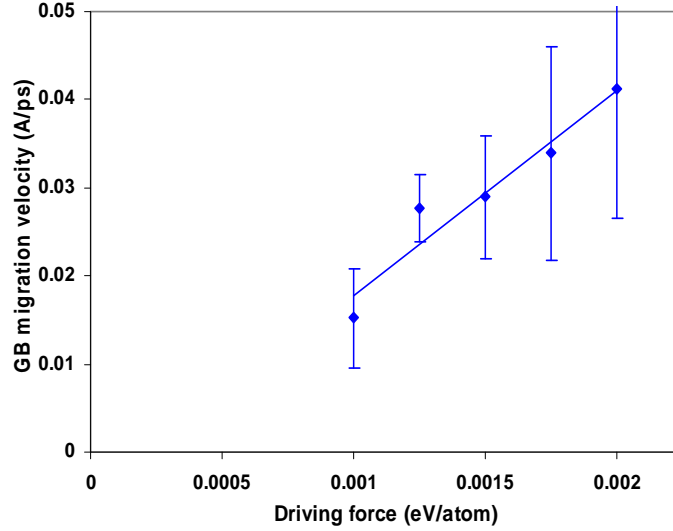


Fig. 3.12: GB velocity as a function of driving force for the  $7.785^\circ$  boundary in Al-0.2%Mg at 300K. The slope will almost pass through the origin.

### 3.7 Solute pinning constant measurement

In a recent study of the solute pinning effect on grain boundary migration, Hersent et al. [128] proposed that the boundary velocity in a solute containing system can be expressed as:

$$v = M \left( P - \frac{2\gamma_{gb}}{R} - P_C \right) \quad (3.8)$$

where,  $M$  is the characteristic boundary mobility in the pure material,  $P$  is the applied driving pressure and  $P_C$  refers to the restraining pressure on the migrating boundary resulting from solute additions. The second term on the right side in Eq. 3.7,  $\frac{2\gamma_{gb}}{R}$  takes into account the effect of grain boundary curvature, with  $R$  is the radius between the pinning points and  $\gamma_{gb}$  is the grain boundary excess free energy. In Hersent's analysis, the restraining pressure is described as  $P_C = F_C/A = F_C\lambda c_b n_b$ , where,  $F_C$  is the pinning force,  $\lambda$  is the boundary thickness,  $n_b$  is the number of atoms per unit volume inside the boundary and  $c_b$  is the boundary solute concentration. For high driving pressures/ low

solute concentrations, the boundary solute concentration ( $c_b$ ) is equivalent to the average solute concentration ( $c$ ). In our calculation, we will consider  $c_b \approx c$  and now the restraining pressure is  $P_C = F_C \lambda c n_b$ . If the boundary width ( $\lambda$ ) and  $n_b$  are assumed to be constant, we can define solute pinning constant  $\delta = F_C \lambda n_b$ . Therefore, as mentioned earlier, the restraining pressure  $P_C$ , being the effect of solute pinning, can be expressed in terms of solute concentration as  $P_C = \delta c$ .

In our study, we will employ the approach of solute pinning by Hercent [128] to analyze the solute behaviour on the migrating boundary. As planar boundary is considered in this investigation, the curvature effect term can be ignored from Eq. 3.7. Therefore, the effective relationship among boundary velocity, applied force and solute pinning force would become  $v = M(P - P_C)$ . Neglecting the curvature term and expressing the restraining pressure ( $P_C$ ) in terms of boundary solute concentration ( $c$ ) and solute pinning constant ( $\delta$ ), Eq. 3.7 can be rewritten as:

$$v - MP = -(M\delta)c \quad (3.9)$$

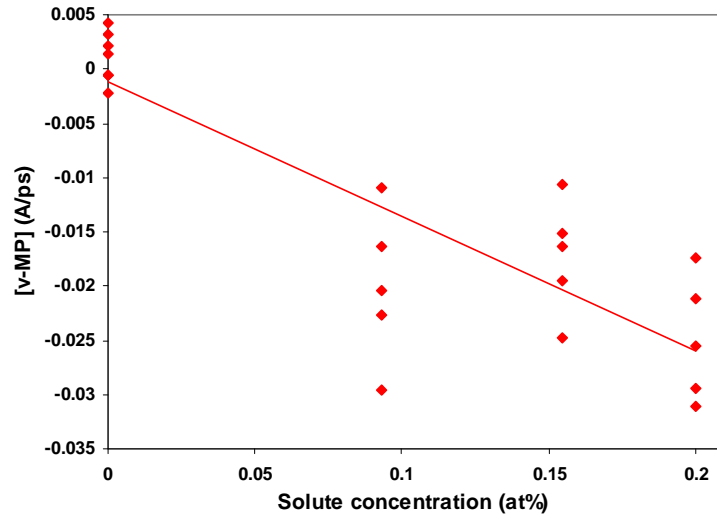


Fig. 3.13:  $(v - MP)$  as a function of solute concentration for binary systems: Al with 0.1%, 0.15% and 0.2% Mg and pure Al for the  $7.785^\circ$  boundary at 300K.

In Fig. 3.13, the term  $(v - MP)$  is plotted as a function of solute concentration for three different Al-Mg binary systems, such as Al with 0.1%, 0.15% and 0.2% Mg of  $7.785^\circ$  boundary at 300K. As the value of  $M$ , we used LAGB mobility for pure Al, which is  $37 \pm 8.2 \text{ \AA/ps/(eV/atom)}$  or equivalently  $3.9 (\pm 0.9) \times 10^{-7} \text{ m/s/Pa}$  as reported in the last chapter. Despite the large scatter in the data there is, consistent with the Hersent et. al.

model, a roughly linear relationship between the pinning force and the concentration. The solid line in Fig. 3.13 refers to the best linear fit to all the data points and approximately passes through the origin, corresponding to pure Al. The magnitude of the solute pinning constant  $\delta$  is extracted from the slope of the plot of Fig. 3.13. The magnitude of  $\delta$  is  $(3.34 \pm 0.94) \times 10^{-3}$  eV/atom or equivalently  $32.6 \pm 9.2$  MPa (with 95% confidence level) for the  $7.785^\circ$  boundary in the Al-Mg binary system at 300K.

For the migration of the  $7.785^\circ$  boundaries in Al-Mg alloys, the ADF method involves the calculation of the order parameter (OP) for each atom, including the Mg atoms. As the Mg atom is larger in size and it can strain the lattice substantially. Therefore the OP measurement may mis-read the Mg atoms and may cause the actual driving force to be less than the selected values. To test this possibility, we performed a careful study using the lambda integration technique [118] and corrected the driving force accordingly for all the alloys in Fig. 7. As the misoriented (shrinking) crystal only contains the Mg atoms, the lambda integration is applied to that crystal in the distributed solute systems and found, a small, roughly 2~5% variation in the results.

To verify the magnitude of threshold driving pressure we found in Al-2%Mg system for the  $7.785^\circ$  boundary at 300K in both cases of segregated and evenly distributed solutes, we have used the calculated value of solute pinning constant  $\delta$ . In the case of solute segregation at the grain boundary, it is reported and observed in Fig. 3.8 that the boundary contains 7.5at% Mg in Al-2%Mg. Therefore the pinning pressure for that solute concentration will be  $0.025 \pm 0.007$  eV/atom, which is comparable to the threshold driving pressure 0.05 eV/atom that is observed from our MD simulations for the  $7.785^\circ$  boundary. As reported earlier, we found a threshold pressure of 0.006 eV/atom for distributed solutes in Al-2%Mg at 300K. Using the value of  $\delta$ , the threshold pressure is  $0.007 \pm 0.002$  eV/atom for Al-2%Mg alloy, which is in close agreement with our MD results. Finally, it can be stated that we validated our investigation of MD simulation by comparing the observed threshold driving pressure for the migration of  $7.785^\circ$  boundary in Al-Mg binary system with that of calculated value from solute pinning constant at 300K.

It is worthwhile to state that we intended to perform the MD simulations of  $7.785^\circ$  boundary motion in the presence of solute Mg atoms in Al-Mg alloys at some higher temperatures in this study. In the previous chapter, it was reported that the artificial driving force (ADF) method is not effective to determine LAGB mobility at the temperatures 400K and 500K. The reason was attributed to the failure of order parameter measurement due to high thermal fluctuations in the range of those temperatures. Therefore, we could not employ the ADF technique at any temperature higher than 300K in this work to investigate the temperature dependence of solute pinning effect on the migrating LAGB in Al-Mg alloys.

### 3.8 Summary of the chapter

The reason of the existing discrepancies between computationally and experimentally determined grain boundary mobility is usually attributed to the presence of impurities in the real materials in experiments. It was reported in all studies that even small amount of solutes can retard the boundary motion strongly and result in lower magnitude of mobility. Solute retarding effect on grain boundary migration is rarely studied computationally. As molecular dynamics (MD) can derive intrinsic mobility, it can precisely predict the effects of solute on the mobility. In this chapter we investigated the solute pinning effect on the migrating grain boundary, especially LAGB, in a model Al-Mg binary system using MD simulations and the artificial driving force (ADF) method. The motion of [112] symmetric tilt boundaries are examined employing two different approaches for different misorientation at 300K. The binary bicrystal system with equilibrium composition profile showed solute segregation at the grain boundary that was found to provide a strong barrier to initiate the boundary migration. There is a threshold applied pressure that is required to overcome the strong pinning effect at all misorientation and concentration examined at 300K. It was observed that the threshold force was very high in the solute segregated case. Due to the absence of solid state diffusion, MD simulation could not reproduce the low driving force limit of Cahn's analysis and only captures the high applied force region. The application of very high pressure drives the grain boundary to migrate with a different mechanism compared to that of pure Al where low pressure is applied to move the boundary. Therefore, the boundary mobility computed for Al-Mg system at high applied force in the case of solute segregation can not be compared with that for pure Al.

An alternative approach, where solute atoms are distributed in a specific region away from the boundary, was employed to investigate the GB-solute interaction under applied pressure. The later technique provided less pinning effect on 7.785° boundary (LAGB) migration compared to that of segregated solutes. The solute restraining force is measured that shows a linear variation with concentration, which is in agreement with the relevant study by Hersent et al. Using the second method, the solute pinning constant is computed, which is  $\delta = 32.6 \pm 9.2$  MPa for LAGB in Al-Mg binary system at 300K. We found that our MD derived threshold driving pressure for the motion of 7.785° boundary agrees well with the calculated one using the value  $\delta$  at 300K.

## CHAPTER 4

### **Dislocation pinning effect on grain boundary migration**

In chapter 3, we have examined the solute pinning effect on the low angle grain boundary migration and found that solutes can strongly pin boundary motion and can reduce the associated mobility. The investigation in the last two chapters did not consider the effect of extrinsic dislocation on the boundary motion. It was mentioned in the first chapter that the interaction of network dislocations can retard the grain boundary mobility as well. To investigate that phenomenon, in this chapter we will study the low and high angle grain boundary motion in the presence of externally induced dislocations. We will perform the MD simulations utilizing artificial driving force (ADF) technique.

#### **4.1 Literature review**

Due to the significance of boundary motion, considerable attention has been paid to computations, simulations and measurements of grain boundary mobility. The real polycrystalline materials contain different types of defects, such as impurities, vacancies, network dislocations etc. These defects can provide influential role during microstructure development by affecting the motion of grain boundaries and accordingly control the mechanical properties of any material. Therefore the interaction of defects with the grain boundary is a subject of importance from the view point of both technologists and scientists. Although numerous studies have focussed on the role of solutes in the migration of grain boundaries, far less attention has been devoted to elucidating the role of network dislocations present in the grain interiors. Since these network dislocations can act as pinning sites for moving boundaries, a fundamental understanding of the interaction of dislocations with the grain boundaries is essential.

Because of the importance of grain boundary in controlling the microstructure of materials, numerous studies have been conducted to determine the boundary mobility. Various experimental measurements of boundary mobility has involved the use of special crystal geometry [65-68], application of external stress [71-72,12], utilization of capillary driving force [28,31] and magnetic field [69-70], tracking of triple junctions in annealing process [73] and so on (for a review, see Ref. [146] ). These methods of boundary mobility determination have been described in detail in the second chapter. As illustrated in the first chapter, in a study of particular interest and relevance to this work, Winning et

al. [12] measured the mobility of tilt boundaries in pure Al for a wide range of misorientation from a stress induced experiment and explained the importance of the interaction of extrinsic dislocations with the grain boundary. In that study, the large variation of the mobility with misorientation was described in terms of the qualitatively different behaviour of dislocation interaction with low angle and high angle boundaries. The authors illustrated that [100], [112] and [111] tilt boundaries were pinned by the network dislocations for the grain boundaries with low misorientation. In contrast, the high angle boundaries absorbed the dislocations during its migration. According to the Winning et. al. [12] model, the motion of a pinned low angle boundary is controlled by the climb of the network or boundary dislocations, which requires an activation energy roughly similar to bulk self diffusion. On the other hand the motion of high angle boundaries involves the climb of absorbed dislocations with an activation energy equal to the boundary diffusion. The difference in activation energies explains the dramatic difference in high and low angle boundary mobilities as a function of temperature. This phenomenon is schematically described in the first chapter in Fig. 1.6. This explanation of Winning is consistent with an earlier proposal by Viswanathan and Bauer [66] who observed an activation energy for the LAGBs in Cu that is consistent with dislocation climb and a much lower activation energy for the case of HAGBs compared to that of LAGBs, as shown in Fig. 4.1, and the transition was reported as  $9^{\circ}\sim 13^{\circ}$  misorientation. According to Winning, the activation energy of the high angle boundary motion is dominated by the diffusion along grain boundary, while the motion of low angle boundary is controlled by bulk diffusion. In this study, we will investigate the interaction of dislocation with the motion of low and high angle grain boundaries to qualitatively validate Winning's Model.

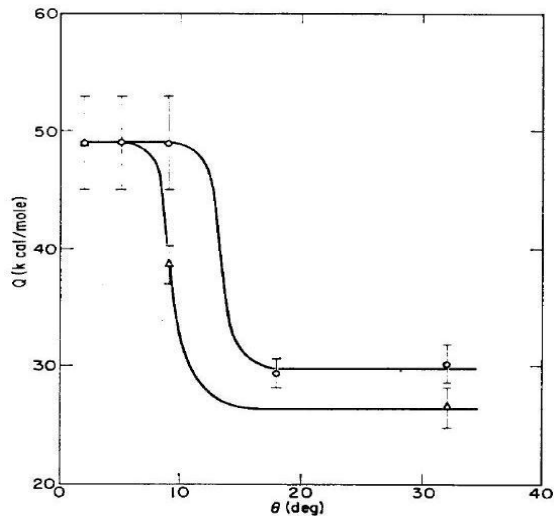


Fig. 4.1: Activation energy of grain boundaries as a function of misorientation for pure tilt (O) and mixed ( $\Delta$ ) boundary [66].

Besides experimental studies, over the past few years molecular dynamics (MD) simulation methods have emerged as an essential tool to compute grain boundary mobility in several model systems. In some MD techniques, the boundary migration is based on applied driving force, such as elastically driven [74-76], curvature driven [77-78,93] and artificial potential driven [79-81]. In recent years, two MD methods were developed that are based on equilibrium fluctuations of the interfaces and offer the distinct advantage of extracting the mobility in the limit of zero driving force. One technique [82-83] considers the 1-D random walk of the average displacement of grain boundary, while the other method [84] analyzes the total fluctuation spectrum of the interface. From all these previous studies it has been concluded that, MD derived grain boundary mobility is considerably higher than that of experiments. In addition all MD simulations consistently provide much smaller activation energies for boundary migration in comparison to those measured experimentally [74-75,77-78]. The reason of this discrepancy is usually attributed to the presence of impurities in real materials in the experimental measurements. As discussed in the third chapter, these impurities affect the interface kinetics by interacting with the migrating grain boundaries and even a trace amount of impurities can have a strong effect on the experimentally determined grain boundary mobility. In fact, several pioneering studies [32,37-38] and more recent works [61-64,147-148] have established the strong impurity drag effect on grain boundaries. As we report in the first chapter, there may be however an additional explanation for the discrepancy between experimentally measured and MD simulated grain boundary mobility. In any real metal there exists an array of network dislocations that, as discussed above, can interact with the moving boundary and eventually can provide drag or pinning effect on it. Therefore, it is of interest to investigate the interaction of extrinsic dislocations with the migrating grain boundaries using MD simulations. Since MD simulations of pure metals involved no solute additions whatsoever, the computations offer the advantage of isolating the dislocation-boundary interaction from all other competing interactions.

Despite the significance of dislocation-boundary interaction, there exist only few literatures that capture the effect of dislocation on the grain boundary kinetics. Over the decades, a number of investigations have been conducted to study the kinetics of discrete dislocation motion focusing the dislocation motion mechanism [149-150], the temperature and applied stress dependence of dislocation velocity [151-153], solute interaction with moving dislocations [144-145] etc. In 1988, Shen et al. [154] studied the interaction of dislocation with grain boundary in 304 stainless steel using electron microscopy. The authors reported that slip propagation of dislocation is obstructed by the grain boundaries and the impeding stress varies from 280 to 870 MPa depending on different mode of transmission. In 2003, in a computational study, dislocation interaction with grain boundaries in fcc metals has been examined by Koning et. al [155]. The authors studied GB-dislocation interactions utilizing 2D straining simulations in Al and 3D molecular dynamics simulations in Ni. The mechanisms of dislocation absorption, transmission and reflection have been described in terms of the interaction. In a recent study [156] Liu et. al. investigated the interaction of dislocation with low angle grain

boundary (LAGB) using discrete dislocation dynamics simulation. The authors studied the resistance of transmitted dislocations through the symmetrical tilt LAGB for different types of interaction between external and grain boundary dislocations such as collinear, coplanar, mixed-symmetrical junction etc.

In a study, particularly relevant to this work, Lim et. al. [157] studied the interaction of extrinsic dislocations with stress induced symmetric tilt low angle grain boundary (LAGB) motion. The grain boundary structure of their simulation is shown in Fig. 4.2. The intrinsic dislocations the form the LAGB have Burgers vector  $\mathbf{b}_1$ , while it is  $\mathbf{b}_2$  for the extrinsic dislocations. It was reported that the dislocation acts as pinning site for boundary migration and completely pins the LAGB motion below a critical applied stress with no dislocation climb. When climb of dislocation is allowed at low driving force, LAGB mobility can be determined from the linear variation of boundary with applied stress. The authors also calculated the forces between the dislocations and analyzed the LAGB mobility and threshold stress to escape from the pinning effect of extrinsic dislocations. From the point of view of the present work, MD simulations offer a comparison and confirmation of the continuum level computations of the motion and interaction of dislocations and grain boundaries.

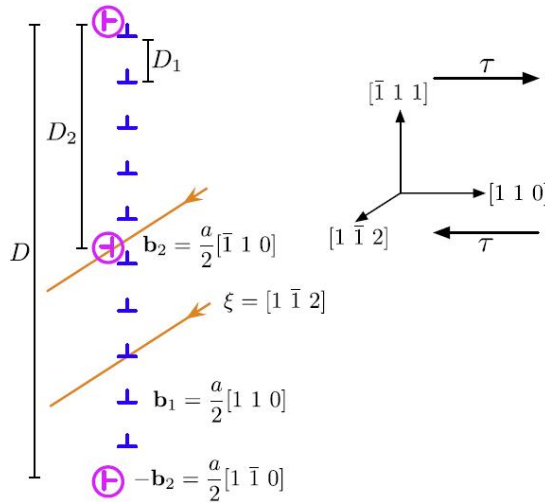


Fig. 4.2: Schematic view of the dislocation arrangement at the LAGB in Lim's study, where intrinsic dislocations are shown in blue with Burgers vector  $\mathbf{b}_1$  and extrinsic dislocations are pink with Burgers vector  $\mathbf{b}_2$  [157].

In the present study, we will investigate the interaction of extrinsic dislocation with migrating low and high angle grain boundary in pure aluminum employing MD simulations, where the boundaries are driven using the artificial driving force technique. We have used [112] symmetric tilt boundary in an embedded atom method EAM description [111] of pure Al. In particular we will focus on both the quantitative and qualitative differences, if any, between the dislocation-boundary interaction for low and high angle boundaries and the results will be discussed in terms of the proposed model by

Winning et. al. [12]. In the next section, the numerical procedure will be described including simulation geometry, dislocation structure and application of driving forces. In the following section, the simulation results will be discussed and the interaction of dislocation with grain boundary will be analyzed in detail.

## 4.2 Simulation Procedure

We have been using the same interatomic potential to define the atomic interactions throughout the entire thesis work which is given by an EAM description of pure Al system, developed by Mendeleev et. al. [111]. In this study, a bicrystal pure Al system, with incorporated external dislocations, is employed to investigate the interaction behaviour of dislocation with the migrating boundary of different misorientation. The simulations have been started with the grain boundary systems that are described in detail in the second chapter. To summarize, we have generated a [112] symmetric tilt grain boundary in pure Al for both low and high angle cases at 300K. The bicrystal system used was comprised of two adjacent grains and the misorientation is specified by the angular difference that these two differently oriented grains possess at the interface. The low angle boundary was created with  $7.785^\circ$  misorientation, while the high angle boundary corresponds to  $23.07^\circ$  misorientation. We have directly used the same simulation geometry and size as described in chapter–2 as the initial system of this study for both low and high angle cases. The simulation cell was periodic in the plane of grain boundary with two added free surfaces on both sides of the cell in the direction normal to the grain boundary. The free surfaces circumvented the developed stress with boundary migration due to coupled shear motion as discussed by Cahn and Mishin [107].

The network dislocations, which act as the pinning center during the simulation, were created into the simulation cell by removing some portion of a (111) plane of the system. The network dislocation pair was introduced into the grain that is consumed during the artificial driving force simulation. The bi-crystal slab was established with two edge dislocations of opposite Burgers vector for both misorientations. A snapshot of the high angle grain boundary (HAGB) simulation cell at 300K, misoriented by  $23.07^\circ$ , is shown in Fig. 4.3 and the extrinsic dislocation pair is visible in the top right region of the system. After creating dislocations, the whole system was relaxed to its equilibrium position utilizing an NVT (constant number of atoms, volume and temperature) ensemble. The steady state variation of the energy and pressure of the system confirms that the

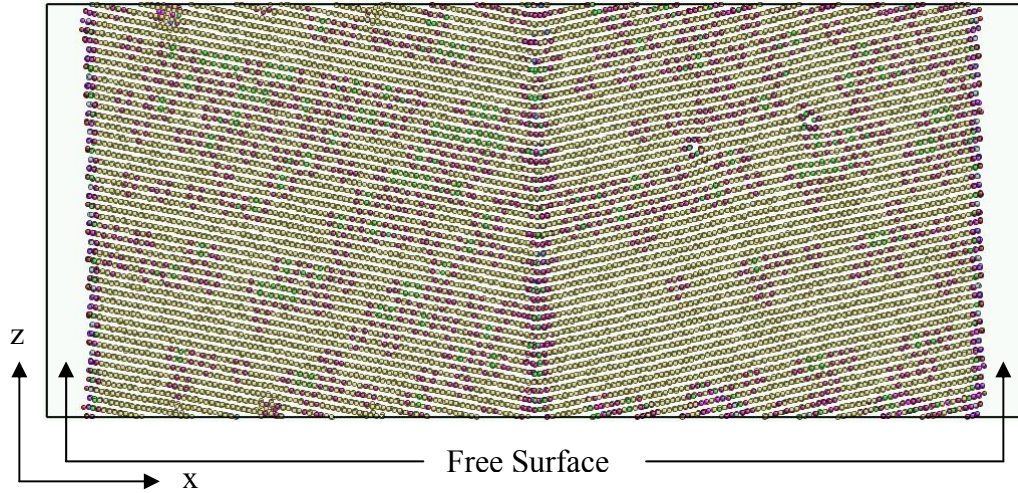


Fig. 4.3: Bicrystal simulation system of pure Al with  $[112]$  symmetric tilt  $23.07^\circ$  boundary at 300K. It is clear that the right crystal contains two dislocations and there are free surfaces at both ends.

equilibrium is obtained. We have used LAMMPS (Large-scale Atomic/Molecular Massively Parallel Simulator) code [114-115] to perform the MD simulations in this study. A time step of 1 fs has been used throughout. The well equilibrated system was then utilized to apply the driving forces for boundary motion and study the interaction of dislocations with the migrating boundary.

The two externally induced dislocations have opposite Burgers vectors leading to a zero net Burger vector. The extrinsic dislocations do not have any contribution to the angular difference between two crystals at their grain boundary. The structure of low angle grain boundaries consists of array of discrete lattice dislocations that will be named as intrinsic dislocation hereafter. The extrinsic dislocations, created in the system, possess line direction parallel to those intrinsic dislocations that form the grain boundary, but different Burgers vectors. The Burgers vector of the dislocations forming the boundary is  $\mathbf{b}_1 = \frac{a}{2}[1\bar{1}1]$  ( $a$  being the lattice parameter of the fcc crystal), while for extrinsic dislocations, these are  $\mathbf{b}_2 = \pm \frac{a}{2}[\bar{1}10]$ . Both types of dislocations have same line directions,  $\zeta = [\bar{1}12]$ .

### 4.3 Application of artificial driving force technique

To observe the grain boundary migration and eventually the interaction with extrinsic dislocations, a driving force is applied on the equilibrated grain boundary system following artificial driving force (ADF) technique [79]. In this method, orientation

dependent artificial potential energy is added to one of the grains in bi-crystal geometry. We have discussed the ADF method thoroughly in the second chapter, to get more detail see Ref. [79]. An order parameter (OP) measurement has been utilized to identify an atom as belonging to grain I or grain II in the bicrystal system. As described in Section 2.7, OP is calculated from the position of the nearest neighbour atoms following Eq. 2.5. The OP profile is shown in Fig. 2.25 that illustrates that the oriented crystal provides higher value of OP compared to that of the reference crystal. The misoriented grain shows a jump in the OP profile because of the deviation of atoms from its ideal position. The atoms in between these two extreme are considered to be in the region of grain boundary, where the driving force is applied due to the added potential energy in the ADF method.

In this technique, OP cut off values have been used to assign the atoms in different crystal and the synthetic potential energy is added accordingly. When the OP is lower than  $OP_{low}$ , the atoms are in the reference crystal with zero added energy. In contrast, for the atoms in the misoriented grain, OP is higher than  $OP_{high}$ , where the artificial energy is applied. The atoms with  $OP_{low} < OP < OP_{high}$  obtained an added energy as described in Eq. 2.7. This is shown in Fig. 2.26, where the slope of applied potential energy profile in the interface region determines the force that will drive the grain boundary. The application of artificial force requires the proper orientation of the nearest neighbour atoms in fcc system. The orientation of the atoms was introduced using the rotation matrix for both crystals as summarized in Table 2.1. We applied the artificial driving pressure to the misoriented grain that causes shrinking of this grain and growth of the reference grain through the migration of the boundary. As the misoriented grain contains the externally introduced dislocations, the grain boundary will move through the dislocations and the migrating interface interacted with the network dislocation during its motion. The GB–dislocation interaction behaviour was investigated for low and high angle boundary to differentiate their interaction behaviour in pure Al system at 300K. To investigate the interaction of extrinsic dislocation with the migrating boundaries in pure Al, a wide range of driving force has been applied at 300K. The span of driving force was 0.002 – 0.05 eV/atom for  $7.785^\circ$  boundary and 0.002 – 0.015 eV/atom for  $23.07^\circ$  boundary. The entire process of simulation was performed with an NVT thermostat.

#### 4.4 Results

To examine the dislocation effect on the migrating LAGB, the interface motion was monitored by tracking the change in the potential energy (PE) of the entire system with the simulation time. A plot of PE/atom vs. time at 300K is shown in Fig. 4.4 for the  $7.785^\circ$  boundary where an 0.002 eV/atom driving force is applied on LAGB. The plot exhibits a decrease in potential energy with time, followed by very long steady state in the profile. The decrease in PE corresponds to the migration of the grain boundary and the steady state part refers to the fact that the boundary is stopped in the MD time scale. It

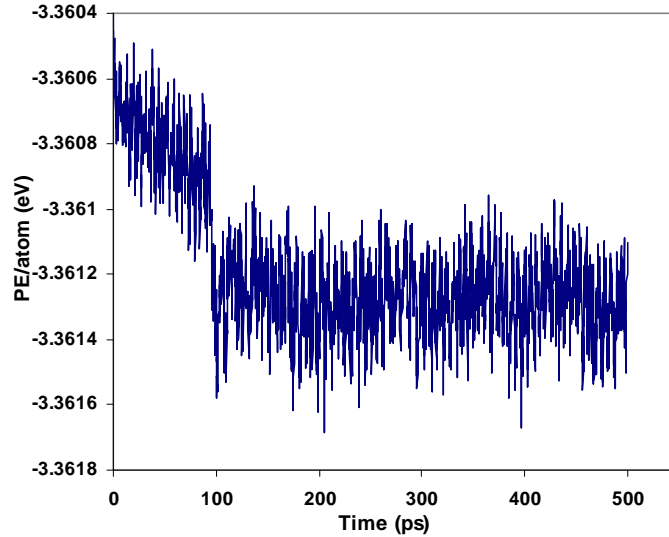


Fig. 4.4: Potential energy change with time under the application of 0.002 eV/atom driving force on  $7.785^\circ$  boundary. The steady state part corresponds to the complete pinning of the boundary.

should be noted that the low driving force regime in the MD simulations utilizes stresses that are larger than, but approach, those applied in the experimental studies of the boundary motion. Therefore, it can be stated that, in the absence of climb effects, the motion of the grain boundary is completely pinned due to the presence of the network dislocations.

The atomic description of the interaction of extrinsic dislocation with the migrating grain boundary of  $7.785^\circ$  misorientation is illustrated in Fig. 4.5 for the case of low driving force at  $T=300\text{K}$ . This figure captures some snapshots, magnified from the region containing the extrinsic dislocations, that illustrate entire process of interaction. Our MD study shows that the interaction of the edge dislocation with the migrating LAGB leads to gliding of the dislocation. This observation is exhibited step by step in Fig. 4.5. Fig. 4.5(a) shows the snapshot at the instant when the grain boundary has just started to interact with the dislocation. As shown in Figs. 4.5(b) and 4.5(c) immediately after encountering the boundary the dislocation glides rapidly downward. The process of gliding was found to be completed in Fig. 4.5(d) after 5.4 ps of interaction with respect to the figure at  $t = 0$  ps and it should be noted that the dislocation has glided a distance equivalent to the spacing of the intrinsic dislocations that comprise the LAGB.

As shown by the red line in Fig. 4.5(d), the final configuration of the system consists of a bowed out boundary pinned by the network dislocation. The locally bowed configuration of the boundary is due to the competition between the applied driving stress and the elastic interaction of the intrinsic dislocations with the single remaining network dislocation, both of which tend to force the boundary to the right in Fig. 4.5(d), and the

pinning effect of the leading extrinsic dislocation. The pinning of low angle boundaries by network dislocations, assuming a zero climb mobility, was also observed in the continuum simulations performed by Lim et. al. [157]. Also consistent with the above MD results, the authors demonstrated that the network dislocation, whose Burgers is perpendicular to the intrinsic grain boundary dislocations, glides prior to the pinning event. The MD simulations cannot account for dislocation climb, but the Lim et. al. study demonstrated that the LAGB will migrate, with the dislocation dragged by the moving boundary, when climb is included in the computation. The driving force required to move the boundary in the climb case is less than the threshold applied stress in the climb free case.

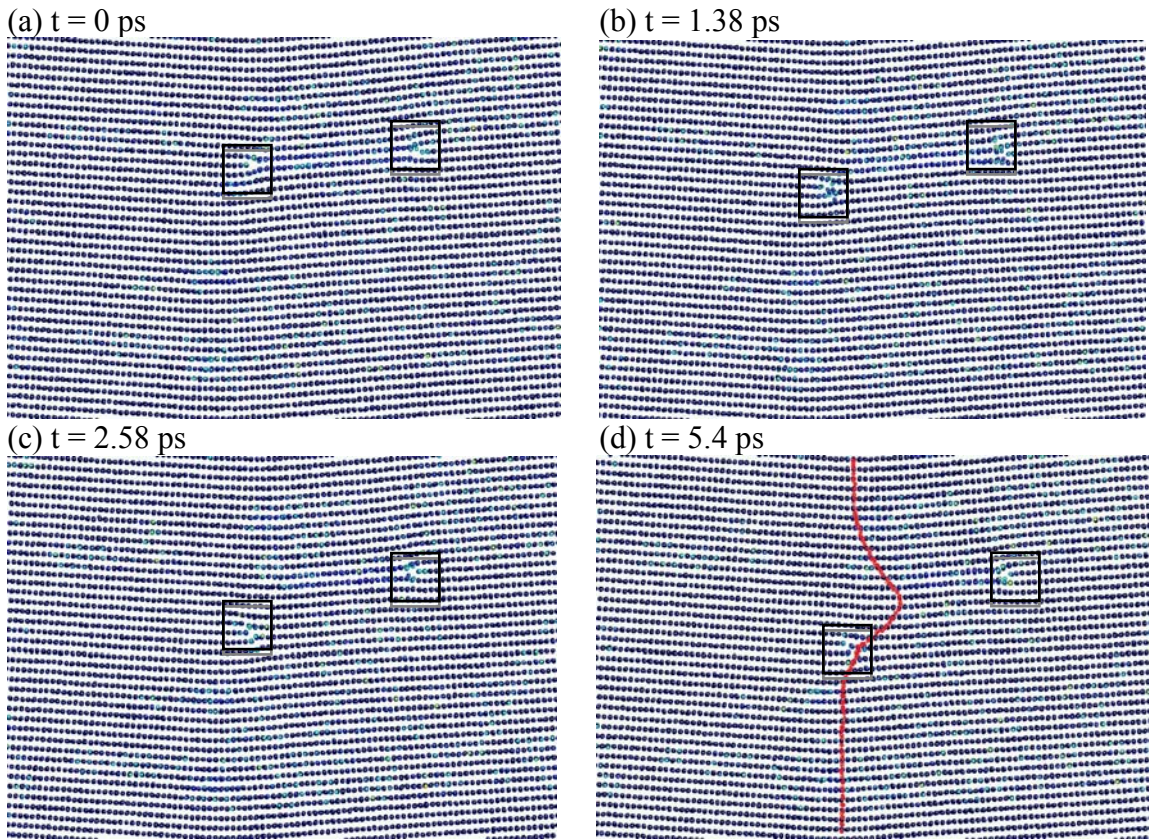


Fig. 4.5: Gliding of extrinsic dislocation due to the interaction with  $7.785^\circ$  boundary with the application of  $0.002$  eV/atom. The square boxes are showing the position of the extrinsic dislocations.

With the application of a sufficiently high driving ( $\geq 0.009$  eV/atom) the  $7.785^\circ$  grain boundary is no longer pinned by the extrinsic dislocation. Although the driving force is much higher than those attained in any experiment, it is nevertheless of interest to examine the atomic processes taking place during the boundary-dislocation interaction. As illustrated in Fig. 4.6(a) the leading extrinsic dislocation in the dipole pair once again glides downward when first encountering the migrating boundary. However, in the high

driving force case the boundary now moves past the dislocation and the LAGB then interacts with the trailing dislocation (Fig. 4.6(b)). Once again the extrinsic dislocation glides in the downward direction as shown in panel 4.6(c), but in addition the second dislocation has translated in a direction perpendicular to the LAGB plane. The net result is a complete annihilation of the dipole pair as the boundary passes (panel 4.6(d)). It is interesting to note that the high driving force applied to the system has induced a climb motion on the trailing extrinsic dislocation. Recall the dislocation dipole was created by removing some number of atoms from a (111) plane in the shrinking grain. After the process depicted in Fig. 4.6 is complete extra vacancies must necessarily be distributed throughout the system. It was found that the vacancies are pushed with the boundary, after annihilation of the extrinsic dislocations, and deposited at the end of the simulation structure.

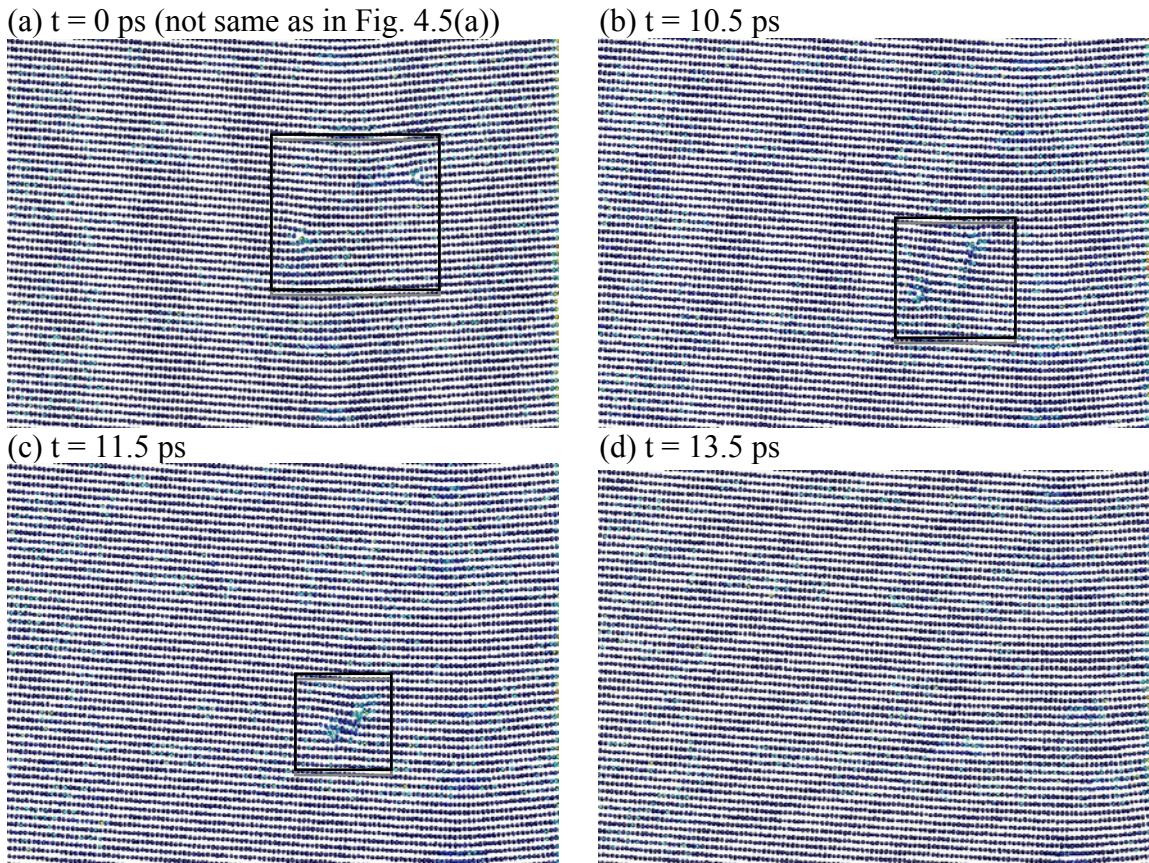


Fig. 4.6: Annihilation of extrinsic dislocation due to the interaction with  $7.785^\circ$  boundary with the application of  $0.01$  eV/atom. The square boxes are showing the position of the extrinsic dislocations.

A similar phenomenon has also been observed in the study by Lim et. al. [157] and the event is illustrated in Fig. 4.7. The authors have shown that, when the applied stress is higher than the threshold value, at  $t = 30000$ , the LAGB breaks away from the

pinning of extrinsic dislocation networks. Escaping of low angle boundary results in gliding of dislocations towards each other to be annihilated as observed in our simulation. The glide of dislocation in Lim's study is shown with red arrow in Fig. 4.7.

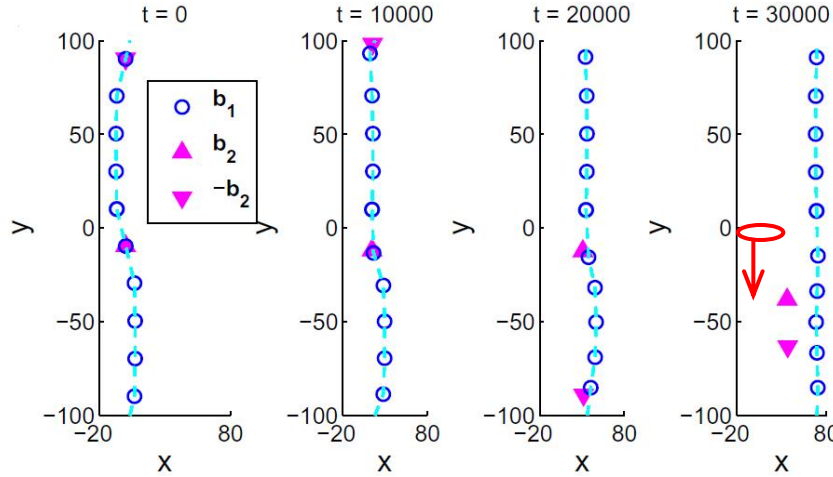


Fig. 4.7: Motion of LAGB to the right in Lim's study with the application of stress higher than threshold stress. Gliding of extrinsic dislocations towards each other (shown in red) at  $t = 30000$  that leads to annihilation of those dislocations [157].

As alluded to above, the Winning et. al. [12] experimental study reported very different behaviour for the boundary mobility for the LAGB and HAGB case and the authors attributed the difference to the interaction of the boundary with network dislocations. Therefore we have extended the MD simulations to the case of a high angle [112] tilt boundary with a misorientation of  $23.07^\circ$ . Again the grain boundary motion was induced via the artificial driving force technique and the temperature was 300K. The range of driving forces for the high angle boundary case was 0.002 – 0.015 eV/atom. The boundary-dislocation interaction for the low driving force limit is summarized in Fig. 4.8.

Panel 4.8(a) shows the system at a point in time where the boundary is far from the extrinsic dislocations and the right panel, 4.8(b), represents the final configuration. The simulation was run for additional 0.75 ns beyond the point shown in Fig. 4.8(b) and no additional grain boundary motion was detected. In other words the boundary has been pinned by the network dislocation. Also consistent with the  $7.785^\circ$  boundary, the leading extrinsic dislocation has undergone glide, but in this case the distance of glide is roughly one atomic plane, which is consistent with the spacing of the intrinsic dislocations comprising the HAGB. Therefore in both the high and low angle case the glide occurs over a distance corresponding to the spacing of boundary dislocations. However, it is important to note that there is no qualitative difference between the pinned boundary structure for the high and low misorientations.

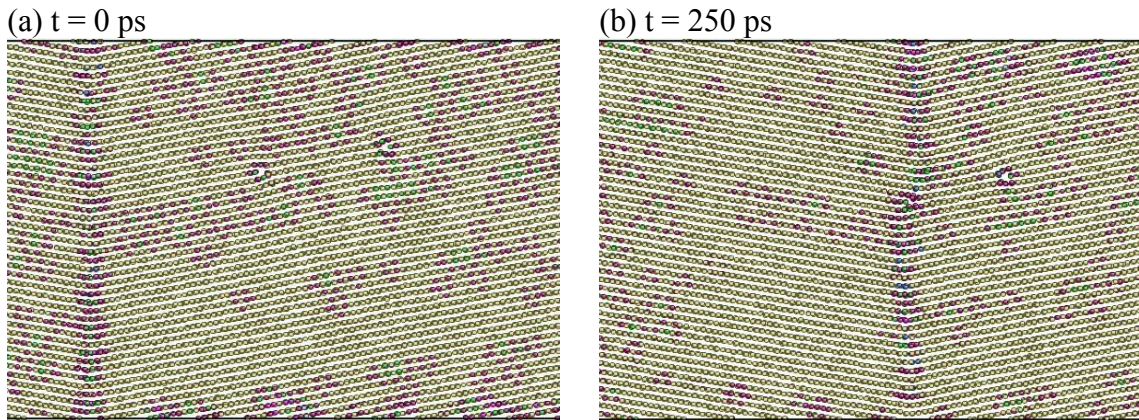
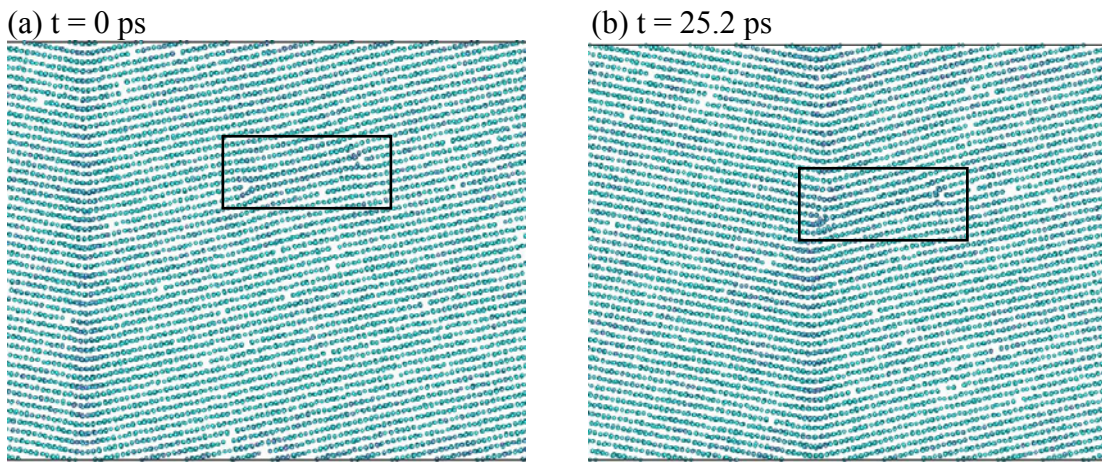


Fig. 4.8: Pinning of  $23.07^\circ$  boundary and gliding of extrinsic dislocation with the application of  $0.005$  eV/atom.

As reported earlier for the  $7.785^\circ$  boundary, there is also a threshold driving force for the  $23.07^\circ$  misorientation above which the network dislocation no longer pins the boundary. For HAGB, the critical driving force was found to be  $0.01$  eV/atom. At this very high driving force, the grain boundary migrates very rapidly and is transmitted through the dislocations. The dislocations then annihilate each other. The process is very similar to that observed for the LAGB. The atomic events that take place during the migration of HAGB with the application of high driving force,  $0.015$  eV/atom, at  $300\text{K}$  is described in Fig. 4.9. The initiation grain boundary migration under application of high applied force is shown in Fig. 4.9(a). The interaction of HAGB with first dislocation in Fig. 4.9(b) causes glide of that by about one atomic plane as shown in Fig. 4.9(c). The high angle boundary transmitted through the both dislocations in Fig. 4.9(d) and left behind them. The dislocations are gliding in the direction to each other for annihilation in Fig. 4.9(e) and the process is done in Fig. 4.9(f). Then the HAGB boundary migrates very fast and completed the transformation.



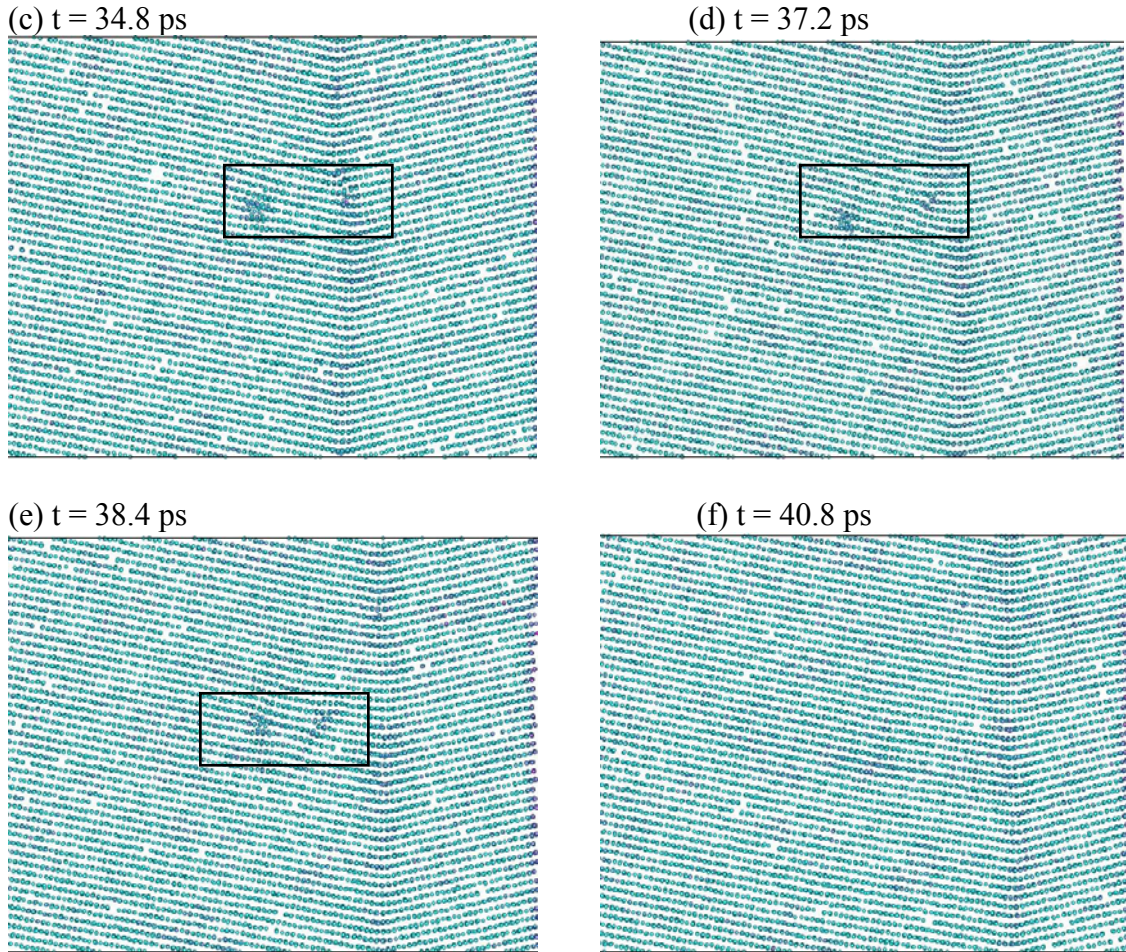


Fig. 4.9: Annihilation of extrinsic dislocation due to the interaction with  $23.07^\circ$  boundary with the application of  $0.015$  eV/atom. The boxes are showing the position of the extrinsic dislocations.

In summary, we observe a threshold driving force of  $0.009$  eV/atom for the low angle boundary and  $0.01$  eV/atom for the high angle boundary. At first glance this result appears to contradict the continuum results of Lim et. al. [157], who observed a threshold pressure that decreases with increasing misorientation. However, in the chapter of LAGB determination, it was illustrated that in ADF method there is a driving force barrier of approximately  $0.004$  eV/atom, at  $300\text{K}$  in pure Al, that must be overcome to start the motion of the  $23.07^\circ$  boundary. Therefore the effective pinning force barrier by the network dislocations is  $0.006$  eV/atom on the HAGB at  $300\text{K}$ . On the contrary, the barrier to motion was absent, within numerical uncertainty, in the case of the LAGB. As a result, the actual resistance on the grain boundary motion, exerted by extrinsic dislocation, is higher, by  $0.003$  eV/atom, for LAGB migration compared to that of HAGB, which is consistent with previous predictions by Lim et. al. [157].

As mentioned earlier, in a study relevant to this work, Winning et al. [67] examined the boundary mobility of both LAGBs and HAGBs in pure aluminum. The authors reported that, at low temperature, the LAGB provides lower mobility compared to that of HAGB and there is an abrupt change of roughly two orders of magnitude at  $\theta = 13.6^\circ$ . The trend is similar for [111], [112] and [100] tilt boundaries. It was also found that the trend is reversed at higher temperatures, that is, the LAGB has much higher mobility than HAGBs. The temperature dependence leads the authors to conclude that the diffusion mechanism responsible for the climb of pinned network dislocations differs for low angle and high angle boundaries. In the low angle regime bulk diffusion is the controlling mechanism whereas diffusion along the boundary is operative for the HAGB. In our work we have observed that there is no qualitative difference between the dislocation-boundary interaction for the  $7.785^\circ$  and  $23.07^\circ$  boundaries and there is therefore no obvious structural difference in the pinned boundaries that would suggest a different diffusion mechanism. Thus, the Winning model together with the MD results suggest that bulk vs. boundary diffusion behaviour is governed entirely by the spacing of intrinsic dislocations in the grain boundary. As will be discussed below, the results from several previous diffusion experiments support this view.

## 4.5 Discussion

The precise difference in the structure of low angle and high angle grain boundary is illustrated in Fig. 4.10. Fig. 4.10(a) refers to the boundary with  $7.785^\circ$  misorientation and Fig. 4.10(b) corresponds to the  $23.07^\circ$  boundary. In this figure, x-z plane of the simulation geometry is shown based on the potential energy (PE) of each atom. The x-axis and y-axis of the figure refers to the x and z coordinates, respectively, of the system in angstrom and PE is shown in eV/atom. The intrinsic dislocations that form the grain boundary are shown with red/yellowish color, while, the bulk is shown in purple. It is clear in Fig. 4.10(a) that the intrinsic dislocations are widely separated from each other in  $7.785^\circ$  boundary and the LAGB is, in fact, comprised of an array of such discrete dislocations. In contrast, in the case of  $23.07^\circ$  boundary in Fig. 4.10(b), there is an overlapping of the strain field of the intrinsic dislocations. Due to the closely spaced boundary forming dislocations, the migration of HAGB is mainly governed by the diffusion along the grain boundary. Therefore, the grain boundary diffusion is directly linked to the motion of low and high angle boundary.

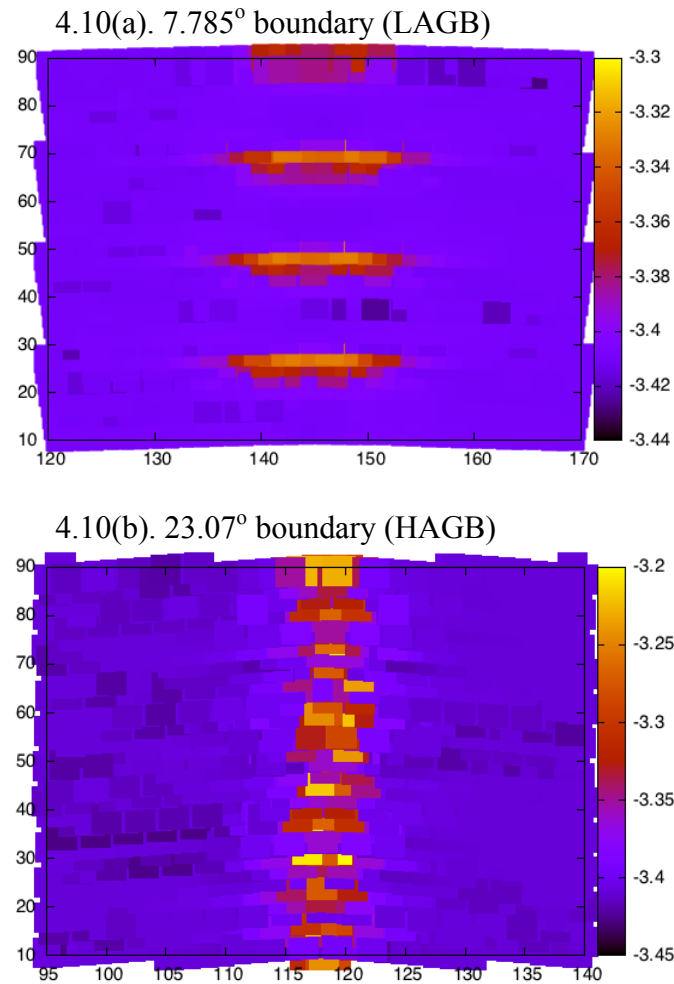


Fig. 4.10: Spatial arrangement of the intrinsic dislocations is shown based on the PE/atom for (a)  $7.785^\circ$  and (b)  $23.07^\circ$  boundary.

If the transition from bulk to boundary controlled climb is not directly related to the dislocation pinning/absorption process, then a similar transition should be observed in conventional solute diffusion as well. In an experimental investigation by Beke et al. [158-159], the activation energy ( $Q$ ) of grain boundary diffusion was reported for both sub grain boundary and high angle boundaries during the diffusion of electroplated Fe in >99.99% pure polycrystalline Al. The Arrhenius plot of grain boundary diffusion from their study is shown in Fig. 4.11, where GB diffusion coefficient is plotted with inverse temperature for both sub grain boundary and high angle grain boundary. The authors reported  $Q$  for LAGBs and HAGBs as about 147.6 and 95.18 KJ/mol respectively, a trend which is consistent with the findings of Winning et. al. [12], where  $Q$  for low and high angle boundary migration is reported as roughly 127 and 80 KJ/mol respectively. The Beke et. al. study predicts approximately  $T = 784\text{K}$  as the crossover temperature. In the Winning et al. study the crossover from bulk to boundary diffusion control was found to

take place in the range  $400\text{K} < T < 900\text{K}$ . Therefore, Beke et. al. study is in agreement with the range reported by Winning et. al.

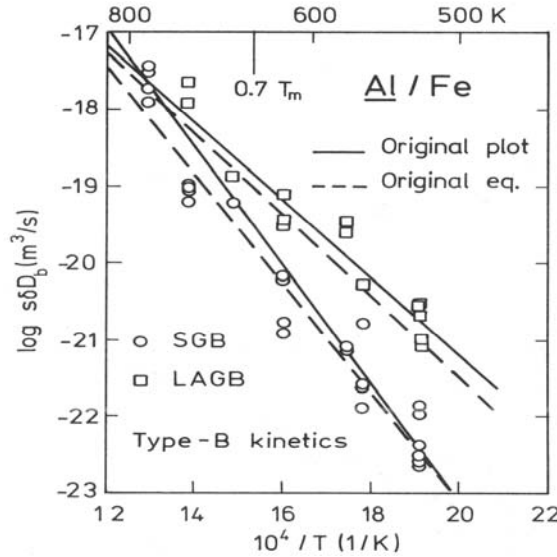


Fig. 4.11: Arrhenious plot of grain boundary diffusion coefficient with inverse temperature for both sub grain boundary and high angle grain boundary [158].

Grain boundary diffusion data was also found to agree qualitatively with Winning et al. study in a recent experimental study by Fujita et. al. [160], where the authors evaluated the diffusion characteristics in samples of Al-Mg and Al-Zn alloys specially processed to contain varying fractions of low angle boundaries. The authors concluded that the activation energy of diffusion is higher for LAGBs compared to that of HAGBs and the intersecting temperature is nearly 848K. The two aforementioned studies provide only qualitative comparisons with the Winning et al conjecture because there was no attempt to differentiate diffusion along the dislocation pipe direction from diffusion perpendicular to the pipes. Clearly, it is the latter quantity that is of interest in the climb of a pinning dislocation.

In another experimental study by Herbeuval and Biscondi [161-163] grain boundary diffusion was examined in samples of electrolytically deposited Zn in 99.998% pure Al bi-crystal. In Fig. 4.12, the variation of GB diffusion activation energy is shown as a function of misorientation for a symmetrical  $\langle 001 \rangle$  tilt boundary. In the Herbeuval et al. work diffusion in the two orthogonal directions was reported separately and the magnitude of  $Q$ , for a symmetrical  $\langle 001 \rangle$  tilt boundary, in the direction perpendicular to the intrinsic dislocation lines was around 122 KJ/mol for LAGBs and 67 KJ/mol for the HAGB. The ratio of activation energies, equal to roughly 1.8, is in quantitative agreement with the Winning et al study who reported a ratio of approximately 1.6. Therefore these experimental studies, together with the MD results, suggest that the change in diffusion

behaviour is due mainly to the inherent dislocation spacing difference between low and high angle boundaries.

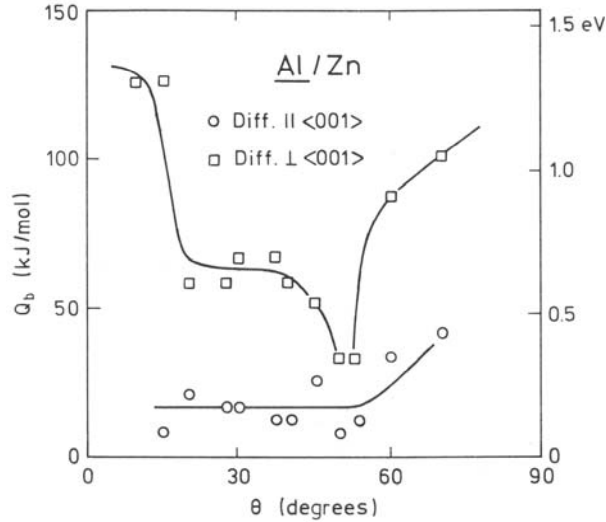


Fig. 4.12: Activation energy of grain boundary diffusion, in the direction parallel and perpendicular to the tilt axis, as a function of misorientation [161].

#### 4.6 Summary of the chapter

As reported in the first chapter, the discrepancies between computationally and experimentally determined grain boundary mobility can be due to the presence of network dislocations in the real materials in experiments. The interaction of those dislocations with migrating boundary can hinder the boundary motion and provide lower mobility of grain boundary. Therefore the interaction behaviour of external dislocations with the grain boundary is of interest and is focused in this chapter due to the lack of available literature capturing this phenomenon. In this chapter we studied the interaction of extrinsic dislocations the migrating low angle and high angle [112] tilt boundaries in pure Al using molecular dynamics simulations and artificial driving force technique. Simulations were performed at a temperature of 300K. At low driving forces, the presence of external dislocations was found to completely pin the grain boundary motion in for both the  $7.785^\circ$  and  $23.07^\circ$  misorientations. Prior to pinning, the network dislocation was observed to rapidly glide parallel to the boundary plane over a distance corresponding to the distance between the intrinsic boundary dislocations. A threshold driving pressure for depinning was obtained for the LAGB and HAGB and it was found that the threshold driving force decreased with increasing misorientation. Both the induced glide and the dependence of threshold stress with orientation are in agreement with previous continuum descriptions of dislocation-boundary interaction.

The results of the MD simulations shed light on the Wininng et al model of grain boundary mobility, which proposes that the activation energy for climb of pinning dislocations corresponds to bulk vacancy diffusion for misorientations less than roughly  $13^\circ$  and transitions to grain boundary diffusion at higher angles. Since the MD results do not reveal significant qualitative differences of the pinned boundary structure for the low and high angle boundaries, we suggest that the transition in activation energy must also exist for conventional solute diffusion. Many previous experimental results are presented to support this view.

## CHAPTER 5

### Conclusion

The goal of this research work was to investigate the low angle grain boundary (LAGB) motion in pure Al and Al-Mg alloys along with some associated features. There were mainly three fold purposes of this study, which are (1) determination of LAGB mobility in pure Al, (2) study of solute pinning effect on the migrating boundary, especially LAGB, in Al-Mg alloys and (3) investigation of extrinsic dislocation interaction with moving low and high angle boundary in pure Al. Throughout the entire thesis, addressing the objectives, we described different applied methodologies and procedures, discussed the simulation observations, analyzed the obtained results and compared them with the previous studies. In this chapter, we will summarize the key conclusions drawn from this project work.

The objective of this thesis was to study the effects of several defects such as solutes and dislocation networks, which are inevitable in the real materials, on the mobility of LAGB. All the previous experimental studies reported that the presence of those defects retard the boundary that provide lower mobility in the experimental observations compared to that of computational studies. But still, there is very few MD simulation studies to capture the solute and dislocation interactions with the migrating grain boundary. This thesis is focused on to provide complete understanding of LAGB determination to develop analytical models of recovery kinetics and comprehensive explanations of solute and dislocation retarding effect boundary motion. In this research work, we provided key insights into the microstructure–property relationship based on the LAGB mobility and its affecting parameters. The major findings of this thesis are highlighted below.

#### Determination of low angle grain boundary mobility

(1) Low angle grain boundary (LAGB) mobility of [112] symmetric grain boundaries in pure Al, determined from the artificial driving force (ADF) and the random walk (RW) techniques in molecular dynamics (MD) simulations, has shown that two methods produce nearly the same mobility, within error bars, at 300K for the grain boundary with  $7.785^\circ$  misorientation and the  $23.07^\circ$  boundary at a temperature of 700K.

(2) A detailed investigation demonstrates that considerable attention must be paid in applying the ADF technique to the case of low angle boundaries. This method is not applicable to compute mobility at temperatures  $\geq 400\text{K}$  for  $7.785^\circ$  boundary due to the failure of order parameter (OP) calculation. We also observed substantial discrepancy between the RW and ADF results for the  $11.655^\circ$  boundary at  $700\text{K}$  temperature.

(3) The activation energy of the LAGB mobility is found to be roughly ten times lower than the experimental results. Most of the previous MD studies exhibited similar discrepancy between experiment and simulation. The discrepancy is, usually reported, due to the presence of impurities and/or network dislocations in real materials.

#### Study of solute pinning on the migrating grain boundary, especially LAGB

(1) A strong solute pinning effect on the migrating  $[112]$  tilt grain boundary is observed in a model Al-Mg binary system at  $300\text{K}$  in molecular dynamics (MD) simulations with the application of artificial driving force (ADF) method.

(2) A high threshold pressure is applied in the solute segregated case to overcome the strong pinning barrier to initiate the boundary migration at all misorientation and concentration examined at  $300\text{K}$ . MD simulation could not capture the low driving force region of Cahn's solute drag analysis as there is no solid state diffusion

(3) The distributed solute technique was observed to provide comparatively less pinning effect on  $7.785^\circ$  boundary (LAGB) migration than that of segregated solutes. The measured solute restraining force shows a linear variation with concentration, which agrees with a relevant study by Hersent et al.

(4) The solute pinning constant,  $\delta=32.6\pm 9.2$  MPa for LAGB in Al-Mg binary system at  $300\text{K}$ , provides pinning pressure that matches well with the MD derived value.

#### Investigation of extrinsic dislocation interaction with migrating LAGB and HAGB

(1) MD simulation results show complete pinning of the migration of grain boundary with  $7.785^\circ$  and  $23.07^\circ$  misorientations due to the interactions with external dislocations under the application of low driving forces.

(2) The extrinsic dislocation was observed to glide rapidly, before pinning, over a distance corresponding to the distance between the intrinsic boundary dislocations. The threshold driving pressure for depinning the boundary was observed to decrease with increasing misorientation.

(3) The MD results do not provide significant qualitative differences in the interaction behaviour of the low and high angle boundaries with extrinsic dislocations. This leads us to suggest that the transition in activation energy, in Winning et. al. model

of grain boundary mobility at roughly  $13^\circ$ , is due to the dependence of grain boundary diffusion on the misorientation. Many previous experimental results are presented in support of this prediction.

## CHAPTER 6

### Future work

This thesis work presented a strong framework to study the low angle grain boundary (LAGB) motion in pure Al and Al-Mg alloys and provides insight into some important aspects, such as solute and dislocation pinning on migrating boundary. As a consequence of the thorough analysis of this research, there are some scopes for further study. A number of suggestions for the possible extensions of this project are summarized in the following:

(1) In this work, low angle grain boundary mobility has been determined in pure Al at different temperatures. It was mentioned in the first chapter that there are a number of recrystallization models that deal with the subgrain motion to describe the kinetics of the nucleation of recrystallization. Therefore, in a future study, those models can be further developed through a quantitative analysis utilizing the MD results of LAGB mobility and their temperature dependence that are obtained in this work. In addition to pure Al, it would be interesting to extend the modified analytical models to the alloy systems, such as Al-Mg, to capture the solute effect using our MD results and interpretations described in the third chapter.

(2) Moreover, future work can be focused on MD simulations to be performed to simulate the actual recrystallization process in pure Al and Al-Mg alloys. This investigation will illustrate the nucleation event by exploring the evolution of the subgrains into viable recrystallization nuclei. The comparison of MD observations with the quantitative model will assist to provide more insights.

(3) To describe the properties of the interfaces with low misorientations properly, the energy of the low angle boundary is required to be determined. The temperature and misorientations dependence of the LAGB energy are the potential candidates for the future investigations of this study. These measurements can be compared to the corresponding experimental results.

(4) In this research work, LAGB mobility has been computed for symmetric tilt boundary motion. This study can be extended to some other boundaries, such as asymmetric tilt and/or twist boundaries. Other than [112] tilt axis, it will be useful to consider other tilt axes, for example [110] and [100] for the determination of interface

mobility. Similarly, future work can also be focused on the employment of different types of boundary and tilt axis to investigate the interaction of solute atoms and extrinsic dislocations with the migrating boundary.

(5) In the study of solute pinning on the LAGB migration, the boundary velocities were calculated using a approach where the solute atoms are distributed in a confined region of the shrinking grain away from the subgrain boundary. This approach was limited to  $7.785^\circ$  boundary motion and hence there are scopes to investigate some high angle boundaries in a future work. The study of solute interaction with migrating boundaries at different misorientation ( $\theta$ ) will assist us to examine the variation of solute pinning behaviour as a function of  $\theta$ .

(6) In this investigation, the interaction behaviour of solute and extrinsic dislocation with the migrating boundaries are studied at the temperature 300K. It is of practical interest to examine both pinning effects at some higher temperatures, which will be helpful to describe the kinetics of recrystallization and grain growth properly. The dependence of the pinning pressure on the temperature can also be explored. As we reported, the artificial driving force (ADF) method is not effective to drive the low angle boundaries, some other techniques, such as capillary force and/or elastic stress driven boundary motion as described in the second chapter, can be applied.

(7) The present study involves the determination of LAGB mobility in pure and binary alloy system. Therefore, the ternary system is still open for further investigation of this research work that will provide the effect of co-segregated solutes on the low angle boundary motion. Moreover, this project can also be extended to study the consequence of solute–extrinsic dislocation interaction on the LAGB movement through the addition of solute atoms in the system that contains network dislocations. These extensions can be carried out at different temperatures and misorientations to demonstrate their dependence on the solute–solute and solute–dislocation interactions.

(8) Besides solutes and externally induced dislocations, some other impurities can be present in all real systems, such as vacancies. As vacancy is considered as one of the elements that controls the microstructure and in turn governs the mechanical integrity of any material, the presence of these impurities might have an effect on the migration of low angle grain boundary. In a plan of future work, some vacancies can be incorporated into the pure and alloy system and the boundary movement will be investigated in the presence of them. To describe a complete kinetics of the LAGB motion, the effect of all kinds of impurities (solutes, network dislocations and vacancies) is required to be encapsulated in the present and future study of this project.

## References

1. <http://www.autoaluminum.org/main/publications-for-download/publications-for-download>.
2. <http://www.autoaluminum.org/main/aluminum-processes-and-materials/aluminum-processes-and-materials>.
3. A.P. Sutton and R.W. Baluffi, Interfaces in crystalline materials, Oxford: Oxford Science Publications; 1995.
4. G. Gottstein and L.S. Shvindlerman, Grain boundary migration in metals: thermodynamics, kinetics and applications, Boca Raton (FL): CRC Press (1999).
5. A.P. Sutton and R.W. Balluffi, Interface in crystalline materials, Oxford, Clarendon Press (1995).
6. V. Randle, *Acta Mater.*, 46, 1459 (1997).
7. G. Gottstein, D.A. Molodov and L.S. Shvindlerman, *Interface Sci.*, 6, 7 (1998).
8. [http://www.tf.uni-kiel.de/matwis/amat/def\\_en/kap\\_7/backbone/r7\\_2\\_1.html](http://www.tf.uni-kiel.de/matwis/amat/def_en/kap_7/backbone/r7_2_1.html).
9. D.L. Olmsted, E.A. Holm and S.M. Foiles, *Acta Mater.*, 57, 3704 (2009).
10. A. Karma, Z.T. Trautt and Y. Mishin, *PRL*, 109, 095501 (2012).
11. J.W. Cahn and J.E. Taylor, *Acta Mater.*, 52, 4887 (2004).
12. M. Winning, A.D. Rollett, G. Gottstein, D.J. Srolovitz, A. Lim and L.S. Shvindlerman, *Philosophical Magazine*, 90, 3107 (2010).
13. C.M. Sellars In: N. Hansen, D. Juul-Jensen, T. Leffers, B. Ralph, editors. Annealing process: recovery, recrystallization and grain growth, Proceedings of the seventh Riso international symposium. Roskilde, Denmark: Riso National Laboratory, 167 (1986).
14. C.M. Sellars In: L. Arnberg, O. Lohne, E. Nes, N. Ryum, editors. International conference on aluminum alloys, 3, Trondheim, Norway, 89 (1992).
15. M.J. Avrami, *Chem. Phys.*, 7, 1103 (1939).
16. M.J. Avrami, *Chem. Phys.*, 8, 212 (1940).
17. M.J. Avrami, *Chem. Phys.*, 9, 117 (1941).
18. F.J. Humphreys and M. Hatherly, Recrystallization and related annealing phenomena. Oxford, UK: Pergamon Press (1996).
19. H.E. Vatne, T. Furu, R. Orsund and E. Nes., *Acta Mater.*, 44, 4463 (1996).
20. F.J. Humphreys, *Acta Mater.*, 45, 4231 (1997).
21. F.J. Humphreys, *Acta Mater.*, 45, 5031 (1997).
22. P.J. Hurley and F.J. Humphreys, *Acta Mater.*, 51, 3779 (2003).
23. H.S. Zurob, Y.J.M. Bréchet and J. Dunlop, *Acta Mater.*, 54, 3983 (2006).
24. J.E. Bailey and P.B. Hirsch, *Proc. R. Soc.*, A267, 11 (1962).
25. R. Sandström, *Acta Metall.*, 25, 905 (1977).
26. S.K. Varma, *Mater. Sci. Eng.*, 82, L19 (1986).
27. Y. Huang and F.J. Humphreys, *Acta Mater.*, 48, 2017 (2000).
28. D.A. Modolov, U. Czubyko, G. Gottstein and L.S. Shvindlerman, *Acta Mater.*, 46, 553 (1998).
29. Y. Huang and F.J. Humphreys, *Acta Mater.*, 47, 2259 (1999).

30. F. Barou, A. Guillotin, Cl. Maurice, J-M. Feppon and J.H. Driver, *Materials Science Forum*, 558-559, 55 (2007).
31. D.A. Modolov, U. Czubayko, G. Gottetein and L.S. Shvindlerman, *Scripta Metall. Mater.*, 32, 529 (1995).
32. K. Lücke and K. Detert, *Acta Metall.*, 5, 628 (1957).
33. J.W. Rutter and K.T. Aust, *Acta Metall.* 6, 375 (1958).
34. K.T. Aust and J.W. Rutter, *Trans. Met. Soc. A.I.M.E.*, 215, 820 (1959).
35. J.W. Rutter and K.T. Aust *Trans. Met. Soc. A.I.M.E.*, 218, 682 (1960).
36. K. Lücke and H. Stüwe, *Recovery and Recrystallization of Metals*, Interscience, NY, p.131 (1963).
37. K. Lücke and H. Stüwe, *Acta Metall.*, 19, 1087 (1971).
38. J.W. Cahn, *Acta Metall.*, 10, 789 (1962).
39. M. Hillert and B. Sundman, *Acta Metall.*, 24, 731 (1976).
40. I. Weiss and J.J. Jonas, *Metall. Trans. A*, 10A, 831 (1979).
41. M.G. Akben, Bacroix and J.J. Joans, *Acta Metall.*, 31, 161 (1983).
42. S.F. Medina and J.E. Mancilla, *ISIJ Int.*, 36, 1063 (1996).
43. H.S. Zurob, Y.J.M Bréchet and G.R. Purdy, *Acta Mater.*, 49, 4183 (2001).
44. C.R. Hutchinson, H.S. Zurob, C.W. Sinclair and Y.J.M. Bréchet, *Scripta Mater.*, 59, 635 (2008).
45. Y.J.M. Bréchet and G.R. Purdy, *Scripta Metall. Mater.*, 24, 1831 (1990).
46. Y.J.M. Bréchet and G.R. Purdy, *Scripta Metall. Mater.*, 27, 1753 (1992).
47. G.R. Purdy and Y.J.M. Bréchet, *Acta Metall. Mater.*, 43, 3763 (1995).
48. I. Andersen and Ø. Grong, *Acta Metall. Mater.*, 43, 2673 (1995).
49. M. Enomoto, *Acta Mater.*, 47, 3533 (1999).
50. M. Hillert, J. Odqvist and J. Ågren, *Scripta Metall.*, 45, 221 (2001).
51. L.M. Fu, H.R. Wang and A.D. Shan, *Mater. Sci. Tech.*, 27, 996 (2011).
52. M. Hillert and M. Schalin, *Acta Mater.*, 48, 461 (2000).
53. J. Svoboda, E. Gamsjäger, F.D. Fisher and P. Fratzl, *Acta Mater*, 52, 959 (2004).
54. J. Svoboda, J. Vala, E. Gamsjäger and F.D. Fisher, *Acta Mater*, 54, 5953 (2006).
55. R. Okamoto and J. Ågren, *Int. Mater. Res.*, 10, 1232 (2010).
56. J. Svoboda, E. Gamsjäger, F.D. Fisher, Y. Liu and E. Kozeschnik, *Acta Mater*, 59, 4775 (2011).
57. Y.J.M. Bréchet and G.R. Purdy, *Acta Mater.*, 51, 18 (2003).
58. C.W. Sinclair, C.R. Hutchinson and Y.J.M. Bréchet, *Metall. Mater. Trans. A*, 38A, 821 (2007).
59. L. Lissel, G. Engberg and U. Borggren: *Proc. of 3rd Int. Conf. On TMP*, Associazione Italiana di Metallurgia/AIM, Padua, Italy, (2008).
60. J. Svoboda, F.D. Fisher and M. Leindl, *Acta Mater*, 59, 6556 (2011).
61. M.I. Mendeleev and D.J. Srolovitz, *Acta Mater*, 49, 589 (2001).
62. M.I. Mendeleev and D.J. Srolovitz and W. E, *Phil. Mag.*, 81, 2243 (2001).
63. M.I. Mendeleev and D.J. Srolovitz, *Int. Sci.*, 10, 191 (2002).
64. M.I. Mendeleev and D.J. Srolovitz, *Int. Sci.*, 10, 91 (2002).
65. R.C. Sun and C.L. Bauer, *Acta Metall.*, 18, 635 (1970).
66. R. Viswanathan and C.L. Bauer, *Acta Metall.*, 21, 1099 (1973).

67. M.S. Masteller and C.L. Bauer, *Acta Metall.*, 27, 483 (1979).
68. M. Furtkamp, G. Gottstein, D.A. Molodov, V.N. Semenov and L.S. Shvindlerman, *Acta Metall.*, 46, 4103 (1998).
69. D.A. Molodov, G. Gottstein, F. Heringhaus and L.S. Shvindlerman, *Acta Mater.*, 46, 5627 (1998).
70. C. Gunster, D. A. Molodov and G. Gottstein, *Mater. Sci. Forum*, 702-703, 635 (2012).
71. C.H. Li, E.H. Edwards and J. Washburn, *Acta Metall.*, 1, 223 (1953).
72. D.W. Bainbridge, C.H. Li and E.H. Edwards, *Acta Metall.*, 2, 322 (1954).
73. C.C. Yang, A.D. Rollett and W.W. Mullins, *Scripta Mater.*, 44, 2735 (2001).
74. B. Schonfelder, D. Wolf, S.R. Phillpot and M. Furtkamp, *Interf. Sci.*, 5, 245 (1997).
75. H. Zhang, M.I. Mendeleev and D.J. Srolovitz, *Acta mater.*, 52, 2569 (2004).
76. B. Schonfelder, G. Gottstein and L.S. Shvindlerman, *Acta Mater.*, 53, 1597 (2005).
77. H. Zhng, M. Upmanyu and D.J. Srolovitz, *Acta Mater.*, 53, 79 (2005).
78. M. Upmanyu, D.J. Srolovitz, L.S. Shvindlerman and G. Gottstein, *Acta Mater.*, 47, 3901 (1999).
79. K.G.F. Janssens, D.L. Olmsted, E.A. Holm, S.M. Foiles, S.J. Plimpton and P.M. Derlet, *Nature Matls.*, 5, 124 (2006).
80. D.L. Olmsted, S.M. Foiles and E.A. Holm, *Acta Mater.*, 57, 3694 (2009).
81. D.L. Olmsted, E.A. Holm and S.M. Foiles, *Acta Mater.*, 57, 3704 (2009).
82. Z.T. Trautt, M. Upmanyu and A. Karma, *Science*, 314, 5799 (2006).
83. J.J. Hoyt, Z.T. Trautt and M. Upmanyu, *Mathmatics and Computers in Simulation*, 80, 1382 (2010).
84. S.M. Foiles and J.J. Hoyt, *Acta Mater.*, 54, 3351 (2006).
85. J. Washburn and E.R. Parkar, *J. of Metals*, 4, 1076 (1952).
86. M. Winning, G. Gottstein and L.S. Shvindlerman, *Acta Mater.*, 50, 353 (2002).
87. C. Herring, in *The Physics of Powder Metallurgy*, P. 143, McGraw-Hill Book Company, New York (1951).
88. M. Winning, G. Gottstein and L.S. Shvindlerman, *Acta Mater.*, 49, 211 (2001).
89. M. Peach and J.S. Koehler, *Phys. Rev.*, 80, 436 (1950).
90. Y. Huang and F.J. Humphreys, *Acta Mater.*, 48, 2017 (2000).
91. L.E. Murr, *Interfacial Phenomena in Metals and Alloys*, Addison-Wesley, Reading, MA (1975).
92. D.A. Molodov, T. Gorkaya and G. Gottstein, *Mater. Sci. Forum*, 558-559, 927 (2007).
93. M.C. Demirel, A.P. Kuprat, D.C. George and A.D. Rollett, *Phys. Rev. Lett.*, 90, 016106 (2003).
94. D.A. Molodov, V.A. Ivanov and G. Gottstein, *Acta Mater.*, 55, 1843 (2007).
95. T. Gorkaya, D.A. Molodov and G. Gottstein, in *Proceedings of the International Conference on Aluminum and its Alloys*, J. Hirsch, ed., DGM, Achen, p. 1071 (2008).
96. M. Ferry and F.J. Humphreys, *Acta Metall. Mater.*, 44, 1293 (1996).
97. F.J. Humphreys, *Scripta Metall.*, 27, 1557 (1992).
98. C. Maurice and F.J. Humphreys, in *Proc. 3<sup>rd</sup> Int. Conf. on Grain Growth*, Pittsburgh, ed. H. Weiland, B. Adams and A. Rollet. TMS, Warrendale, PA, 81 (1998).
99. F.J. Humphreys and M. Hatherly, *Recrystallization and related annealing phenomena*. Oxford, UK: Pergamon Press (1996).

100. T. Furu, R. Orsund and E. Nes, *Acta Metall. Mater.*, 43, 2209 (1995).
101. T. Furu and E. Nes, in *Recrystallization*, 92, San Sebastian, Spain, ed. M. Fuentes and G. Sevillano, Trans. Tech. Publications, Brookfield VT, USA, p. 311 (1992).
102. A.O. Humphreys and F.J. Humphreys, in *Proc. 4<sup>th</sup> Int. Conf. on Aluminium*, Atlanta, Vol. 1, Georgia Inst. Tech., Atlanta, GA, p. 211 (1994).
103. R. Sandström, E. Lehtinen, B. Hedman, I. Groza and J. Karlsson, *J. Mater. Sci.*, 13, 227 (1978).
104. M. Hillert, *Acta Metall.*, 13, 22 (1965).
105. B. Schonfelder, D. Wolf, S.R. Phillpot and M. Frutkamp, *Interface Sci.*, 5, 25, (1997).
106. D.L. Olmsted, S. M. Foiles and E. A. Holm, *Scripta Mater.*, 57, 1161 (2007).
107. J.W. Cahn, Y. Mishin and A. Suzuki, *Acta Mater.*, 54, 4953 (2006).
108. J.W. Cahn, Y. Mishin and A. Suzuki, *Phil. Mag. A*, 86 (25-26), 3965 (2006).
109. E.A. Holm and S.M. Foiles, *Science*, 328, 1138 (2010).
110. C. Deng and C.A. Schuh, *Phys. Rev. B*, 84, 214102 (2011).
111. M.I. Mendeleev, M. Asta, M.J. Rahman and J.J. Hoyt, *Philosophical Magazine*, 89, 3269 (2009).
112. M.S. Daw and M.I. Baskes, *Phys. Rev. B*, 29, 6443 (1984).
113. M.S. Daw, S.M. Foiles and M.I. Baskes, *Materials Science Reports*, 9, 251 (1993).
114. S.J. Plimpton, *J. Comp. Phys.*, 117, 1 (1995).
115. <http://lammps.sandia.gov/>.
116. Kelchner, Plimpton and Hamilton, *Phys. Rev. B*, 58, 11085 (1998).
117. M.I. Mendeleev, M.J. Rahman, J.J. Hoyt and M. Asta, *Modelling Simul. Mater. Sci. Eng.*, 18, 074002 (2010).
118. J.G. Kirkwood, *J. Chem. Phys.*, A 40, 3817 (1989).
119. David Olmsted, private communication.
120. M.I. Mendeleev, C. Deng, C.A. Schuh and D.J. Srolovitz, *Modelling Simul. Mater. Sci. Eng.*, 21, 045017 (2013).
121. A. Roy and C.L. Bauer, *Acta Metall.*, 23, 957 (1975).
122. A.L. korzhenevskii, R. Bausch, R. Schmitz, *Acta Mater.*, 54, 1595 (2006).
123. M. Hillert, *Acta Mater.*, 47, 4481 (1999).
124. M. Hillert, *Acta Mater.*, 52, 5289 (2004).
125. M. Hillert and B. Sundman, *Acta Metall*, 25, 11 (1977).
126. J. Ågren, *Acta Metall.*, 37, 181 (1989).
127. E.S. Machlin, *Trans. AIME*, 224, 1153 (1962).
128. E. Hersent, K. Marthinsen and E. Nes, *Metall. Mater. Trans. A*, 44A, 3364 (2013).
129. N.F. Fiore and C.L. Bauer, *Prog. Mater. Sci.*, 13, 85 (1967).
130. R. Sandström, B. Lehtinen, E. Hedman, I. Groza and S. Karlsson, *J. Mat. Sci.*, 13, 1229 (1977).
131. C.K. Syn, A. Ahmadiéh and J.W. Morris Jr., *Scripta Metall.*, 9, 1255 (1975).
132. P. Cha, S.G. Kim, D. Yeon and J. Yoon, *Acta Mater.*, 50, 3817 (2002).
133. K. Grönhagen and J. Ågren, *Acta Mater.*, 55, 955 (2007).
134. I. Loginova, J. Odqvist, G. Amberg and J. Ågren, *Acta Mater.*, 51, 1327 (2003).

135. K.R. Elder, M. Katakowski, M. Haataja and M. Grant, *Phys. Rev. Lett.*, 88, 245701 (2002).
136. K.R. Elder and M. Grant, *Phys. Rev. E*, 70, 051605 (2004).
137. M. Greenwood, C.W. Sinclair and M. Milizer, *Acta Mater.*, 60, 5752 (2012).
138. A.T. Wicaksono, C.W. Sinclair and M. Militzer, *Modelling Simul. Mater. Sci. Eng.*, 21, 085010 (2013).
139. Y. Yang, H. Humadi, D. Buta, B.B. Laird, D.Y. Sun, J.J. Hoyt and M. Asta, *Phys. Rev. Lett.*, 107, 025505 (2011).
140. I. Toda, P.D. Bristowe and C. Capdevila, *Acta Mater.*, 60, 1116 (2012).
141. 'A comprehensive molecular dynamics study of low angle grain boundary mobility in pure aluminum system', M.J. Rahman, H.S. Zurob and J.J. Hoyt, In press, *Acta Mater.* (2014).
142. D. Frenkel, *Advanced Monte Carlo Techniques NATO ASI Series C*, vol 397, ed M.P. Allen and D.J. Tildesley (Dordrecht: Kluwer), p 93 (1993).
143. D. Frenkel and B. Smit, *Understanding Molecular Simulation* (New York: Academic) (1996).
144. D.L. Olmsted, L.G. Hector Jr., W.A. Curtin and R.J. Clifton, *Modelling Simul. Mater. Sci. Eng.*, 13, 371, (2005).
145. D.L. Olmsted, L.G. Hector Jr. and W.A. Curtin, *J. Mechanics. Phys. of solids*, 54, 1763 (2006).
146. J.J. Hoyt, *Model. Simul. Mater. Sci. Eng.*, in Press (2014).
147. M.I. Mendeleev and D.J. Srolovitz, *Acta Mater.*, 49, 2843 (2001).
148. M.I. Mendeleev and D.J. Srolovitz, *Model Simul. Mater. Sci.*, 10, R79 (2002).
149. J. Chang, W. Cai, V.V. Bulatov and S. Yip, *Materials Science and Engineering A*, 309, 160 (2001).
150. J. Chang, W. Cai, V.V. Bulatov and S. Yip *Computational Materials Science*, 23, 111 (2002).
151. J. Chang, V.V. Bulatov and S. Yip, *J. Computer-Aided Materials Design*, 6, 165 (1999).
152. W. Cai, V.V. Bulatov and S. Yip, *J. Computer-Aided Materials Design*, 6, 175 (1999).
153. W. Cai, V.V. Bulatov, S. Yip and A.S. Argon, *Materials Science and Engineering A*, 309, 270 (2001).
154. Z. Shen, R.H. Wagoner and W.A.T. Clark, *Acta Metall.*, 36, 3231 (1988).
155. M. Koning, R.J. Kurtz, V.V. Bulatov, C.H. Henager, R.G. Hoagland, W. Cai and M. Nomura, *J. Nuclear Materials*, 323, 281 (2003).
156. B. Liu, D. Raabe, P. Eisenlohr, F. Roters, A. Arsenlis and G. Hommes, *Acta Mat.*, 59, 7125 (2011).
157. A.T. Lim, D.J. Srolovitz and M. Haataja, *Acta Mater.*, 57, 5013 (2009).
158. D.L. Beke, I. Gödney and F.J. Kedvis, *Trans. Jap. Inst. Metals (Suppl.)*, 27, 649, (1986).
159. D.L. Beke and F.J. Kedvis, *Crystal Res. Technol.*, 20, 73, (1985).
160. T. Fujita, Z. Horita and T.G. Langdon, *Materials Science and Engineering A*, 371, 241(2004).

161. I. Herbeuval, M. Biscondi and C. Goux, *Mem Sci. Rev. Metall.*, 70, 39 (1973).
162. I. Herbeuval and M. Biscondi, *C.R. Acad. Sci. C*, 273, 1416 (1971).
163. I. Herbeuval and M. Biscondi, *Canad. Metall. Quart.*, 13, 171 (1974).